

**AN INVESTIGATION OF DYNAMIC FAILURE EVENTS IN  
STEELS USING FULL-FIELD HIGH-SPEED INFRARED  
THERMOGRAPHY AND HIGH-SPEED PHOTOGRAPHY**

Thesis by

Pradeep R. Guduru

In Partial Fulfillment of the Requirements

For the Degree of

Doctor of Philosophy



Graduate Aeronautical Laboratories

California Institute of Technology

Pasadena, California

2001

(Defended September 15, 2000)

© 2001

Pradeep R. Guduru

All Rights Reserved

*To my parents,*

Chandrakala Guduru  
and  
Malla Reddy Guduru

*And my sisters*

Santhi and Thriveni

## Acknowledgements

I would like to express my sincere gratitude to my thesis advisor, Professor Ares J. Rosakis for his invaluable guidance, support and encouragement during my years at Caltech. I have greatly benefited from his incessant insistence on the fundamentals and his infectious zeal for teaching. I thoroughly enjoyed the complete freedom I was provided to explore and experiment with all ideas and I deeply appreciate his ceaseless confidence in me throughout the ups and downs of my graduate life.

I can not thank enough Professor G. Ravichandran, who unceasingly monitored my learning process at Caltech. His wise and generous advice kept me focussed all along. I truly value my innumerable discourses with him on topics ranging from history to philosophy during our runs to Henninger flats on the Mt. Wilson trail.

I sincerely thank Professor A.T. Zehnder for his pivotal role in developing the infrared camera. I also thank Dr. Arie Venkert for introducing me to the world of microscopic analysis. I am grateful to Professor J.K. Knowles, Professor W.L. Johnson and Professor M. Gharib who served on my thesis committee and provided many valuable suggestions.

I would like to thank Dr. David M. Owen for his many practical ideas in conducting the experiments and his help with scanning electron microscopy. He had an elegant solution to every problem I had and he never seemed to run out of ideas.

I am indebted to Prof. John Lambros for introducing me to dynamic fracture experimental facilities and to Prof. Raman Singh for teaching me the art of good experimentation. I wish to thank Prof. Hongbing Lu for patiently training me in many lab techniques during my early days as a graduate student. Special thanks to Petros Arakelian

who was always very helpful and resourceful. I would also like to thank Joe Haggerty, Ali Kiani, Larry Frazier and Bradley St. John for their help in the machine shop.

The real pleasure of living and working at Caltech has been my interaction with my fellow students. They are too many to list in this short space, but I can not miss expressing my gratitude to my good friends Demir Coker, Omprakash Samudrala, Sangwook Lee, Sandeep Sane, Hansuk Lee, Sairam Sundaram, Ying Huang, Bibhuti Patel and Javier Gonzalez. And what a joy it has been to hang out with these guys!

Last, but not the least, I would like to thank Denise Thobe, who with her bubbly personality, has always been a source of inspiration. I am especially grateful to her for her patience and all her help in making my stay at GALCIT a very pleasant experience.

Financial support for this work was provided by the Office of Naval Research (Dr. Y.D.S. Rajapakse, Scientific Officer) and the Engineering Research Program of the Office of Basic Energy Sciences at the Department of Energy (Dr. Robert Price, Project Officer). Additional support for the construction of the high-speed infrared camera was provided by the National Science Foundation through the Center for Quantitative Visualization at GALCIT (Professor M. Gharib, Director) and is gratefully acknowledged.

## Abstract

**An** infrared (IR) imaging system has been developed recently at Caltech for measuring the temperature increase during the dynamic deformation of materials. The system consists of an 8x8 HgCdTe focal plane array, with 64 parallel preamplifiers. Outputs from the 64 detector/preamplifiers are digitized using a row-parallel scheme. In this approach, all 64 signals are simultaneously acquired and held using a bank of track and hold amplifiers. An array of eight 8:1 multiplexers then routes the signals to eight 10MHz digitizers, acquiring data from each row of detectors in parallel. The maximum rate is one million frames per second.

Crack tip temperature rise during dynamic deformation is known to alter the fracture mechanisms and consequently the fracture toughness of a material. However, no direct experimental measurements have ever been made to determine the same because of limited diagnostic tools. Further, the temperature rise in the vicinity of the crack tip could potentially be used as a direct measure of loading and could serve as a diagnostic tool in order to extract appropriate fracture parameters. By transcending the existing experimental limitations, this investigation presents detailed, real time evolution of the transient crack tip temperature fields in two different steels (C300 and HY100 steels), using the 2-D high speed IR camera. The crack tip temperature rise at initiation in C300 steel was found to be about 55K. In case of HY100, the crack tip temperature rise was above 90K and was seen to be a strong function of loading rate. HRR elastic-plastic

singular field has been used to extract J integral evolution from the measured temperature field. Critical value of J integral at initiation was seen to increase with loading rate.

An experimental investigation has been conducted to study the initiation and propagation characteristics of dynamic shear bands in C300 maraging steel. Pre-fatigued single edge notched specimens were impacted on the edge under the notch to produce shear dominated mixed mode stress fields. The optical technique of coherent gradient sensing (CGS) was employed to study the evolution of the mixed mode stress intensity factors. Simultaneously, the newly developed 2-D high speed infrared (IR) camera was employed to obtain the temperature field evolution during the initiation and propagation of the shear bands. A criterion for shear band initiation is proposed in terms of a critical mode II stress intensity factor. The IR images, for the first time, revealed the transition of crack tip plastic zone into a shear band and also captured the structure of the tip of a propagating shear band. These thermographs support the notion of a diffuse shear band tip and reveal "hot spots" distributed along the length of a well developed shear band.

## Table of Contents

Acknowledgements.....	iv
Abstract .....	vi
Table of contents .....	viii
Introductory remark.....	xii
Chapter 1 Million Frames per Second Infrared Imaging System .....	1
Abstract .....	1
1.1 Introduction.....	2
1.2 System design.....	4
1.2.1 Optics .....	4
1.2.2 Infrared detector array.....	6
1.2.3 Multiplexers and data acquisition.....	7
1.3 System calibration and test.....	9
1.3.1 Spatial resolution.....	9
1.3.2 Temporal resolution.....	10
1.3.3 Calibration.....	10
1.4 Results.....	12
1.5 Summary.....	13
References.....	14
List of figures.....	15

## Chapter 2 Dynamic Full Field Measurements of Crack Tip Temperatures . 26

Abstract.....	26
2.1 Introduction.....	27
2.2 Experiments.....	30
2.2.1 Material .....	30
2.2.2 Experimental technique.....	31
2.2.2.1 Infrared imaging .....	31
2.2.2.2 IR System calibration .....	35
2.2.3 Specimen geometry and loading arrangement.....	36
2.2.3.1 C300 maraging steel .....	36
2.2.3.2 HY100 steel .....	37
2.3 Results.....	38
2.3.1 C300 steel.....	38
2.3.1.1 Temperature images.....	38
2.3.1.2 Comparison with Rice and Levy model .....	39
2.3.2 HY100 steel.....	43
2.3.2.1 Temperature images.....	43
2.3.2.2 J integral estimation.....	45
2.4 Concluding remarks.....	49
References.....	52
List of tables .....	58
List of figures.....	59

## Chapter 3 Dynamic Shear Bands: An Investigation Using High Speed

Optical and Infrared Diagnostics .....	84
Abstract .....	84
3.1 Introduction.....	85
3.2 Experimental techniques.....	95
3.2.1 Material and specimen geometry .....	95
3.2.2 Coherent gradient sensing (CGS).....	96
3.2.3 Infrared thermography.....	99
3.2.3.1 Two-dimensional infrared imaging system .....	99
3.2.3.2 IR System calibration .....	102
3.2.3.3 Specimen support and triggering.....	104
3.3 Experimental results .....	105
3.3.1 Failure modes .....	105
3.3.2 Stress intensity factor history when $v < 26\text{m/s}$ .....	106
3.3.3 Incipient shear banding when $v < 26\text{m/s}$ .....	111
3.3.4 Stress intensity factors when $v > 26\text{m/s}$ .....	112
3.3.5 Shear band propagation speed.....	113
3.3.6 Crack initiation under mixed mode loading.....	114
3.3.7 Micrographs of shear bands .....	114
3.3.8 Temperature measurement .....	115
3.3.8.1 Temperature field at the crack tip.....	116
3.3.8.2 Structure of the tip of a propagating shear band.....	117

3.3.8.3 Temperature structure along a propagating shear band.....	118
3.4 Concluding remarks.....	121
References.....	123
List of tables .....	132
List of figures.....	133

## **Introductory Remark**

This doctoral dissertation consists of three chapters, each with its own abstract, introduction and conclusions. The overall theme of this work is to make quantitative observations of some dynamic failure events in solids by imaging the transient temperature fields associated with them using the two-dimensional high speed infrared (IR) camera recently developed at Caltech. The first chapter describes the design and the working of the IR camera and the results of some preliminary experiments to test its capability.

The second chapter details the full field measurement of crack tip temperature fields when subjected to dynamic mode I loading, in two different steels. Crack tip temperature rise during dynamic deformation is known to alter the fracture mechanisms and consequently the fracture toughness of a material. However, no direct experimental measurements have ever been made to determine the same because of limited diagnostic tools. In addition, although it has been common knowledge that the loading of the crack tip is done via the development of a plastic zone, there has never been any real time visualization of its development and the distribution of plastic dissipation in it. Further, the temperature rise in the vicinity of the crack tip could potentially be used as a direct measure of loading and could serve as a diagnostic tool in order to extract appropriate fracture parameters. Detailed, real time evolution of the transient crack tip temperature fields in two different steels, using a 2-D high speed infrared camera, is presented. Experimental results are compared with the predictions of some analytical models. In

case of ductile steels, a method to extract the critical J integral from the temperature measurements is discussed.

The third chapter deals with an investigation to study the failure mode transition and the initiation and propagation characteristics of dynamic shear bands in C300 maraging steel. Pre-fatigued single edge notched specimens are impacted on the edge under the notch to produce shear dominated mixed mode stress field at the crack tip. In order to study the evolution of mixed mode stress intensity factors, the optical technique of coherent gradient sensing (CGS) along with high speed photography is employed. Simultaneously, on the other side of the specimen, the high speed infrared (IR) camera is used to image the temperature evolution during the initiation and propagation of shear bands. The CGS images reveal the evolution of the stress intensity factors prior to failure and the critical conditions for both failure modes, i.e., opening crack and shear band, are identified. The IR images, for the first time, reveal the transition of crack tip plastic zone in to a shear band. The images also capture the structure of the tip of a propagating shear band. These thermographs support the notion of a diffuse shear band tip, with gradual temperature rise associated with it. Thermal images of a well developed shear band show that the temperature along the band is highly non-uniform, with "hot spots" distributed along its length. These hot spots are believed to be the consequence of a flow related instability operating at the length scale of the shear band width. Relevant analytical results are discussed to support this idea.

# Chapter 1

## Million Frames per Second Infrared Imaging System

### Abstract

An infrared imaging system has been developed for measuring the temperature increase during the dynamic deformation of materials. The system consists of an 8x8 HgCdTe focal plane array, each with its own preamplifier. Outputs from the 64 detector/preamplifiers are digitized using a row-parallel scheme. In this approach, all 64 signals are simultaneously acquired and held using a bank of track and hold amplifiers. An array of eight 8:1 multiplexers then routes the signals to eight 10MHz digitizers, acquiring data from each row of detectors in parallel. The maximum rate is one million frames per second. A fully reflective lens system was developed, consisting of two Schwarzschild objectives operating at infinite conjugation ratio. The ratio of the focal lengths of the objectives determines the lens magnification. The system has been used to image the distribution of temperature rise near the tip of a notch in a high strength steel sample (C-300) subjected to impact loading by a drop weight testing machine. The results show temperature rises at the crack tip up to around 70K. Localization of temperature, and hence of deformation into 'U' shaped zones emanating from the notch tip, is clearly seen, as is the onset of crack propagation.

## 1.1 Introduction

Most of the energy that goes into permanently, or inelastically, deforming a material is dissipated thermally. Bending a paper clip back and forth until it breaks, and then putting the broken piece to one's lips to feel the temperature increase easily demonstrates this phenomenon. In many industrial processes and scientific problems involving dynamic, inelastic deformation of materials, similar temperature increases occur. The increase in temperature can in some cases be very large in which case the temperature itself becomes an important parameter in the deformation process. Examples include dynamic fracture <sup>1, 3</sup>, metal cutting <sup>4</sup>, formation of adiabatic shear bands <sup>5,6</sup> and ballistic impact <sup>7</sup>. These processes all involve extensive permanent deformation occurring over a time scale that is too fast for the heat to dissipate to the environment before the deformation is complete. Large increases in temperature lead to thermal softening of the material, which promotes localization of deformation and hence even higher temperatures. High temperatures can also strongly affect the life of tooling used in manufacturing processes such as metal cutting. In other situations, such as impact at high, but not ballistic rates, or stable crack growth, there may be temperature increases moderate enough not to have a strong effect on deformation. Nonetheless, such temperature increases provide a useful means of gathering information about energy dissipation in the process <sup>8</sup>.

In all of the examples described above, it is desirable to measure the temperature of the object undergoing dynamic deformation. Ideally, the measurement should be non-contact, real-time, accurate and spatially resolved. In the impact induced dynamic fracture and shear band problems we are interested in, deformation, fracture and the

resulting temperature increases of 10-1000°K occur over time scales of a few tens to hundreds of microseconds, and over size scales of 10-1000 $\mu$ m. Thus to study deformation induced heating and the resulting effects on the deformation process, a means of measuring temperature accurately, with high spatial resolution and at rates of around one million frames per second, is required. Although there have been great advances in infrared (IR) imaging systems in recent years, there are no commercial systems capable of imaging at such high speeds. IR imaging systems typically run at television rates, 30 Hz, although higher speed systems do exist, with rates of up to 34kHz<sup>9</sup>. Temperature at a point or averaged over a region can be measured at very high speeds using single element IR detectors in conjunction with high speed data acquisition<sup>10,11</sup>. Linear arrays of up to 16 IR detectors have been used to measure the temperature field around dynamically growing cracks<sup>1-3</sup>. Methods of measuring temperature during dynamic crack growth are reviewed in reference 3.

Although a great deal can be done with single element and linear arrays of high speed IR detectors, to actually measure the temperature field requires a two-dimensional detector array. To achieve the required framing rates of up to 1MHz requires very fast data acquisition in conjunction with a high-speed IR detector array. The bottleneck in performing such measurements has been data acquisition. However, the availability of fast, relatively inexpensive digitizers has now allowed us to design and build an infrared (IR) imaging system that, for the first time, enables the measurement of thermal fields at rates of up to 1 million frames per second. The complete imaging system, consisting of the focusing optics, IR focal plane array, multiplexing circuits, and data acquisition

boards is described in the block diagram of Figure 1 and shown in the photograph of Figure 2. At the heart of the system is an 8x8 focal plane array of HgCdTe IR detector elements. Each of the 64 elements has its own preamplifier, the outputs of which are fed into a bank of eight 8:1 multiplexers. The multiplexed signals are then digitized using 4 two-channel, Gage 1012 A/D boards, running at speeds up to 10MHz. Radiation emitted from the object as it deforms and heats up is focused onto the IR focal plane array using a reflective lens, built up out of two Schwarzschild objectives, each operating at infinite conjugation ratio. The magnification of each lens is fixed, thus to achieve different magnifications different lenses are used. In this system, there is no integration of the signal between frames as in commercial IR cameras; thermal resolution is sacrificed in favor of speed. The details of each of the components of the system are given in the next section, followed by examples of results obtained with the imager.

## **1.2 System Design**

### **1.2.1 Optics**

There are several requirements to be satisfied in the design of the optics. The setup of the system is greatly simplified if it can be focused using visible light. This leads to a fully reflective lens. The size of each IR detector element is  $100 \times 100 \mu\text{m}$ . It was desired to have fields of view per detector ranging from approximately 180 to  $50 \mu\text{m}$ . It is also important that the light gathering capability is large, i.e., low f-number, and that the blur at the focal plane due to various aberrations be less than  $100 \mu\text{m}$ . Note that due to the relatively large size of the IR elements, achieving diffraction-limited performance in the

optics was not necessary.

To obtain a range of magnifications, two lenses were designed and built, one with a magnification of 1.3X (or 1/1.3X if used in reverse) and the other with 1.8X (or 1/1.8X). Each lens consists of two Schwarzschild objectives<sup>12</sup>, each operating at infinite conjugation ratio. Schwarzschild objectives consist of a large, concave primary mirror with a central aperture and a smaller, convex secondary mirror, located concentrically with the primary. The ratio of the primary mirror to secondary mirror focal lengths depends on the conjugation ratio used. At infinite conjugation ratio the best value is  $f_{\text{primary}}/f_{\text{secondary}}=2.54$ <sup>12</sup>. The 1.3X system is shown in Figure 3. In the arrangement shown, the left side, or the object side, is a lens with  $f=47.5\text{mm}$ . On the right side is a lens with  $f=63.3\text{mm}$ . The ratio of the focal lengths of each side determines the magnification. Modules of this design are easily combined to achieve different magnifications. The lenses are located so that the focal point of the left side coincides with the object, and the focal point of the right side coincides with the image.

For the actual lenses, rather than have custom lenses ground, we used gold-coated plano-convex and plano-concave mirrors from a standard catalog<sup>b)</sup> edged and drilled to our specifications. Thus small deviations from the ideal  $f_{\text{primary}}/f_{\text{secondary}}$  ratio of 2.54 were allowed in the interest of economy. The actual values range from 2.53 to 2.58. We found by ray tracing that these deviations do not deteriorate the resolution greatly. For

---

<sup>b)</sup> Rolyn Optics, Covina, CA

example, in the 1.3X system, both the left and right sides have a mirror ratio of 2.58. The spot size on the focal plane array (when used in the 1.3X magnification) is only 4 $\mu\text{m}$ . The mirrors, housed in a black anodized aluminum cylinder, are mounted ahead of the IR detector dewar as shown in the photograph of Figure 2.

### 1.2.2 Infrared Detector Array

The temperatures of interest in dynamic deformation of materials range from 1-1000°C. At the lower range of temperatures, most of the radiation is near 10 $\mu\text{m}$ . Thus to achieve high sensitivity the IR detectors should have significant response at this wavelength. For this reason and for reasons having to do with availability of IR arrays and willingness of IR array manufacturers to build a custom array, we chose to work with HgCdTe detectors. The IR detector array was custom built for this project by Fermionics<sup>c)</sup>. It consists of a back illuminated 8x8 array of HgCdTe elements. The elements are sensitive to radiation from approximately 2-10 $\mu\text{m}$ , with the peak sensitivity at approximately 8 $\mu\text{m}$ . The time response is very fast, limited only by the bandwidth of the preamplifiers. Each element is 100x100 $\mu\text{m}$  with a center to center spacing of 130 $\mu\text{m}$ . To minimize detector cross talk, a ground plane surrounds each element. The array is indium bump bonded to a fan out board that mounts in a lead-less chip carrier, housed in a side looking liquid nitrogen cooled dewar. The detector elements are in vacuum, in

---

<sup>c)</sup> Sirni Valley, CA

contact with the liquid nitrogen cooled dewar's cold finger, and mounted behind a 6mm thick ZnSe window.

The detector elements operate essentially as photodiodes; i.e., they output a current that is proportional to the incident radiation. This current is converted to voltage using the transimpedance amplifier shown in Figure 4. The elements are held at a 3.9V back bias, and the output is AC coupled to reject signals due to the detector's dark current. The bandwidth of the detector-amplifier system is 500kHz.

### **1.2.3 Multiplexers and Data Acquisition**

The key to acquiring images at the desired one million frames per second rate is fast, low noise data acquisition. One approach would be to have 64 digitizers, one for each pixel of the array. Such an approach is not only clumsy but was well beyond our budget. Thus an alternative approach was taken using row-parallel data acquisition. In this scheme, each row of elements is fed into its own custom built 8:1 multiplexer. The output from each multiplexer is digitized by one of the eight 10MHz digitizers.

The block diagram of the multiplexer circuit is shown in Figure 5. At the front end of each multiplexer are eight HA5351 track and hold amplifiers, configured for unity gain. The first four inputs are fed to one CLC533 4:1 multiplexer and the second four are fed to another CLC533. The outputs of these are fed to a third CLC533. When, for example, images are to be acquired at 1 million frames per second, a 10MHz clock is provided to the timing circuit. The timing diagram is shown in Figure 6. The timing circuit is

essentially a decade counter. It provides a track and hold signal to the HA5351 causing it to track the inputs for 100ns, then hold them for 900ns while the multiplexers switch through the outputs 10 times per frame, i.e., every 100ns. After the 8 input signals are switched through the system, a 0.5V signal is fed to the output for 200ns. During the time the 0.5V signal is sent to the output, the track and hold amplifiers are tracking, then acquiring the signals. This provides sufficient tracking and settling time for the HA5351. The 0.5V signal provides a marker in the output record signifying where a frame begins and ends. With reference to Figure 5, the sequence of outputs from the multiplexer is 1A, 2A, 1B, 2B, 1C, 2C, 1D, 2D, 0.5V, 0.5V.

The output signals from the 8 multiplexers are fed to the inputs of 4 two channel, 10MHz, 12 bit A/D boards (Gage 1012) mounted in an industrial PC. Each board has 512k memory, sufficient to store up to 25,000 frames of data. To ensure synchronization, the A/D boards are clocked externally using the same clock that drives the multiplexers. Data is acquired 40 ns after the rising edge of the clock. Thus (see the timing diagram of Figure 6) data is acquired at approximately 40ns after the multiplexers have switched from one output to the next. The settling time of the CLC533 multiplexers is about 25ns, so the 40ns delay provides sufficient time for the signal to settle before the data are digitized. Experiments are typically run in a single shot mode whereby a number of frames are acquired at high speed, stored on the memory of the A/D boards, and then transferred to the host computer's disk drive once the test is over.

## 1.3 System Calibration and Test

To ensure integrity of the results great care must be taken in calibrating the system, understanding the system limitations, noise levels, accuracy, precision and both spatial and temporal resolution.

### 1.3.1 Spatial Resolution

The spatial resolution is determined by the resolution of the optics, by the element size and cross talk of neighboring IR detector elements. The detector element, or pixel, size is  $100\mu\text{m}$  square. The maximum magnification lens used is 1.8X, thus the best attainable spatial resolution is  $55\mu\text{m}$ . Resolution could be increased using higher magnification lenses, however, since the radiation being imaged is in the range of  $10\mu\text{m}$  wavelength, one can not expect to do much better than about  $20\mu\text{m}$  spatial resolution. To test the actual resolution a vertically oriented  $75\mu\text{m}$  diameter, NiCr wire is placed in the object position and heated with an electrical current. Using the 1.3X lens the  $75\mu\text{m}$  wire gets mapped to  $100\mu\text{m}$  on the focal plane array. If the focus were perfect and if there were no cross talk between the detector elements, once the system is focused to obtain the maximum signal on a single column of elements, there should be no signal on the adjacent elements. In practice there is electrical cross talk between elements and the focusing is not perfect. At the best focus, adjacent elements output a signal that is 15%

of the element the hot wire is focused on. The next nearest neighbors output a signal that is 6%. The cross talk check is repeated with the wire in the horizontal position. Knowing this cross talk we can correct for it in the analysis of the data by setting up and solving 64 linear equations of the form

$$s_i = \frac{1}{1.84} [r_i + 0.15(r_{i+1} + r_{i-1} + r_{i-8} + r_{i+8}) + 0.06(r_{i+2} + r_{i-2} + r_{i-16} + r_{i+16})]$$

where the elements are numbered  $i=1,64$ ,  $s_i$  is the measured signal from element  $i$  and  $r_i$  is the actual signal on element  $i$ . The 111.84 term is there to give  $r_i=s_i$  when there is uniform illumination. These equations are modified for elements at the edges of the array since they don't have neighbors to one side.

### 1.3.2 Temporal Resolution

The temporal resolution is limited by the bandwidth of the detector-amplifier system and the 1MHz maximum digitization rate. To verify the time response of the system, an IR emitting LED is placed in front of the HgCdTe detector array and pulsed. The rise time in response to a step input from the IR LED is approximately  $1\mu\text{s}$ , equivalent to a 500kHz bandwidth.

### 1.3.3 Calibration

Calibration of the system is performed in a very direct manner. A sample of the same

material and surface finish as will be tested is heated in an oven to several hundred °K. The heated sample, instrumented with a thermocouple to record its surface temperature, is placed in the object position. As the sample cools, the voltage output from each of the IR elements is recorded by the data acquisition system along with the sample temperature. This procedure provides a voltage vs. temperature curve for each element.

Since the IR system is AC coupled, the input radiation to the detectors must contain an AC component. This is achieved by placing a chopping wheel in front of the heated calibration specimen. An LED-Photodiode pair is placed across the chopping wheel to synchronize the data acquisition with the chopping. While the chopping wheel is covering the calibration sample, 64 points are recorded. Another 64 points are recorded while the wheel exposes the sample. Each of the sets of 64 points is averaged, then their difference taken to provide the peak-to-peak voltage output corresponding to a given temperature. A typical calibration curve, obtained using the 1.3X magnification lens, is shown in Figure 7. Near room temperature, the sensitivity is approximately 1 mV/°K. We have found that there are significant variations in the outputs of the detector elements, thus each element must have its own calibration. The system noise level, which, as recorded by the A/D boards, is approximately 2 mV, corresponding to a temperature resolution of 2°K. The thermal resolution can be increased by using lower magnification, causing each detector to gather radiation from a larger area. The scatter in the calibration determines the uncertainty in the temperatures. For the 1.3X system calibration plotted in Figure 7, the uncertainty in temperature is approximately  $\pm 5\%$ .

## 1.4 Results

One of the first applications of the system was to characterize the transient temperature fields associated with the process of crack initiation and growth in a high strength steel. A C-300 maraging steel plate (yield strength of about 1900 MPa) with a pre-fabricated crack was impact loaded in a drop weight tower as shown in Figure 8. The IR imaging system was focused on an area of approximately 1.1 x 1.1 mm, as shown in the figure.

Two sequences of thermal images from the same experiment are shown in Figure 9. Note that the last images in Figure 9a is the same as the first image of 9b. They appear different because of the different temperature scales used in plotting them. In Figure 9a, a more or less symmetric, 'U' shaped zone of high temperature develops at the crack tip about 160  $\mu$ s after impact. This zone of high temperature corresponds to the region in which plastic deformation occurs. Thus the thermal images show us that the deformation is somewhat localized along diagonal bands emanating from the crack tip. The temperature field stays symmetric until about 226 ps.

Asymmetry in the temperature distribution can be seen to begin and build up rapidly in Figure 9b. This is an indication that the crack has begun to grow. This experiment provides us, for the first time, the detailed distribution of the temperature field around the crack tip and an indication of the associated distribution of dissipated plastic work at the specimen surface. Taking the crack initiation time to be around 226 ps, the experiment also revealed that the specimen surface at the crack tip heats up by as much as 55°K by the time of crack initiation. This temperature rise under different loading rates could be

used as a measure of the resistance of the material to crack growth. The observed temperature distribution could also serve as a bench mark for comparing any future theoretical/computational studies on crack initiation and propagation in similar materials.

## **1.5 Summary**

By using a fully row-parallel data acquisition scheme, whereby data from each row of an IR focal plane array is acquired simultaneously, a system capable of acquiring 8x8 IR images at a rate of 1 million frames per second has been assembled from a combination of standard and custom built components. This system, consisting of an 8x8 HgCdTe focal plane array, 64 preamplifiers and track and hold amplifiers, eight 8:1 multiplexers, eight 10MHz, 12 bit digitizers, and a fully reflective lens system, is capable of spatial resolution down to approximately 50  $\mu\text{m}$ , and a temperature resolution of approximately 2°K. In its first application, the system has been used to image the distribution of temperature rise near the tip of a notch in a high strength steel sample (C-300) subject to impact loading by a drop weight testing machine. The results show temperature rises at the crack tip up to around 70°K. Localization of temperature, and hence of deformation into 'U' shaped zones emanating from the notch tip is clearly seen, as is the onset of crack propagation. Many other applications of this system to solid and fluid mechanics can be anticipated. A few examples include: temperatures in reactive flows, temperature rise in dynamic shear banding, and temperature rise during ballistic impact.

## References

- <sup>1</sup> A. T. Zehnder and A. J. Rosakis, *J. Mech. Phys. Solids*. **39**, 385 (1991).
- <sup>2</sup> J. A. Kallivayalil and A. T. Zehnder, *Int. J. Fracture*. 66, 99 (1994).
- <sup>3</sup> A. T. Zehnder and A. J. Rosakis, *Experimental Techniques in Fracture, III*, J. S. Epstein, (ed.), VCH publishers, 125 (1993).
- <sup>4</sup> H. Ay and W.-J. Yang, *Int. J. Heat Mass Transfer*, 41,613 (1998).
- <sup>5</sup> M. Zhou, A.J. Rosakis and G. Ravichandran, *J. Mech. Phys. Solids*, **44**, 981 (1996).
- <sup>6</sup> K. A. Hartley, J. Duffy, and R. H. Hawley, *J. Mech. Phys. Solids*, 35,283 (1987).
- <sup>7</sup> G.T. Camacho and M. Ortiz, *Comput. Method. Appl. M.* 142,269 (1997).
- <sup>8</sup> K. Bhalla and A.T. Zehnder, to be submitted to *Engineering Fracture Mechanics*, (2000).
- <sup>9</sup> Y. Wang, *Study of deformation and fracture of polymers and metals using infrared imaging methods*, Ph.D. thesis, Wayne St. University (1997).
- <sup>10</sup> R. Weichert and K. Schoenert, *J. Mech. Phys. Solids*. **26**, 151 (1978).
- <sup>11</sup> J. Hodowany, G. Ravichandran, A.J. Rosakis, and P. Rosakis, *GALCIT SM Report 98-7*, California Institute of Technology, Pasadena (1998).
- <sup>12</sup> R. Kingslake, *Lens Design Fundamentals*, Academic Press, New York (1978).

## List of Figures

1. Block diagram of million frames per second IR imaging system.
2. Photograph of system in place in front of a cracked, steel sample to be loaded in impact at 6 m/s.
3. Ray diagram of 1.3X reflective IR lens. The lens consists of two Schwarzschild objectives placed back to back, each used at infinite conjugation ratio. Magnification is given by the ratio of the focal lengths of the two objectives.
4. Transimpedance circuit used to amplify current from the IR detector elements.
5. Multiplexer block diagram.
6. Timing diagram for multiplexer and A/D board.
7. Calibration of IR detectors using 1.3X lens system and C-300 steel sample.
8. Schematic of notched C-300 steel drop weight impact experiment.
9. Temperature field for crack initiation (color image). a) Temperature field during loading (prior to crack initiation). b) Temperature after crack begins to grow. Peak temperatures move with crack tip. Note that temperature contours are linear interpolations.

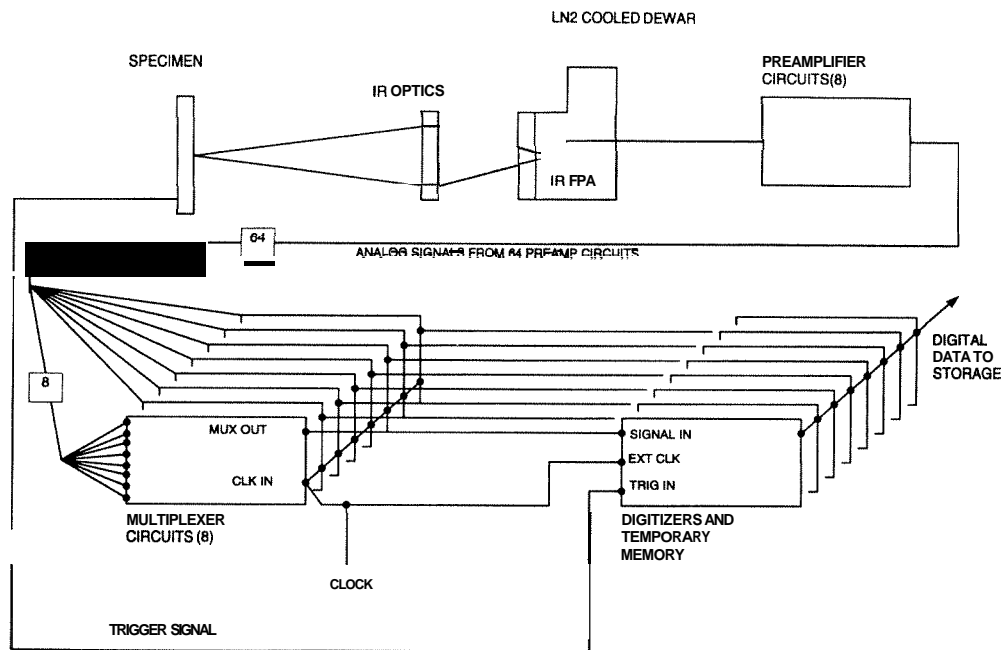


Figure 1

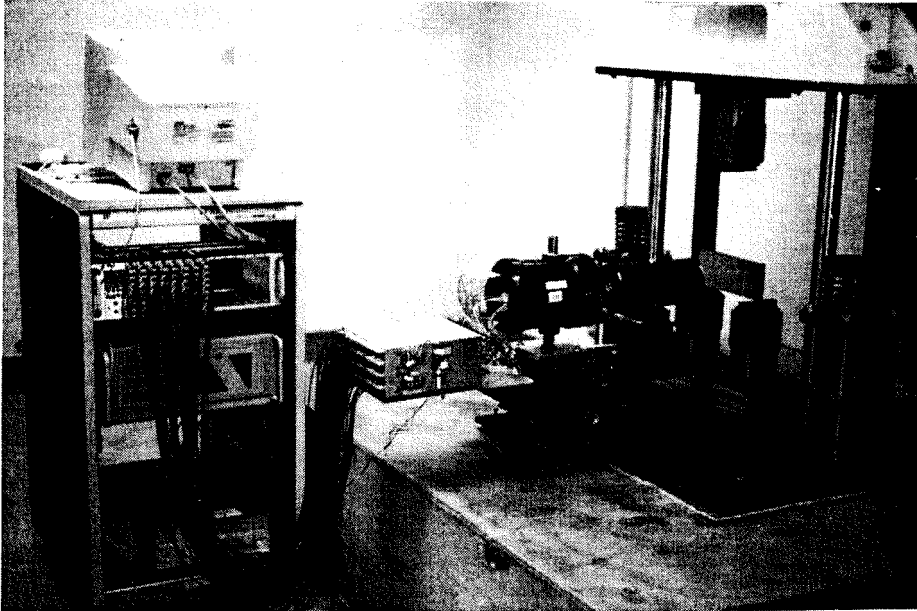


Figure 2

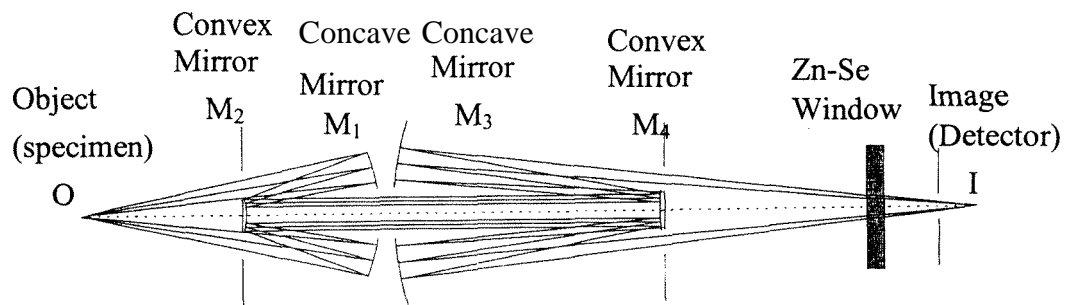


Figure 3

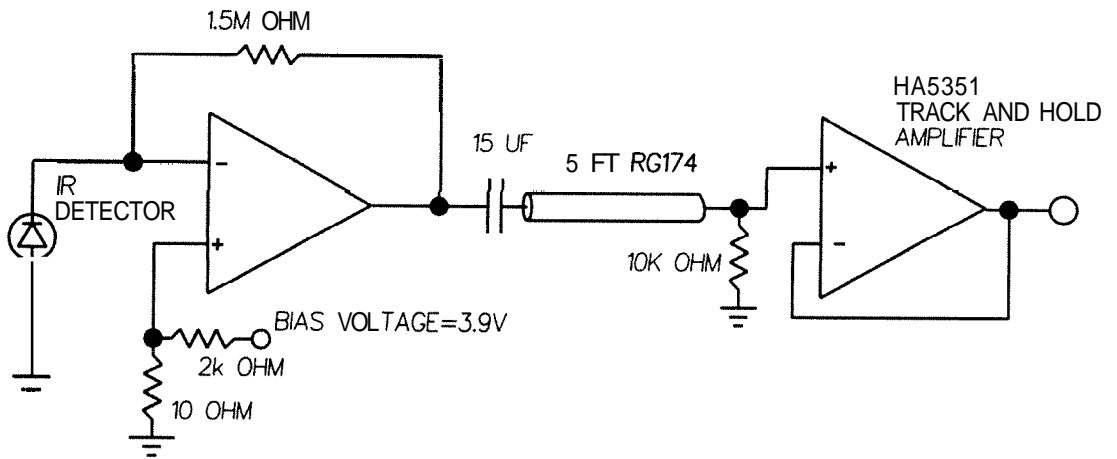


Figure 4

## INPUT SIGNALS

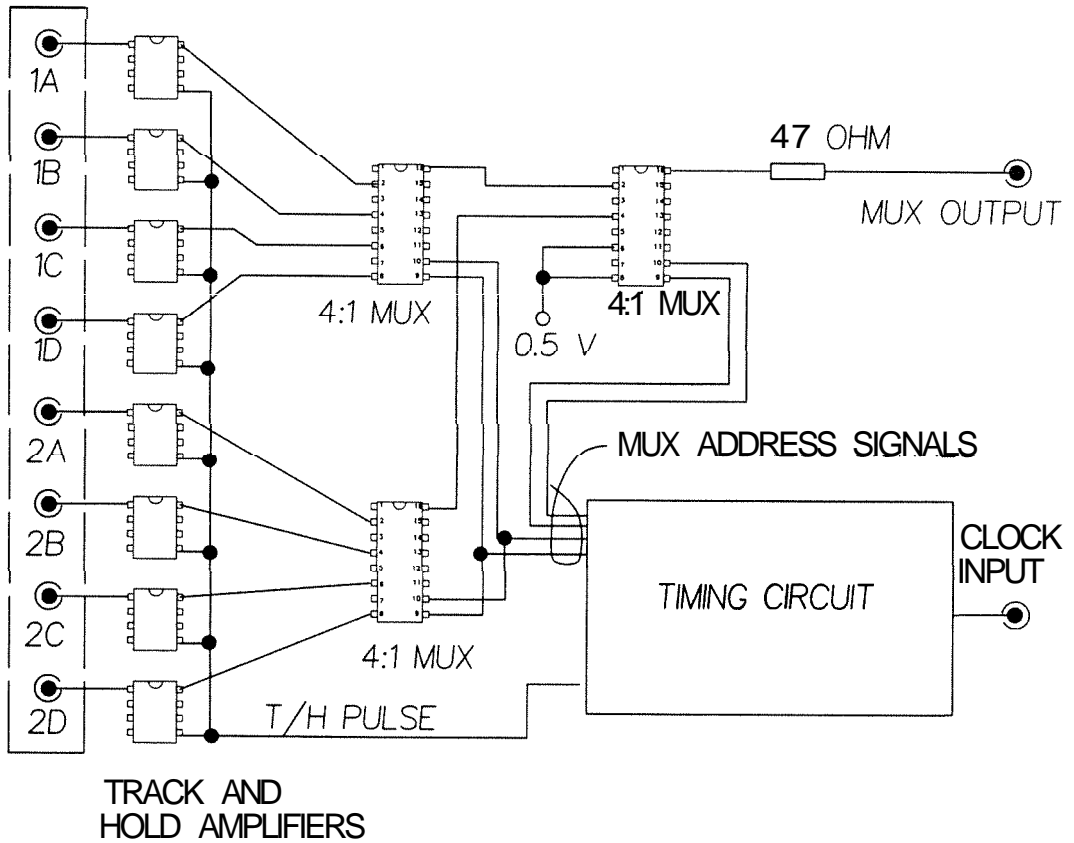


Figure 5

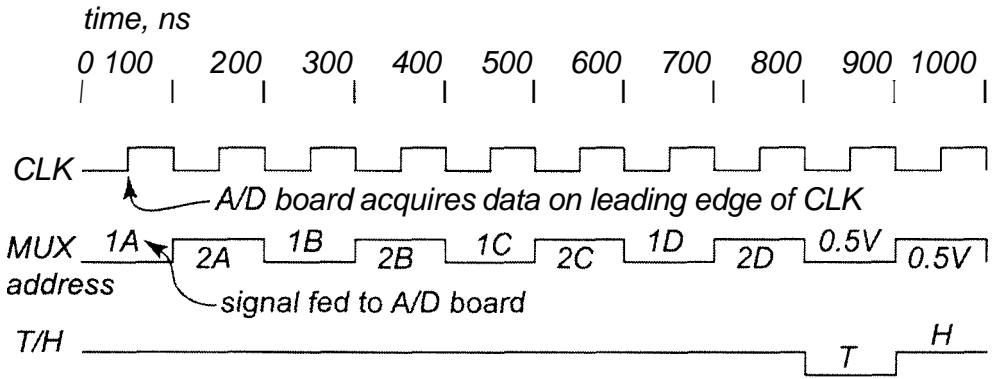


Figure 6

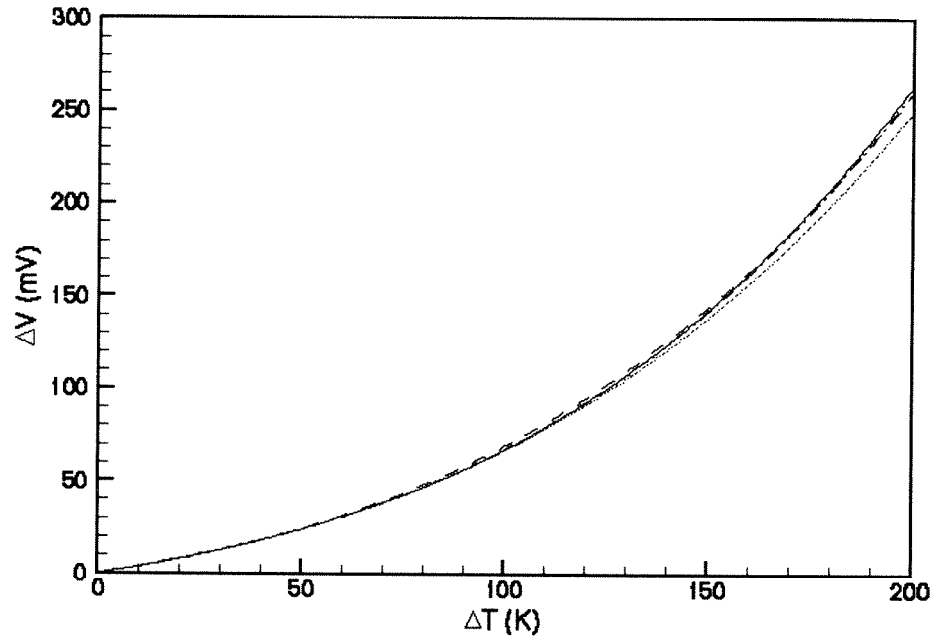


Figure 7

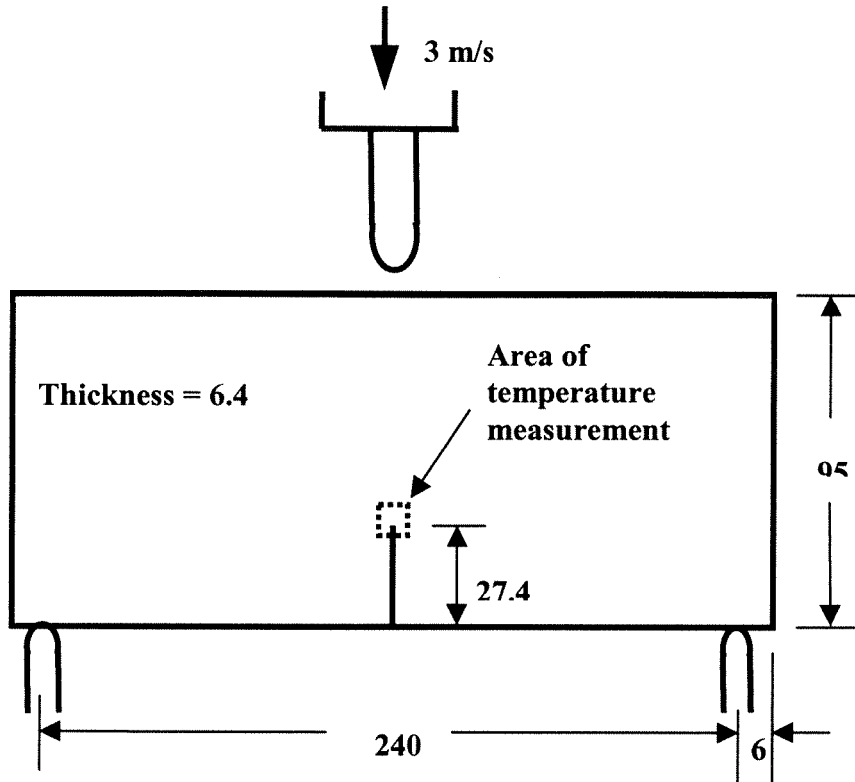


Figure 8

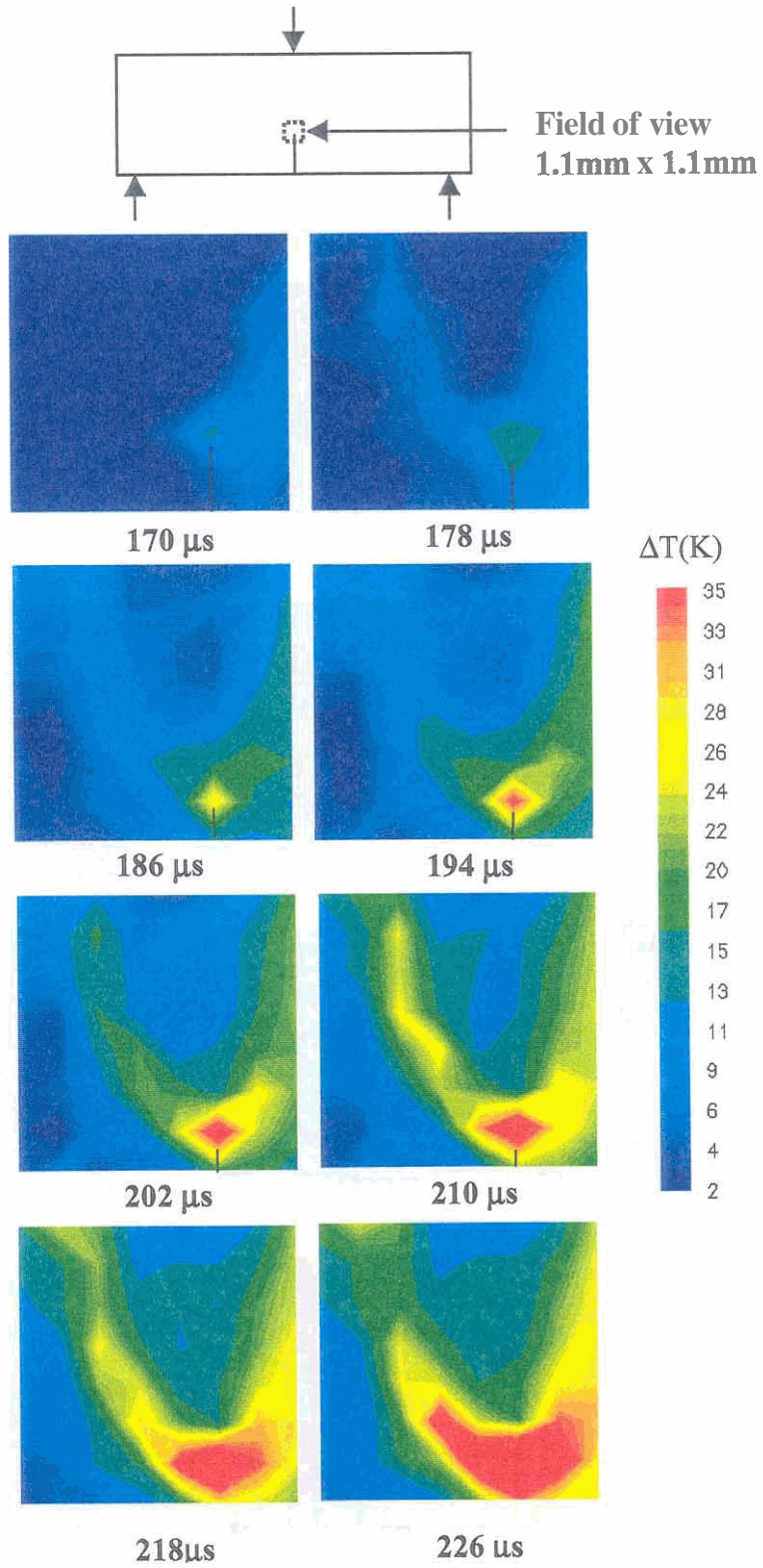


Figure 9a

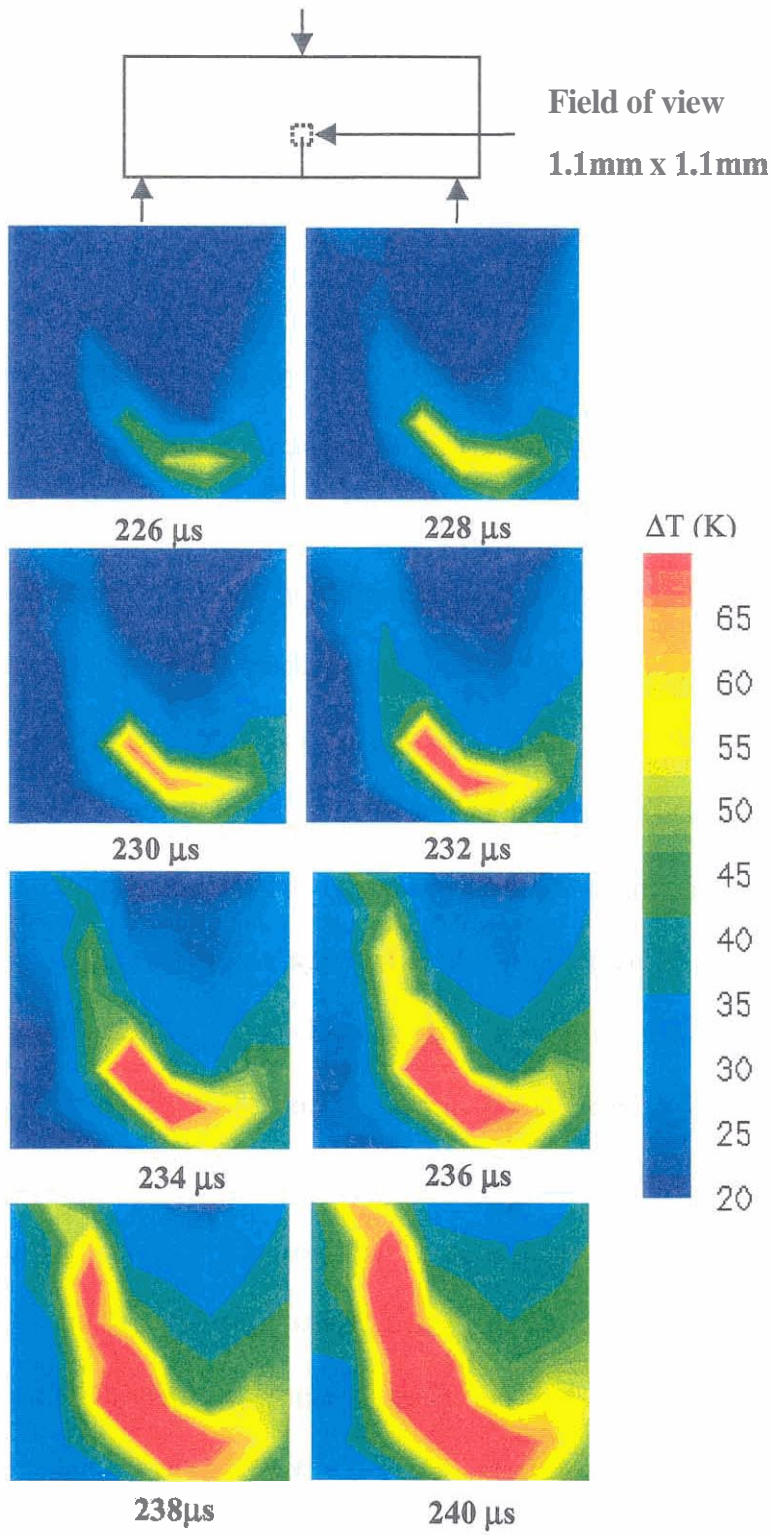


Figure 9b

## Chapter 2

### Dynamic Full Field Measurements of Crack Tip Temperatures

#### Abstract

Crack tip temperature rise during dynamic deformation is known to alter the fracture mechanisms and consequently the fracture toughness of a material. However, no direct experimental measurements have ever been made to quantify this effect because of the lack of appropriate diagnostic tools. In addition, although it has been common knowledge that the dynamic loading of the crack tip is achieved via the development of a plastic zone, there has never been any real time visualization of its development and the distribution of plastic dissipation in it. Further, the temperature rise in the vicinity of the crack tip could potentially be used as a direct measure of loading and could serve as a diagnostic tool in order to extract appropriate dynamic fracture parameters. Such a measurement would reflect crack tip loading more accurately than other conventional quantities such as boundary loads and the crack mouth opening displacement, under dynamic loading conditions. By transcending the existing experimental limitations, the present investigation presents detailed, real time images of the transient crack tip temperature fields in two different steels, using a 2-D high speed infrared camera, recently developed at Caltech. Experimental results are compared with the predictions of some analytical models. In case of ductile steels, a method to extract the critical  $J$  integral from the temperature measurements is discussed.

## 2.1 Introduction

In addition to inertia and strain rate sensitivity effects, the temperature rise at the tip of a stationary crack subjected to dynamic loading could significantly alter its resistance to initiation. As discussed by Freund (1990), strain rate and temperature can have opposing effects on the fracture toughness vs. loading rate relation, with higher strain rates resulting in decreasing toughness because of material rate sensitivity and higher temperatures having the opposite effect. If the loading rate were high enough, local heating in a crack tip plastic zone would be nearly adiabatic. The increase in the temperature within the fracture process zone directly affects the micromechanisms of fracture, by modifying the local constitutive relation, resistance to void growth process, etc. Kraft and Irwin (1965) attempted to estimate the temperature rise at the crack tip in three different materials, a titanium alloy, a steel and an aluminum alloy, by examining their fracture toughness behavior over a range of loading rates and at different temperatures. The temperature rise they predicted was typically less than 120°C. By treating a growing plastic zone as a distributed source of heat, Rice and Levy (1969) estimated the maximum temperature rise at the tip of a crack at initiation would be 120°, 60° and 80°C for the above three materials, which was in good agreement with the experimental results. By assuming that the fracture behavior of a specimen at a given temperature would be the same as that of a specimen whose crack tip process zone is at that temperature, they proposed a model to predict the fracture toughness vs. loading rate relation. Their work, for the first time, underlined the importance of considering the effects of temperature rise at the tip of a stationary crack subjected to rapid loading on its

fracture resistance. Crack tip temperature as a parameter affecting the fracture processes was also considered by Jha and Narasimhan (1992) and by Basu and Narasimhan (1999). Using a 2-D plane strain finite element model, employing finite deformations, to analyze the crack initiation in 4340 steel, Jha and Narasimhan (1992) estimated that the temperature near the crack tip at initiation could be as high as 230°C. In addition, as discussed by Freund (1990), temperature at a crack tip could bring about a complete change in the mechanisms of fracture, an effect which was conclusively demonstrated by the experiments of Wilson *et al.* (1980). In spite of such early analytical and numerical demonstrations of the potentially significant role of the crack tip temperature in determining the mechanisms of fracture, there has been very little effort to accurately measure the evolution of temperature fields at the crack tip. This can be traced to the particular experimental difficulties that would be encountered in such an effort. Typical dynamic crack initiation experiments are very rapid events, happening at time scales ranging from few tens of microseconds to a few milliseconds at the most. In addition, the size of a typical fracture process zone ahead of a crack tip is of the order of the critical crack opening displacement, which ranges from tens of microns to a few hundreds of microns for most structural materials. Making accurate measurements of such highly dynamic and transient temperatures at such small length scales, severely limits the choice of experimental techniques to either fast response thermocouples or to infrared (IR) thermography. However, even tiny thermocouples of 100 $\mu\text{m}$  bead diameter have a response time of about a millisecond rendering them unsuitable for the current application. High speed IR detectors have been successfully used in the past by several investigators to measure temperature rise during dynamic deformation in materials. The

IR detectors that have been used are of either a single element type or a linear array of 8-16 detectors variety, with each detector averaging temperature over a spot, the size of which ranged from 20 $\mu$ m to a few hundred microns. However, their use has been limited to experimental situations where the location of the temperature measurement spot did not have to be very precise. In dynamic experiments, it is nearly impractical to focus these detectors at a tiny spot such as a crack tip process zone, due to high speed impact induced vibrations and deformation and thus are not very suitable for crack tip temperature measurement. One way to effectively overcome such problems would be to use a two-dimensional IR camera with a high speed data acquisition capability and with a spatial resolution of the order of 100 $\mu$ m. We explore this idea in the current investigation.

In addition to the significance of crack tip temperatures mentioned above, temperature fields within the crack tip plastic zone could potentially be used as a diagnostic tool to measure the crack tip loading parameters such as the dynamic **J** integral, under certain conditions. By identifying the critical time of crack initiation, the critical value of **J** integral can then be inferred. This idea was introduced and explored by Guduru *et al.* (1998) by deriving a relation between the **J** integral and the crack tip temperature field using the HRR singular field (Hutchinson, 1968; Rice and Rosengren, 1968) within the plastic zone and assuming adiabatic conditions. They used a single element HgCdTe IR detector, to measure the average temperature rise over an area of 300 $\mu$ m x 300  $\mu$ m on the specimen in front of the crack tip, and used it to estimate the evolution of the **J** integral in a drop weight impact experiment on HY100 steel in a three point bend configuration. Despite the novelty of the experimental technique, the accuracy

of their measurement was limited by the relatively large area of temperature averaging, uncertainty in locating the area of measurement in relation to the crack tip and the rigid translation of the specimen during deformation. In order to pursue this idea further by transcending the stated limitations, a comprehensive investigation to map the entire crack tip temperature fields has been undertaken using a 2-D high speed IR camera, recently developed at Caltech. Full field thermal images of plastic zone evolution are first presented. Subsequently, the measured temperatures are used to estimate the evolution of the  $J$  integral and the issues related to  $J$  dominant stress-strain fields within the plastic zones are discussed.

## 2.2 Experiments

### 2.2.1 Material

Temperature rise at the crack tip and within the plastic zone is investigated in two steels, featuring very different mechanical properties. One of them was a C300 maraging steel, which is an ultra high strength martensitic steel, with yield stress of about 2GPa. Its chemical composition is shown in Table 1. The specimens were cut from a plate of 6.5mm in thickness, and the heat treatment involved age hardening, by holding them at 482°C for five hours, followed by air cooling. The mechanical properties of the age hardened C300 maraging steel can be found in Zhou et *al.* (1996b). The mode I fracture toughness of C300 steel is about 88 Mpa m<sup>1/2</sup>. In opening mode, these specimens undergo flat fracture over most of the specimen thickness, with thin shear lips (~1mm) on either

side. The flat fracture region shows void growth and coalescence. The other steel is a highly ductile, medium strength, HY100 steel, the chemical composition of which is shown in Table 2. Its static yield strength is 800MPa. The heat treatment involved holding at 900°C for 16 minutes followed by water quenching. The steel was then tempered by holding at 638°C for 50 minutes. As will be shown later, HY100 has a very high fracture toughness and does not satisfy small scale yielding conditions in the specimen geometry used in this investigation. The typical mode I fracture surface consists of a small triangular tunneled area ahead of the crack tip, which soon gives way to shear lips covering the entire thickness. A discussion of the ductile fracture mechanisms in HY100 steel can be found in Venkert et al. (2000). HY100 displays substantial rate sensitivity, with an increase of about 20% in yield stress at a strain rate of 3000/s compared to its value at a rate of 0.01/s. A detailed constitutive description of HY100 can be found in Zhuang and Ravichandran (1998).

## **2.2.2 Experimental Technique**

### **2.2.2.1 Infrared imaging**

Discrete infrared (IR) measurements has been used for measuring temperature rise in dynamic deformation and failure experiments by many investigators in the past (Moss and Pond, 1975; Costin et al. 1979; Hartley et al. 1987; Marchand and Duffy, 1988; Zehnder and Rosakis, 1991, 1992; Mason and Rosakis, 1993; Zehnder et al., 1993; Kallivayalil and Zehnder, 1994; Zhou et al., 1996a; Guduru et al., 1998; Hodowany et

al., 2000; Li and Lambros, 2000). All investigations conducted so far have utilized either a single element detector or a linear array of detectors with wither 8 or 16 sensing elements. Using a linear array of detectors, it is possible to measure temperature at a series of discrete points along a line on the specimen surface. Such detectors have been successfully used by Zehnder and Rosakis (1991) and by Mason and Rosakis (1993) to measure the temperature rise across a propagating opening crack in a high strength steel. Costin *et al.* (1979), Hartley *et al.* (1987), Marchand and Duffy (1988), Zhou *et al.* (1996a) used them to measure the temperature rise across a propagating shear band in steels. However, the linear arrays of detectors are ideal to measure temperature distribution across features that are essentially one-dimensional and steady. Although a great deal of information can be obtained with these linear arrays, given the highly transient two-dimensional nature of most dynamic events in solids, including the crack tip temperature fields, it is desirable to have an instrument that can measure temperature fields over an area instead of at discrete points along a line. Since several events involving dynamic deformation in solids occur at time scales of tens of microseconds, such measurements can be accomplished using a two-dimensional array of fast response IR detectors acquiring images at rates of around 1MHz.

Although there have been great advances in 2-D, quasi-static, infrared (IR) imagery in recent years, there are currently no commercial systems capable of imaging at such high speeds. Available IR imaging systems typically run at television rates, 30 Hz, although higher speed systems do exist, with rates of up to 34kHz. Achieving the required framing rates of up to 1MHz necessitates very fast and temporally frozen data

acquisition in conjunction with a high-speed 2-D IR detector array. The bottleneck in performing such measurements has been data acquisition. However, utilizing the fast, relatively inexpensive digitizers which are now available, a 2-D IR imaging system has been designed and built at Caltech. This instrument, for the first time, enables the measurement of transient thermal fields at rates of up to 1 million frames per second. The complete imaging system, consisting of the focusing optics, an IR focal plane array, multiplexing circuits, and data acquisition boards is shown in the block diagram of Fig. 1. At the heart of the system is an 8x8 focal plane array of HgCdTe IR detector elements. Each detector element is  $100\mu\text{m} \times 100\mu\text{m}$ , with center to center spacing of  $130\mu\text{m}$ . Each of the 64 elements has its own preamplifier, the outputs of which are fed into a bank of eight 8:1 multiplexers. The multiplexed signals are then digitized using 4 two-channel, Gage 1012 A/D boards, running at speeds up to 10MHz. Radiation emitted from the object as it deforms and heats up is focused onto the IR focal plane array using a reflective lens, built up out of two Schwarzschild objectives, each operating at infinite conjugation ratio. The ray diagram for the focussing optics is shown Fig. 2. A photograph of the camera consisting of the focussing optics and the liquid nitrogen dewar housing the detectors, is shown in Fig. 3. The magnification of each lens is fixed. To achieve different magnifications, different lenses are used. In the current investigation, a magnification of 0.9 was used to investigate the crack tip temperature field in C300 steel and a magnification of 0.48 for HY100 steel. The choice of magnification is governed by the size of the area that needs to be imaged at a specific resolution, which in turn is related to the size of the plastic zone in each case. For C300, the size of the plastic zone at crack initiation is less than 1mm and at a magnification of 0.9, the IR camera would

image an area of 1.1mm x 1.1mm. In such a case, each detector measures average temperature over an area of 110  $\mu\text{m}$  x 110  $\mu\text{m}$ . For HY100, the size of the plastic zone at initiation is around 10mm, which is too large for the lens systems designed for the camera. Instead, it was decided to observe an area of 2.1mm x 2.1 mm close to the crack tip using a magnification of 0.48. At this magnification, each detector averages temperature over an area of 210 $\mu\text{m}$  x 210 $\mu\text{m}$ . In this system, there is no integration of the signal between frames as in commercial IR cameras; thermal resolution is sacrificed in favor of speed. The system rise time is approximately 750ns. The details of each of the components of the system and the results of some preliminary applications of the system are given in Zehnder *et al.* (2000). It was experimentally found that the system cross talk is about 12%. As a result, if the image of a thin (~75 $\mu\text{m}$  diameter) hot wire is focussed on a row of detectors, the neighbouring row of detectors also responds, even though no signal is expected out of it. The signals from the neighbouring row are about 12% of the signals from row on which the image is focussed. The sources of cross talk are electronic and optical in nature. The former is due to the electronic coupling between the neighbouring detectors on the array. Optical cross talk arises because of imperfect optical focussing, owing to various aberrations in the focussing system as well as imperfections in assembling the system. A procedure to correct for the cross talk is detailed in Zehnder *et al.* (2000). However, no attempt has been made here to correct for the cross talk. As a consequence, the thermal images obtained would be somewhat blurred images of the actual temperature fields on the specimen. In order to convert the voltage signals from the detectors to corresponding temperatures on the specimen, an output signal vs. temperature calibration curve must be obtained for the detectors.

### 2.2.2.2 *IR System calibration*

Calibration of the system is performed in a very direct manner. A sample of the same material and surface finish as will be tested is heated in an oven by several hundred degrees. The heated sample, instrumented with a thermocouple to record its surface temperature, is placed in the object position. As the sample cools, the voltage output from each of the IR elements is recorded by the data acquisition system along with the sample temperature. This procedure provides a voltage vs. temperature curve for each element. Since the IR system is AC coupled, the input radiation to the detectors must contain an AC component. This is achieved by placing a chopping wheel in front of the heated calibration specimen.

Great care should be exercised during the calibration procedure since any errors made at this stage are directly reflected in the final measurements. Further, oxidation of the sample surface when heated to high temperatures during calibration changes its emissivity substantially, rendering the calibration curve inapplicable. The ideal way to overcome the oxidation problem is to perform the calibration in vacuum or in an inert gas atmosphere, both of which are experimentally cumbersome procedures. As an alternative, the following procedure has been adopted. First, the sample was heated up to a temperature at which no oxidation takes place on its surface, about 225°C in the case of C300, and a calibration is performed while it cools down to room temperature. In order to

verify that indeed no oxidation has taken place, the same sample, without modifying the surface condition in anyway, is heated repeatedly to 225°C and the calibration curves are obtained. The curves obtained in four such repetitions for C300 steel, for one of the 64 detectors, are shown in Fig. 4. The proximity of all of them to each other confirms that there was no oxidation up to 225°C. Next, the specimen was heated to a higher temperature, 525°C, and a calibration was performed while the specimen cooled down. This curve, along with the curve obtained by heating the specimen up to 225°C, is shown in Fig. 5. The ratio of these curves to each other represents the ratio of the emissivities of the two surfaces. This ratio is plotted as a function of temperature rise in Fig. 6. It can be seen that this ratio, after some initial non-linearity, settles down to a constant value 1.55, which is essentially the ratio of the emissivity of the oxidized surface to that of the non-oxidized surface. The calibration curve corresponding to the non-oxidized surface is then extended to higher temperatures by simply dividing the calibration curve of oxidized surface by the factor 1.55. Similar calibration procedure was followed for HY100 steel also. It should be noted that during a dynamic experiment, the temperature elevations of interest happen at such short time intervals that oxidation does not have the time to build up during the observation window.

## **2.2.3 Specimen Geometry and Loading Arrangement**

### **2.2.3.1 C300 Maraging steel**

The specimen geometry and loading arrangement are schematically illustrated in Fig. 7. The specimen was loaded in a three point bend configuration under a drop weight tower (Dynatup 8100A), with a tup mass of 250 kg. The impact speed was 3 m/s. A notch, 260 $\mu$ m wide and 25.4 mm long, was cut on the edge using electric discharge machining (EDM). The notch was subsequently extended by 2 mm by fatigue loading, in order to produce a sharp crack. Temperature rise during the deformation was measured in a small area of 1.1mm x 1.1mm around the crack tip, as shown in Fig. 7. A photograph of the experimental arrangement consisting of the drop weight tower, the specimen, IR camera, amplifier bank and the data acquisition system, is shown in Fig. 8.

#### 2.2.3.2 *HY100 steel*

Loading HY100 specimens in a simple three point bend configuration as in the case of C300 steel, presents certain experimental difficulties for temperature measurement. In a three point bend arrangement, as the tup tries to bend the specimen, the crack tip translates downwards at about half the speed of the tup, i.e., 1.5 m/s in the C300 steel experiment. As a result, each detector on the IR camera measures temperature, not at a single targeted point on the specimen, but at several different points as they translate past the field of view of the detectors. This would not be a major problem if the total translation prior to crack initiation were small compared to the size of the field of view of the camera. For example, in the case of C300 steel, crack initiates around 200 $\mu$ s, during which time, the crack tip travels about 300  $\mu$ m downwards, which is small compared to the size of the field of view. However, since, HY100 steel is a lot more

ductile, crack initiation takes place after a substantially larger translation, compared to the size of the field of view. Thus, in order to load the specimen in mode I, without any crack tip translation, a specimen geometry was designed as shown in Fig. 9. This is a modification of the geometry used by Zehnder and Rosakis (1991). The loading is produced by driving a wedge which separates two pins that open the crack in mode I. The bottom of the specimen is securely clamped to a rigid base in order to prevent any translation. The load to drive the wedge is provided by placing the specimen-wedge assembly under a drop weight tower or impacting the wedge with a projectile accelerated in a gas gun. For HY100 steel, two loading rates were used. First, the specimens were subjected to drop weight impact at a speed of 4 m/s. To achieve a higher rate of loading, it was subjected to a 50 m/s projectile impact. The cylindrical steel projectile used was 50mm in diameter and 127mm long. A schematic of the latter experimental arrangement for gas gun impact is shown in Fig. 10.

## **2.3 Results**

### **2.3.1 C300 Steel**

#### *2.3.1.1 Temperature images*

Two sequences of thermal images obtained, showing the initiation and propagation of the crack respectively, are shown in Figs. 11 and 12. It should be recalled that the temperature is measured at 64 discrete points. The images shown are the

projections on the  $x_1$ - $x_2$  plane of the contour lines on a surface fitted through the 64 points in the  $x_1$ - $x_2$ - $\Delta T$  (temperature rise) space. In Fig. 11, starting about 170 $\mu$ s after impact, a plastic zone can be seen building up. A black line is artificially superimposed on these images to indicate the supposed approximate location of the crack. The position of the crack is inferred from the temperature patterns. In spite of some initial asymmetry, the plastic zone builds up almost symmetrically and gradually up to 226 $\mu$ s. The first image in Fig. 12 is the same as the last one in Fig. 11, shown at a different temperature scale. Beyond 226 $\mu$ s, an asymmetry in temperature distribution can be seen to build rapidly, which is the result of the process of crack growth. The red band of high temperatures in the latter images of Fig. 12 is actually the intersection of the shear lip with the free surface. The temperatures at the center of the band reach as high as 200°C. This is the first time that such images showing the process of crack initiation and propagation, detailing the shape and growth of the plastic zone and its temperature structure within, in real time, have been obtained. From Fig. 11 and Fig. 12, it can be concluded that 226 $\mu$ s is the time of crack initiation and that the maximum temperature rise at the crack tip at initiation is around 55°C. However, each IR detector averages temperature over an area of 110 $\mu$ m x 110 $\mu$ m. Since the temperature gradients are expected to be high near the crack tip, the maximum local temperature could actually be higher than 55°C.

### 2.3.1.2 *Comparison with the Rice and Levy model*

Rice and Levy (1969) (RL) modeled the temperature rise at the tip of a stationary crack for small scale yielding, using the plane strain slip line analysis and the  $\mathbf{J}$  integral. The slip line analysis gives the rate of plastic dissipation within the plastic zone to be

$$\dot{W}^p = \frac{\tau_o^2}{\mu r} \cos 2\left(\theta - \frac{\pi}{2}\right) \dot{\omega} \quad (1)$$

where  $\tau_o$  is the shear yield stress,  $\mu$  is the shear modulus,  $(r, \theta)$  are the crack tip polar coordinates, with  $\theta = 0$  denoting the crack line ahead of the tip and  $\omega$  is the maximum extent of the plastic zone, which is given by

$$\omega = \frac{3(1-\nu)}{\sqrt{2}(2+\pi)} \left( \frac{K}{2\tau_o} \right)^2 \quad (2)$$

where  $\nu$  is the Poisson's ratio and  $K$  is the far field stress intensity factor. Before considering the complete heat conduction analysis of RL, let's first assume adiabatic conditions and estimate the temperature rise. For adiabatic conditions, eq. (1) can be integrated directly. Using eq. (2) and by assuming that all of plastic work is converted into heat, the temperature rise near the crack tip at initiation can be estimated to be

$$\Delta T = \frac{2.23}{r} \quad (3)$$

where  $r$  is in millimeters. The following values have been used in the above calculation.  $K = 88 \text{ MPa m}^{1/2}$ ;  $\tau_o = 1 \text{ GPa}$ ;  $\mu = 70 \text{ GPa}$ ;  $\nu = 0.3$ ;  $\rho = 8000 \text{ kg/m}^3$ ;  $c = 450 \text{ J/kg/K}$ ; and

$\theta = \pi/2$  for an upper bound estimate. Since each IR detector averages temperature over a spot of size  $110\mu\text{m} \times 110\mu\text{m}$ , it would be appropriate to compare the measured crack tip temperature with an estimate from eq. (3), using  $r = 55\mu\text{m}$ , which yields  $\Delta T = 41^\circ\text{C}$ . This compares very well with the measured value of  $55^\circ\text{C}$ . However, as RL pointed out, since the temperature distribution according to this analysis has a  $1/r$  singularity, the crack tip would never be under truly adiabatic conditions. RL solved the heat conduction problem for the crack tip temperature rise, by considering the heat generated over the entire plastic zone for the plane strain slip line model. The solution is given below.

$$\Delta T = \left( 0.156 \frac{(1-\nu^2)K^2}{E\sqrt{\rho ck\tau}} \right) h(\delta) \quad (4)$$

where  $\tau$  is the time for the stress intensity factor to increase from 0 to its critical value of  $88 \text{ MPa m}^{1/2}$ , which is about  $200\mu\text{s}$  in this case.  $k$  is the coefficient of thermal conduction,  $36 \text{ W/m/K}$ .  $h(\delta)$  is a dimensionless function that depends on the dimensionless parameter  $\delta$  which is a measure of the shortness of the time to reach the maximum stress intensity factor and is defined as  $\delta = 2\sqrt{\alpha\tau}/a$ , where  $a$  is the thermal diffusivity,  $10^{-5} \text{ m}^2/\text{s}$ . For the values listed above,  $\delta = 0.16$ , for which  $h(\delta)$  is 0.85 from RL. Using these values in eq. (4), the crack tip temperature rise is estimated to be approximately  $30^\circ\text{C}$ . Though RE model predicts the crack tip temperature to the correct order, it is an underestimation of the actual value of  $55^\circ\text{C}$ . The discrepancy can be attributed to the assumptions made in using the model for the present case. The model was developed for the case of plane strain, which is not exactly a valid state at the specimen free surface, where the

conditions are closer to plane stress. For a given stress intensity factor, the strains are higher for plane stress, leading to higher temperatures as observed in the experiment. The crack tip finite strains could be another factor, which are not considered in RL model. Away from the crack tip, adiabatic conditions are expected to be a better approximation. Hence, the adiabatic model discussed above can be used to predict the temperature rise there. According to eq. (3), the temperature rise falls rapidly to about 2°C at a distance of 1mm from the crack tip. This seems to agree very well with the experiment as can be discerned from the last two images of Fig. 11.

It is generally known that when a specimen is subjected to mode I loading, the conditions at the free surface would be close to a plane stress situation and the conditions at the mid-plane would be close to a plane strain situation. Thus it was surprising to find the temperature contours at the specimen surface, as observed by the IR camera, have a characteristic U shape near the crack tip, whereas, such a shape is typically associated with a plane strain plastic zone. An explanation for this can be found from the 3-D numerical investigations of the shapes of the plastic zones of statically loaded three point bend 4340 steel specimens (Narasimhan and Rosakis, 1990) (NR). 3-D numerical simulations of thin metal plates were also conducted by Nakamura and Parks (1990) and similar results were reported. The numerical simulations revealed that the contours of equivalent stress within the plastic zone, at the free surface, actually show a characteristic U shape that was observed in the experiments. A qualitative comparison of the results of NR with the current experiment is shown in Fig. 13. Fig. 13a is a thermal image at the time of crack initiation and 13 b shows the contours of equivalent stress within the plastic

zone for a 10mm thick 4340 steel plate, with a yield stress of 1030 MPa and loaded to a stress intensity factor of  $280 \text{ MPa m}^{1/2}$ . The figure also shows the corresponding adiabatic temperature rise values along the contours, which were not originally reported by NR, but were calculated here for the purpose of comparison. Given the difference in the material properties, loading conditions and the experimental geometry, it is not possible to make a direct quantitative comparison between the two. However, two observations can be made. The equivalent stress contours indeed show the characteristic U shape near the crack tip, which is supported by the experiments. Such a shape is a consequence of the presence of the free boundary. In case of the numerical simulation, the applied K is almost three times that in the experiment and the yield stress is only one-half of that of C300 steel. Hence, crack tip plastic zone length scale is approximately 36 times bigger in the simulation compared to that in the current experiment, which accounts for the big difference in size between Fig. 13a and 13b. This difference in length scale also provides a way to compare the two pictures appropriately, by scaling down Fig. 13b by the factor 36. Thus the plastic zone shown in Fig. 13b is about  $600\mu\text{m} \times 600\mu\text{m}$  when scaled down, and the temperature contour values are indeed within the order of magnitude of the measured values.

## **2.3.2 HY100 Steel**

### *2.3.2.1 Temperature images*

A sequence of thermal images obtained in the drop weight tower experiment with an impact speed of 4m/s is shown in Fig. 14. A plastic zone can be seen growing beginning at 950 $\mu$ s. The peak temperatures observed are significantly higher than those observed in C300 steel. The maximum temperature at the crack tip in the last image is around 90°C. This is expected because of the extensive plastic deformation HY100 can sustain prior to failure. Once again, the familiar U shaped temperature rise contours close the crack tip can be observed. One of the persistent difficulties in the study of the dynamic fracture of ductile metals has been the reliable identification of crack initiation time. In the past a variety of techniques have been used to identify crack initiation with varying success. In the current investigation, the following procedure has been followed to identify crack initiation. Fig. 15b shows the temperature signals for 5 individual detectors, located along a line ahead of the crack, as shown schematically in Fig. 15a, for the drop weight tower experiment. The area shown in Fig. 15a is the field of view of the IR camera and the digits denote the individual detectors along the column that is directly ahead of the crack tip. The temperature signals increase steadily at the beginning and at around 1600 $\mu$ s, show a marked increase in slope. This increase in slope can be associated with crack initiation in the form of tunneling at the center of the specimen. Initially when the crack tip is loaded, the region in front of the crack tip throughout the thickness is plastically deformed and the temperature increases. However, when crack initiation begins in the form of tunneling at the mid-plane of the specimen, subsequent deformation gets concentrated in the two ligaments on either side of the tunnel. Thus the rate of plastic deformation on the specimen surface in front of the crack tip increases following

tunneling, resulting in an increase in the slope of the temperature signals seen in Fig. 15b. From this figure, the crack initiation event can be identified to be at 1600 $\mu$ s.

A sequence of images, obtained from the gas gun experiment with an impact speed of 50m/s is shown in Fig. 16. As before, failure initiation can be identified to be around 140 $\mu$ s, from Fig. 17a and b. Failure occurs an order of magnitude faster here compared to the drop weight tower experiment. The small flat portion of the temperature signals following initiation suggests the highly dynamic nature of the initiation event, resulting in momentary unloading before further plastic deformation. One major difference between the two experiments is the maximum crack tip temperature rise at the time of initiation. It is approximately 90K in the drop weight experiment and about 150K in the gas gun experiment. The explanation for this lies in the rate induced elevation of resistance to crack initiation. To investigate this issue further, the measured temperature signals were used to estimate the evolution of an appropriate fracture parameter. Following Guduru et al. (1998), it was assumed that the HRR stress-strain field characterized by the  $\mathbf{J}$  integral exists around the crack tip area and the measured temperatures were used to estimate the evolution of the  $\mathbf{J}$  integral and its critical value at initiation. The calculations are also used to check the assumption about the existence of the HRR field.

### 2.3.2.2 *J* integral estimation

### *Asymptotic stress field*

Hutchinson (1968) and Rice and Rosengren (1968), considered the case of a monotonically loaded stationary crack in a material described by a  $J_2$ -deformation theory of plasticity and a power hardening law. They showed that the strain and stress components in the crack tip region scale with the value of the J-integral. Within the small strain assumption, an asymptotic solution of the elastic-plastic field equations in the crack tip region has the form

$$\varepsilon_{ij} \rightarrow \varepsilon_0 \left[ \frac{J}{\sigma_0 \varepsilon_0 I_n r} \right]^{\frac{n}{n+1}} E_{ij}(n, \theta) \quad (5)$$

$$\sigma_{ij} \rightarrow \sigma_0 \left[ \frac{J}{\sigma_0 \varepsilon_0 I_n r} \right]^{\frac{1}{n+1}} \Sigma_{ij}(n, \theta) \quad (6)$$

Here,  $\sigma_0$  is the tensile yield stress,  $\varepsilon_0$  is the equivalent tensile yield strain,  $n$  is the hardening exponent, and the angular factors  $\Sigma_{ij}$  and  $E_{ij}$  depend on the mode of loading and the hardening exponent. The dimensionless quantity  $\mathbf{I}$ , was defined by Hutchinson (1968).

### *Temperature rise associated with the HRR singular field*

Consider an elastic-plastic isotropic homogeneous material with constant thermal conductivity. The heat conduction equation can be written as (Rosakis *et al.* 2000)

$$k\nabla^2 T - \eta(3\lambda + 2\mu)T_0 \dot{\varepsilon}_{kk}^e + \beta \sigma_{ij} \dot{\varepsilon}_{ij}^p = \rho c \dot{T} \quad (7)$$

where  $k$  is the thermal conductivity,  $T$  is the absolute temperature,  $\eta$  is the coefficient of thermal expansion,  $\lambda$  and  $\mu$  are Lamé constants,  $T_0$  is the initial temperature,  $\varepsilon_{ij}$  and  $\sigma_{ij}$  are the Cartesian components of the strain and stress tensors respectively,  $\rho$  is the mass density and  $c$  is the specific heat.  $\beta$  is the fraction of plastic work density rate  $\dot{W}^p = \sigma_{ij} \dot{\varepsilon}_{ij}^p$ , dissipated as heat. Assuming that the elastic strain components are small compared to the plastic strain components, the thermoelastic term in the above equation can be neglected. If the process is assumed to be adiabatic, the above equation reduces to

$$\frac{\beta}{\rho c} \sigma_{ij} \dot{\varepsilon}_{ij}^p = \dot{T} \quad (8)$$

Substituting (5) and (6) into (8) and integrating with time, we have

$$J(t) = \frac{\rho c I_n}{\beta} \left( \frac{n+1}{n} \right) \frac{r}{\Sigma_{ij}(\theta, n) E_{ij}(\theta, n)} \Delta T(r, \theta, t) \quad (9)$$

This equation provides a direct relation between the temperature rise at a point within the plastic zone and the  $J$  integral. Plane stress values of the angular functions and  $I_n$  are used, with a value of 8 for  $n$ . The value of  $\beta$  is assumed to be 1.0. This calculation is illustrated in Fig. 18 for the drop weight tower experiment. Using the temperature rise at

points that are directly ahead of the crack tip, the  $J$  integral as calculated from eq. (9) is plotted as a function of the distance from the crack tip, at different times, separated by  $200\mu\text{s}$ . If there were complete HRR field dominance everywhere near the crack tip, each line would be a straight horizontal line, corresponding to the value of  $J$  at that instant. The figure shows that it is almost constant beyond a certain distance from the crack tip, indicating the existence of the HRR field there. At  $1600\mu\text{s}$ , which is the approximate time of crack initiation,  $J$  has a value of about  $850\text{ kPa m}$ . The calculation is repeated for the gas gun experiment and is shown in Fig. 19 and the critical  $J$  in this case can be deduced to be about  $1225\text{ kPa m}$ . This elevation in the critical  $J$  accounts for the substantial increase in the crack tip temperature in the higher impact speed experiment. In order to demonstrate the nature of temperature distribution ahead of the crack tip, a direct comparison with the HRR predicted field, which has  $1/r$  dependence (eq. 9), is shown in Figs. 20 and 21 respectively for the drop tower case and the gas gun case at their corresponding initiation times. In Fig. 20, the squares are the experimentally measured temperature rises at discrete points ahead of the crack tip and the solid line is the HRR prediction with a  $J$  value of  $850\text{ kPa m}$ . The close agreement between the two beyond a finite distance from the crack tip testifies to the existence of the HRR field there. Similarly, Fig. 21 demonstrates the HRR character of the temperature field in the gas gun case also.

It was shown by Narasimhan and Rosakis (1990) that the stress field at the free surface of the specimen, within the plastic zone, follows the plane stress HRR field, which justifies the use of the plane stress fields in eq. (9) above. It was also shown that

the  $J$  integral decreases from the specimen mid-plane towards the free surface. The  $J$  integral estimated from the surface temperature measurements, thus, is the surface  $J$  and thus can not be used as a critical parameter for crack initiation in specimens of finite thickness. However, an increase in the critical surface  $J$  certainly indicates an increase in resistance to fracture. On the other hand, given the relative accuracy and convenience of IR temperature measurement, it would be desirable to develop a way to use such a measurement as a tool to compare the dynamic fracture resistance among different materials as well as to investigate the effect of loading rate on the fracture toughness for a given material. A step in that direction would be a systematic parametric numerical investigation of specimens of finite geometry to relate the surface  $J$  to the thickness averaged  $J$ , which can serve as a better fracture parameter.

## 2.4 Concluding Remarks

This investigation, for the first time, captured the real time evolution of the temperature fields at the crack tips in two steels, a high strength steel and a highly ductile steel. The temperature fields recorded are at the surface of the specimen. Inside the specimen, because of the plane strain constraint, the plastic strains are expected to be lower and hence lower temperatures. The thermal images also provide an opportunity to test models and analyses that predict the temperatures at stationary cracks, the size and the shape of the plastic zone and the plastic work dissipation distribution therein. RL model predicts the crack tip temperature to within the order of magnitude and the

differences can be attributed to the fact that the model was developed for the plane strain situation. No attempt has been made to compare the RL model with temperatures in HY100 steel because there was no independent information about the value of the critical  $J$  integral other than that from temperature measurements. The HRR field, used to extract the  $J$  integral value, predicts a  $1/r$  variation for the temperature rise within the plastic zone. RL model also predicts a  $1/r$  variation and using the HRR based  $J$  in the RL model to predict the temperatures will merely be an exercise in checking the closeness between the hardening (HRR) and non-hardening (RL) models. A remarkable result that comes out of this work is the direct experimental proof of the existence of the HRR stress field near the crack tip even under dynamic loading conditions (Figs. 20 and 21). There have been a limited number of experimental investigations that addressed this issue using optical techniques (Rosakis and Freund, 1982; Zehnder *et al.* 1990, Chiang and Hareesh, 1988). The current investigation provides an alternative temperature based visualization of the HRR field within the plastic zone.

Identifying crack initiation accurately in ductile fracture has always been a grey area in determining their dynamic fracture toughness. If initiation is defined as the first coalescence of voids with the main crack near the mid-plane of the specimen, static fracture toughness can be determined by subjecting several specimens to progressively higher loads and conducting a post-test examination. Since such a procedure is not possible for dynamic testing, a variety of methods have been used in the past to infer the time of crack initiation. They include placing a strain gage close to the specimen and looking for a change in the slope of the signal from the gage, the change in the slope of

the crack opening displacement (Couque, 1994; Guduru *et al.* 1998), magnetic emission detection near the crack tip (Winkler, 1990), constructing the "key curves" (Joyce and Hackett, 1986). This investigation offers a temperature based procedure to identify crack initiation. However, none of the methods have been independently verified by other techniques to check their consistency and repeatability and this is an area that requires further attention.

## References

- Basu, S. and Narasimhan, R. (1999) A finite element study of the effects of material characteristics and crack tip constraint on dynamic ductile fracture initiation. *Journal of the Mechanics and Physics of Solids* 47, 325-350.
- Chiang, F.P. and Hareesh, T.V. (1988) Three-dimensional crack tip deformation: an experimental study and comparison to HRR field. *International Journal of Fracture* 36, 243-257.
- Costin, L.S., Crisman, E.E., Hawley, R.H. and Duffy, J. (1979) On the localization of plastic flow in mild steel tubes under torsional loading. *Proceedings of the 2<sup>nd</sup> Conference on the Mechanical Properties of Materials at High Rates of Strain* (Ed. Harding, J.) The Institute of Physics, London, 90-100.
- Couque, H. (1994) Effect of loading rate on the plane stress fracture toughness properties of an aluminum alloy. *Journal de Physique IV* **C8-4**, 747-752.
- Freund, L.B. (1990) *Dynamic Fracture Mechanics*. Cambridge University Press, Cambridge.
- Guduru, P.R., Singh, R.P., Ravichandran, G. and Rosakis, A.J. (1998) Dynamic crack initiation in ductile steels. *Journal of the Mechanics and Physics of Solids* 46, 1997-2016.

Hartley, K.A., Duffy, J. and Hawley, R.H. (1987) Measurement of the temperature profile during shear band formation in steels deforming at high strain rates. *Journal of the Mechanics and Physics of Solids* 35,283-301.

Hodowany, J., Ravichandran, G., Rosakis, A.J. and Rosakis, P. (2000) Partition of plastic work into heat and stored energy in metals. *Experimental Mechanics* 40, 113-123.

Hutchinson, J.W. (1968) Singular behaviour at the end of a tensile crack in a hardening material. *Journal of the Mechanics and Physics of Solids* 16, 13-31.

Jha, M. and Narasimhan, R. (1992) A finite element analysis of dynamic fracture initiation by ductile failure mechanisms in a 4340 steel. *International Journal of Fracture* 56,209-231.

Joyce, J.A. and Hackett, E.M. (1986) Dynamic J-R curve testing of a high strength steel using the key curve and multispecimen techniques. *Fracture Mechanics: Seventeenth Volume, ASTM STP 905* (Edited by J.H. Underwood, R. Chait, C.W. Smith, D.P. Wilhelm, W.A. Andrews and J.C. Newman). American Society for Testing and Materials, Philadelphia. 741-774.

Kallivayalil, J.A. and Zehnder, A.T. (1994) Measurement of the temperature field induced by dynamic crack growth in beta-C titanium. *International Journal of Fracture* **66**, 99-120.

Kraft, J.M. and Irwin, G.R. (1965) Crack velocity considerations. *Symposium on Fracture Toughness Testing and its Applications*, ASTM STP 381, Philadelphia. 114-129.

Li, Z. and Lambros, 3. (2000) Dynamic thermomechanical behavior of fiber reinforced composites. *Composites, Part A – Applied Science and Manufacturing* **31**, 537-547.

Marchand, A. and Duffy, J. (1988) An experimental study of the formation process of adiabatic shear bands in a structural steel. *Journal of the Mechanics and Physics of Solids* **36**, 251-283.

Mason, J.J. and Rosakis, A.J. (1993) On the dependence of the dynamic crack-tip temperature fields in metals upon crack-tip velocity and material parameters. *Mechanics of Materials* **16**, 337-350.

Moss, G. and Pond Sr, R.B. (1975) Inhomogeneous thermal changes in copper during plastic elongation. *Metallurgical Transactions* **6A**, 1223-1235.

Nakamura, T. and Parks, D.M. (1990) Three-dimensional crack front fields in a thin ductile plate. *Journal of the Mechanics and Physics of Solids* 38, 787-812.

Narasimhan, R. and Rosakis, A.J. (1990) Three-dimensional effects near a crack tip in a ductile three-point bend specimen: part I – A numerical investigation. *Journal of Applied Mechanics* 57,607-617.

Rice, J.R. and Levy, N. (1969) Local heating by plastic deformation at a crack tip. *The Physics of Strength and Plasticity* (Edited by A.S. Argon), MIT press, Cambridge, MA. 277-292.

Rice, J.R. and Rosengren, G.F. (1968) Plane strain deformation near a crack tip in a power-law hardening material. *Journal of the Mechanics and Physics of Solids* 16, 1-13.

Rosakis, A.J. and Freund, L.B. (1982) Optical measurement of the plastic strain concentration at a crack tip in a ductile steel plate. *Journal of Engineering Materials and Technology* 104, 115-125.

Rosakis, P., Rosakis, A.J., Ravichandran, G. and Hodowany, J. (2000) A thermodynamic internal variable model for the partition of plastic work into heat and stored energy in metals. *Journal of the Mechanics and Physics of Solids* 48, 581-607.

Venkert, A., Guduru, P.R. and Ravichandran, G. (2000) An investigation of dynamic failure in 2.3Ni-1.3Cr-0.17C steel. *Metallurgical and Materials Transactions A* **31A**, 1147-1154.

Wilson, M.L., Hawley, R.H. and Duffy, J. (1980) The effect of loading rate and temperature on fracture initiation in 1020 hot rolled steel, *Engineering Fracture Mechanics* **13**, 371-385.

Winkler, S.R. (1990) Magnetic emission detection of crack initiation. *Fracture Mechanics: Twenty-First Symposium, ASTM STP 1074* (Edited by J.P. Gudas, J.A. Joyce and E.M. Hackett), American Society for Testing and Materials, Philadelphia, 178-192.

Zehnder, A.T., Guduru, P.R., Rosakis, A.J. and Ravichandran, G. (2000) Million frames per second infrared imaging system. *Review of Scientific Instruments*. In press.

Zehnder, A.T., Ramamurthy, A.C., Bless, S.J. and Brar, N.S. (1993) Stone impact damage to automotive paint finishes – Measurement of temperature rise due to impact. *International Journal of Impact Engineering* **13**, 133-143.

Zehnder, A.T. and Rosakis, A.J. (1991). On the temperature distribution at the vicinity of dynamically propagating cracks in 4340 steel. *Journal of the Mechanic and Physics of Solids* **39**, 385-415.

Zehnder, A.T. and Rosakis, A.J. (1992) A note on the use of high speed infrared detectors for the measurement of temperature fields at the vicinity of dynamically growing cracks in 4340 steel. *Journal of Applied Mechanics* 59,450-452.

Zhou, M., Ravichandran, G. and Rosakis, A.J. (1996a) Dynamically propagating shear bands in impact-loaded prenotched plates – I. Experimental investigations of temperature signatures and propagation speed. *Journal of the Mechanics and Physics of Solids* 44, 981-1006.

Zhou, M., Ravichandran, G. and Rosakis, A.J. (1996b) Dynamically propagating shear bands in impact-loaded prenotched plates – II. Numerical simulations. *Journal of the Mechanics and Physics of Solids* 44, 1007-1032.

Zhuang, S. and Ravichandran, G. (1998) SM Report No. 98-4, Graduate Aeronautical Laboratories, California Institute of Technology, Pasadena, CA.

## List of Tables

Table 1. Chemical composition (wt %) of C300 maraging steel

Table 2. Chemical composition (wt %) of HY100 maraging steel

## List of Figures

- Figure 1      Block diagram for the IR imaging system.
- Figure 2      Ray diagram for the double Schwarzschild focussing system.
- Figure 3      A photograph of the IR imaging system.
- Figure 4      Calibration curve obtained by repeatedly heating the sample to 225°C.
- Figure 5      Calibration curves obtained by heating the sample to 525°C and 225°C.
- Figure 6      Ratio of the two calibration curves shown in Fig. 5.  $\Delta V_{HT}$  is the output from the 525°C test and  $\Delta V_{LT}$  is the output from the 225°C test.
- Figure 7      A schematic illustration of the specimen geometry and loading arrangement for C300 specimens. All dimensions shown are in millimeters.
- Figure 8      A photograph of the experimental setup for testing C300 specimens under a drop weight tower.
- Figure 9      A schematic illustration of the specimen geometry and loading arrangement for HY100 specimens. All dimensions shown are in millimeters.
- Figure 10     A schematic illustration of the experimental setup for testing

HY100 specimens with a gas gun and measure the crack tip temperature field.

- Figure 11 A sequence of thermal images showing the development of the plastic zone until initiation.
- Figure 12 A sequence of images showing the development of the temperature field for a just initiated crack.
- Figure 13 (a) A thermal image of crack tip region in C300 at initiation. (b) The plastic zone with the contours of equivalent stress and the corresponding temperature rise for a 4340 steel, from the numerical simulations of Narasimhan and Rosakis (1990).
- Figure 14 A sequence of images showing the evolution of the temperature field at the crack tip in a HY100 specimen subjected to drop weight impact at 4 m/s.
- Figure 15 (a) Schematic illustration of the area of temperature measurement and the position of the crack tip. The digits represent the detectors focussed along the crack line. (b) Temperature signals from the detectors on the crack line.
- Figure 16 A sequence of images showing the evolution of the temperature field at the crack tip in a HY100 specimen subjected to gas gun impact at 50 m/s.
- Figure 17 (a) Schematic illustration of the area of temperature measurement and the position of the crack tip. The digits represent the detectors focussed along the crack line. (b) Temperature signals from the

detectors on the crack line.

Figure 18 Evolution of the **J** integral as a function of time, as calculated from the temperature signals along the crack line for the drop weight tower impact.

Figure 19 Evolution of the **J** integral as a function of time, as calculated from the temperature signals along the crack line for the gas gun impact.

Figure 20 An illustration of the  $1/r$  character of the temperature distribution in the drop weight tower experiment.

---

Figure 21 An illustration of the  $1/r$  character of the temperature distribution in the gas gun experiment.

Ni	Co	Mo	Ti	Si	Al	Cr	Cu
18.9	9.2	4.88	0.7	0.07	0.11	0.18	0.14

Table 1

C	Mn	Cu	Si	Ni	Cr	Sn	Mo
0.17	0.3	0.13	0.22	2.35	1.32	0.013	0.25

Table 2

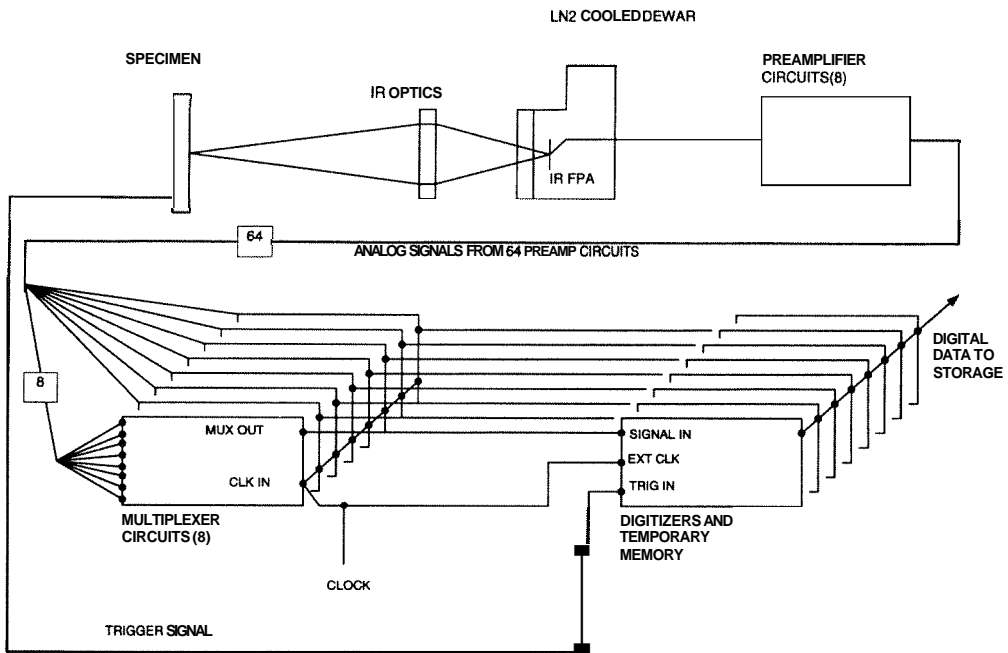


Figure 1

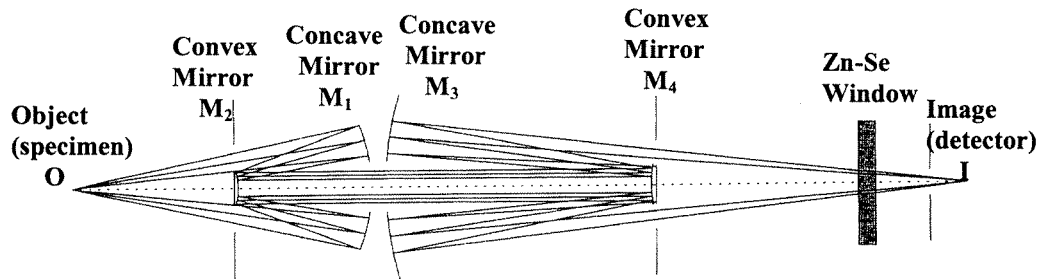


Figure 2

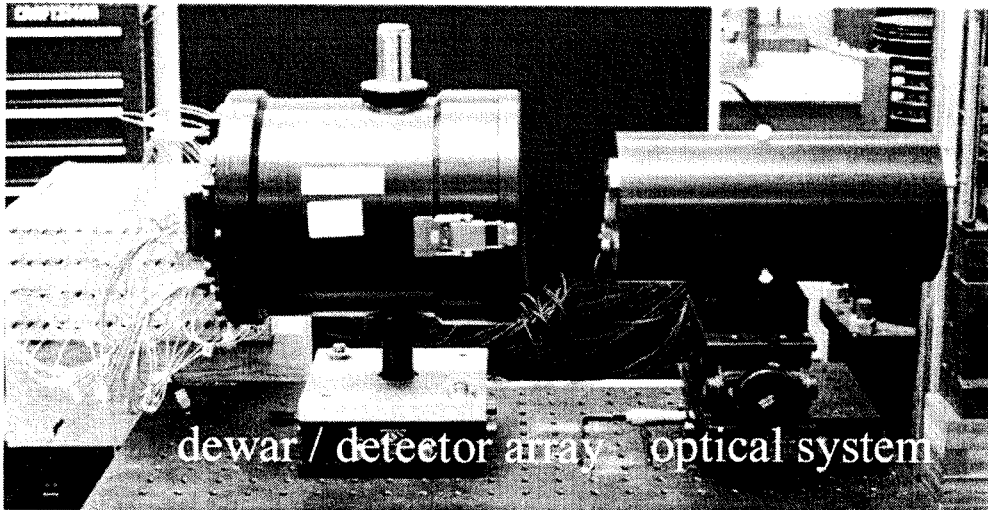


Figure 3

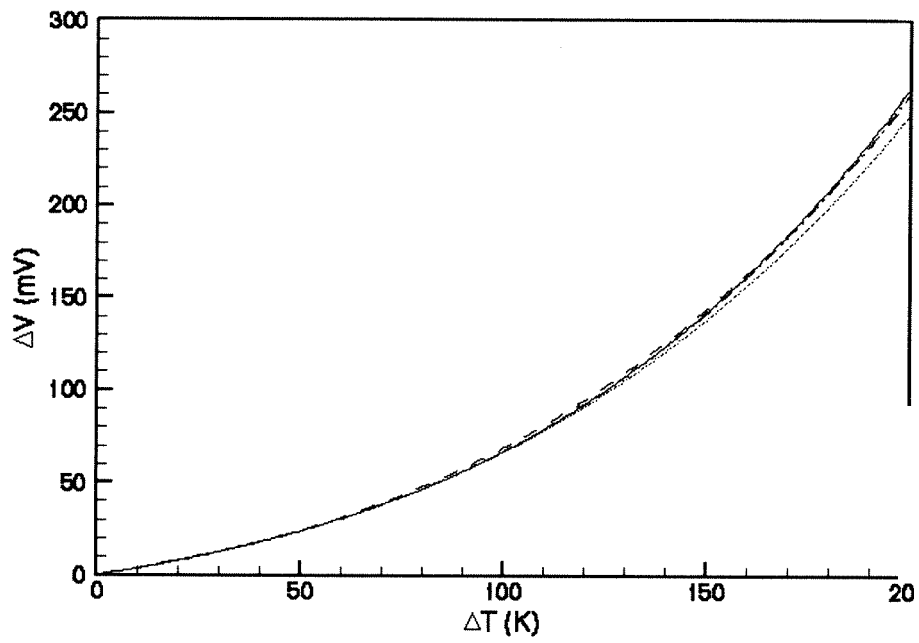


Figure 4

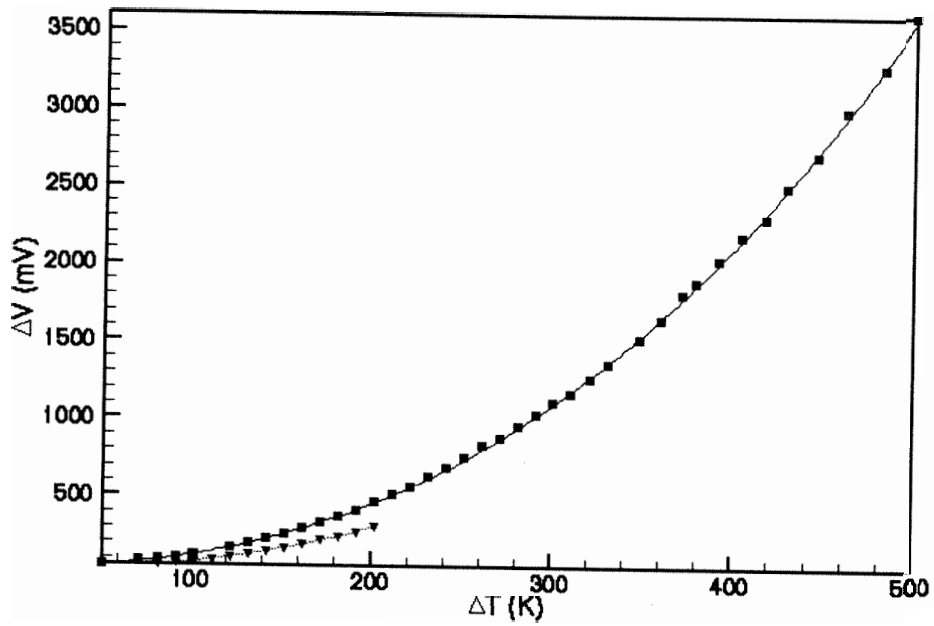


Figure 5

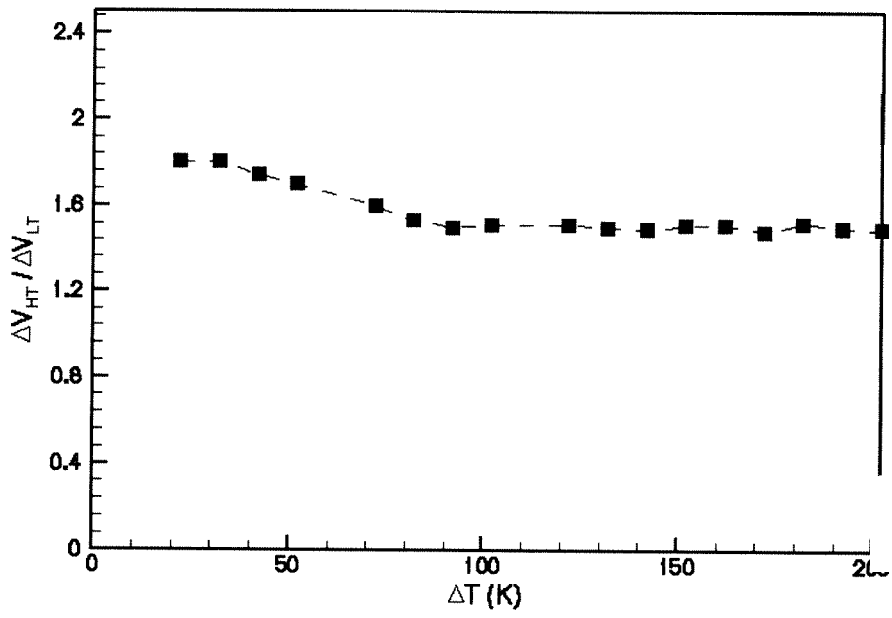


Figure 6

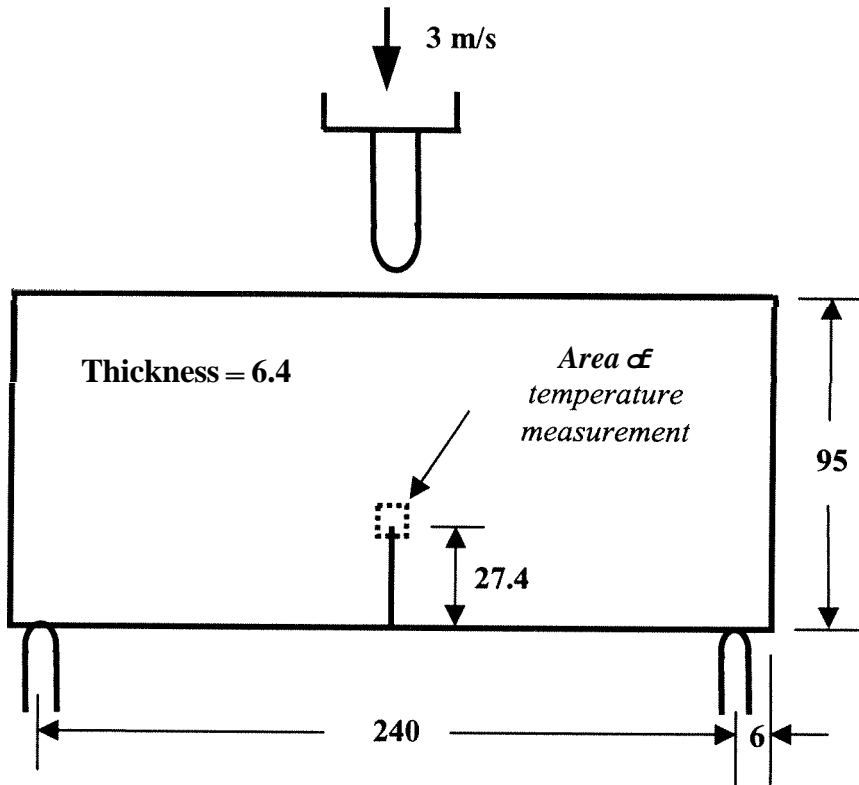


Figure 7

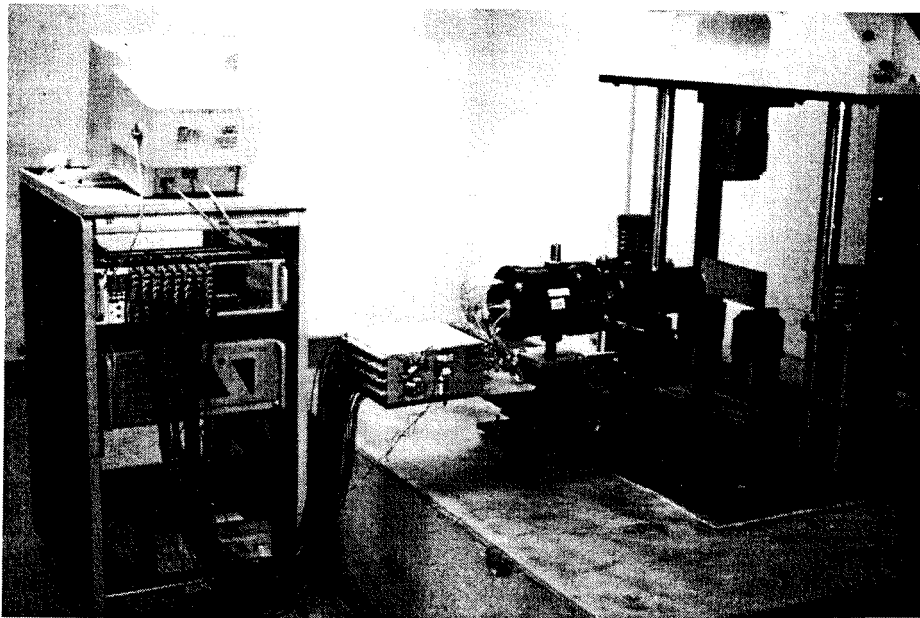


Figure 8

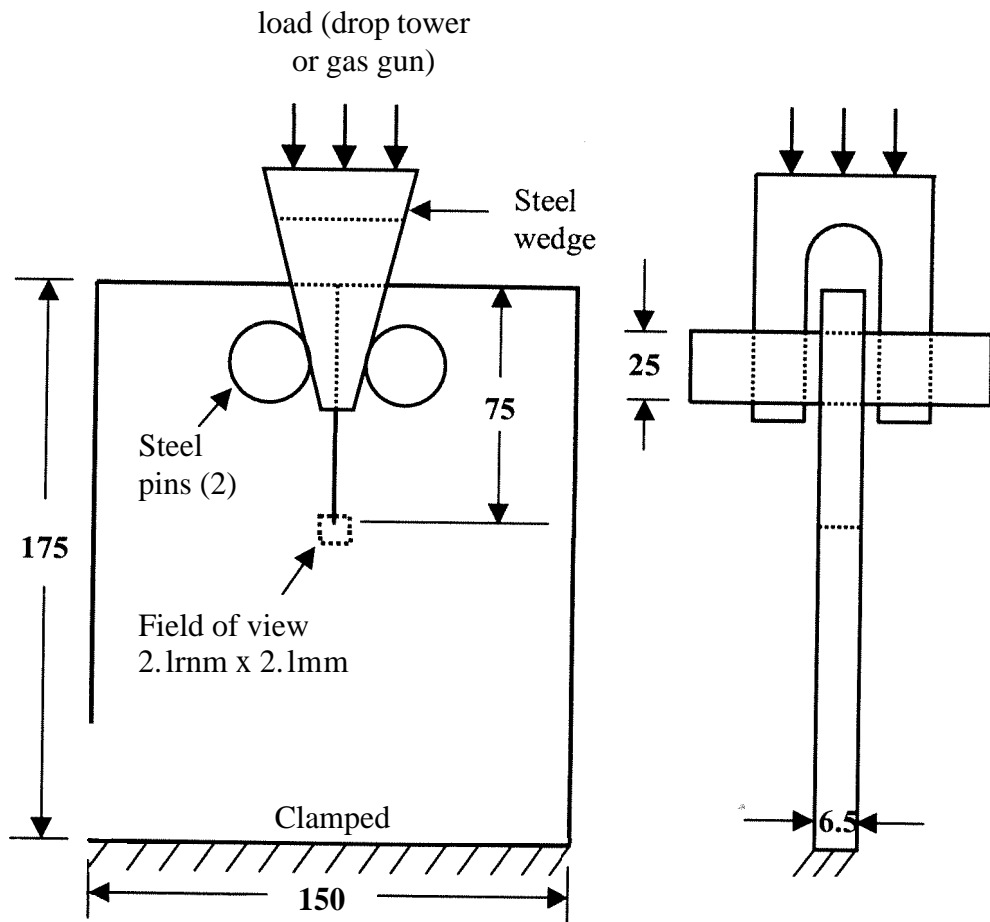


Figure 9

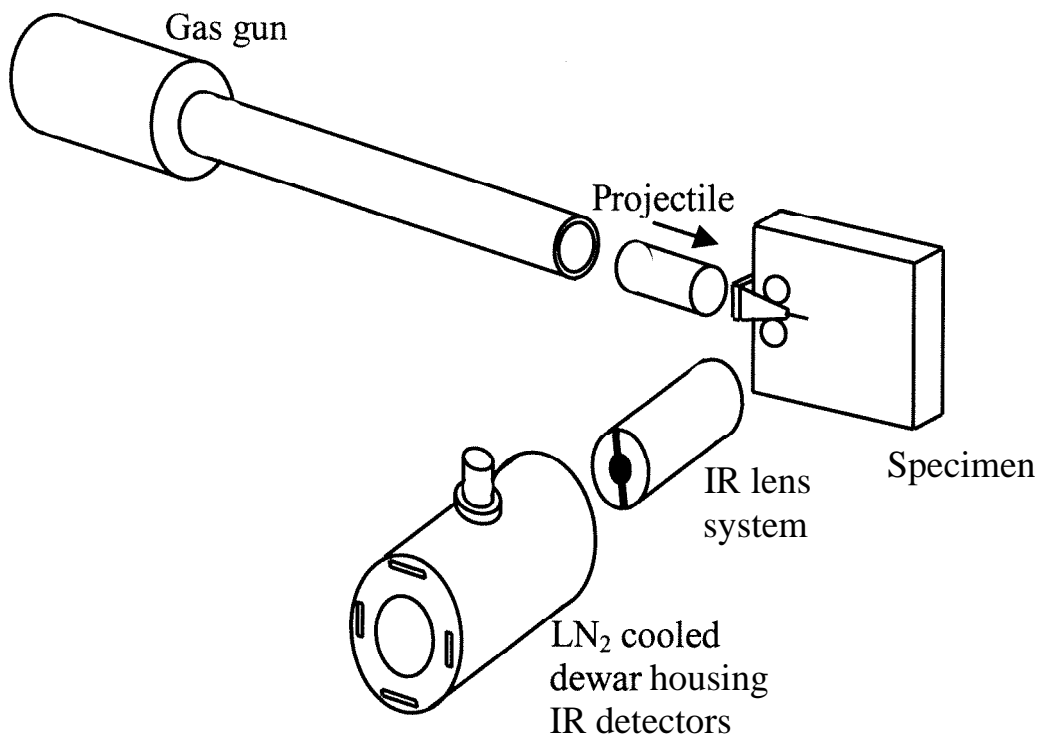


Figure 10

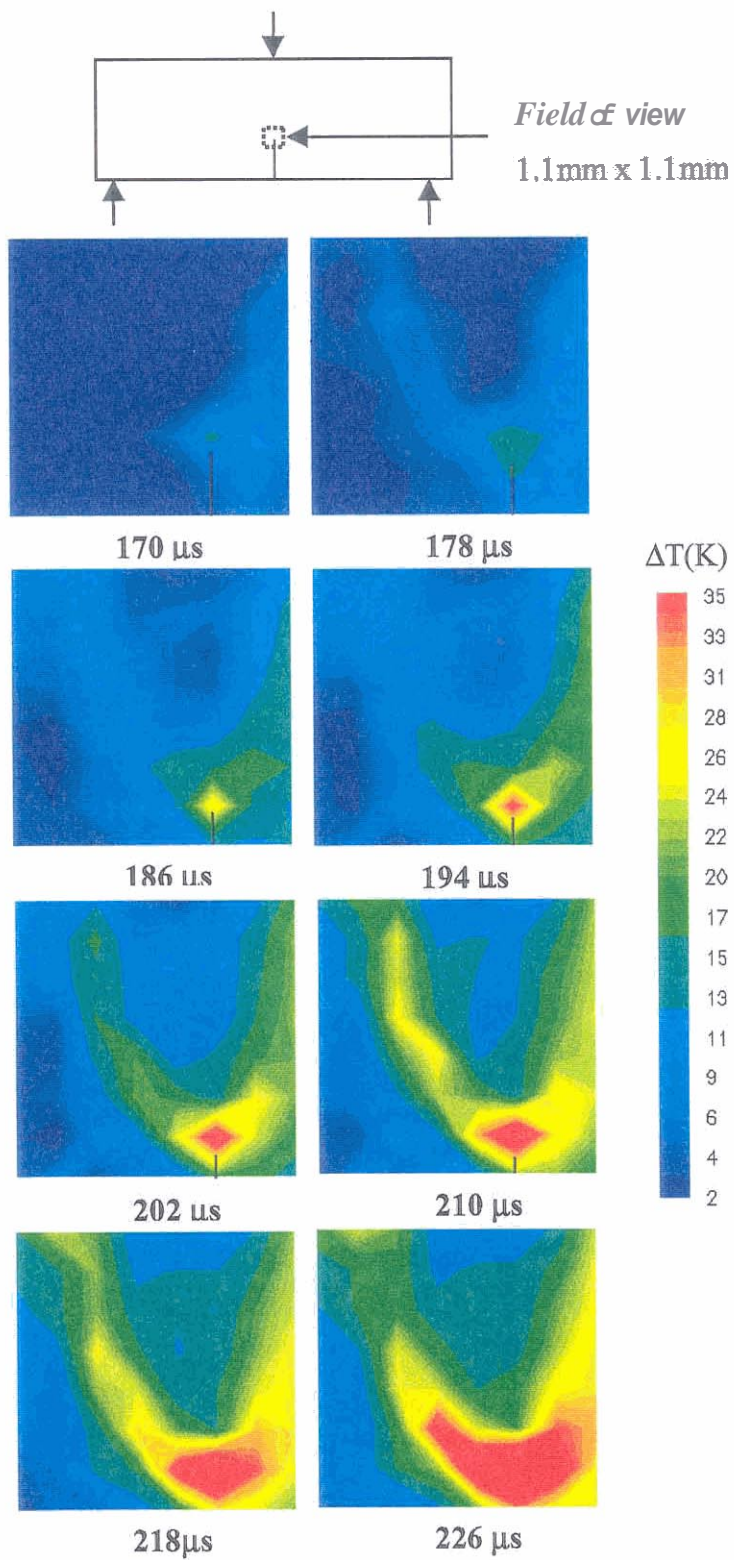


Figure 11

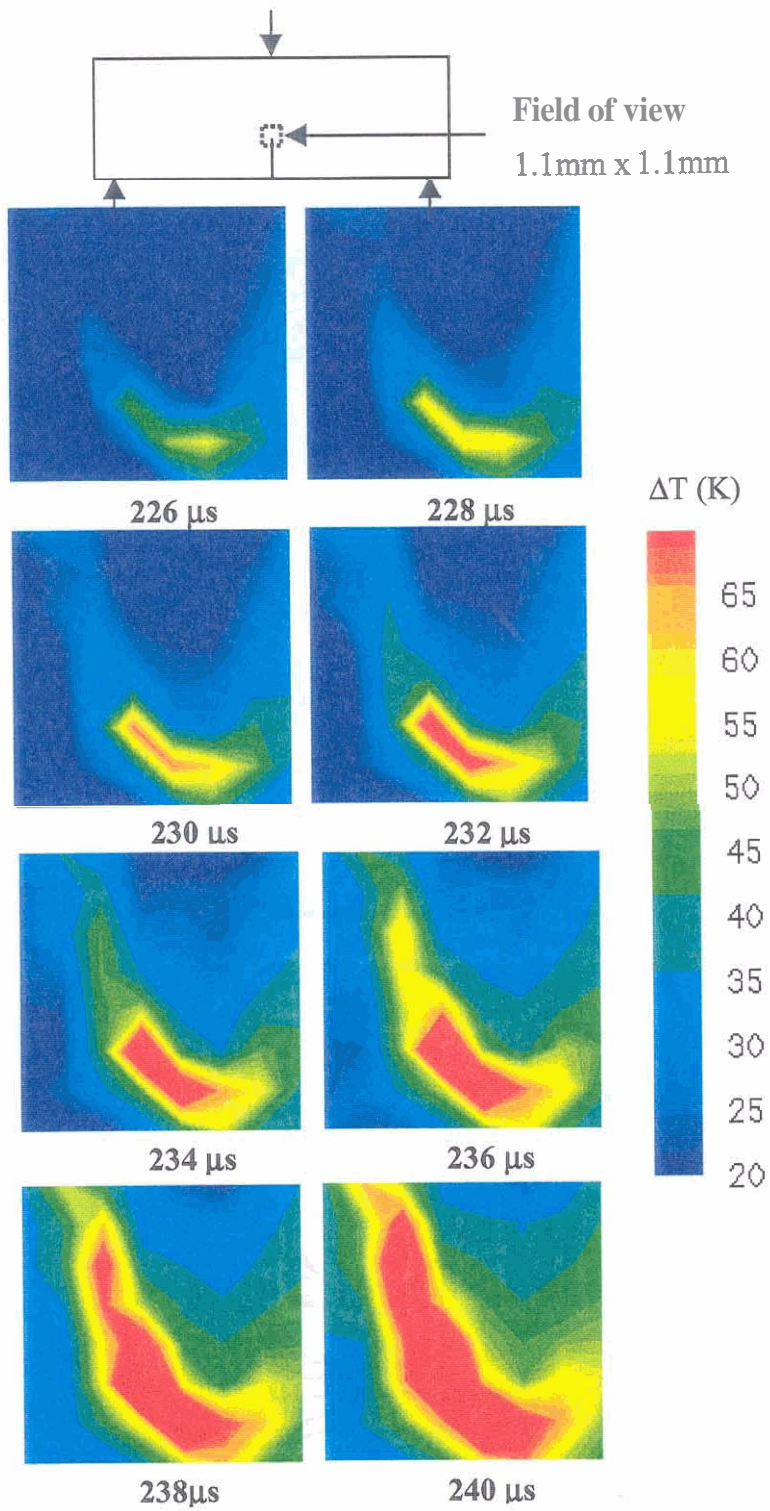
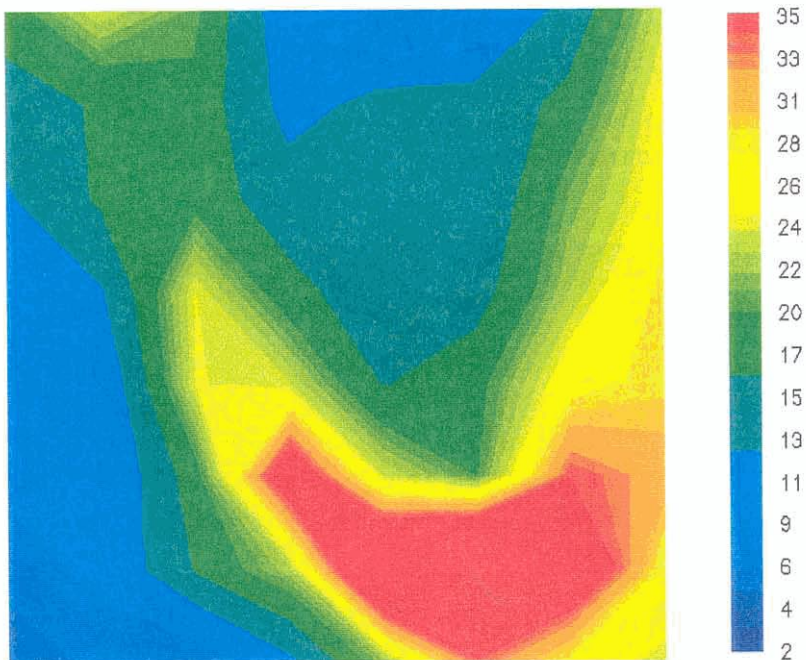


Figure 12



1.1 mm x 1.1 mm

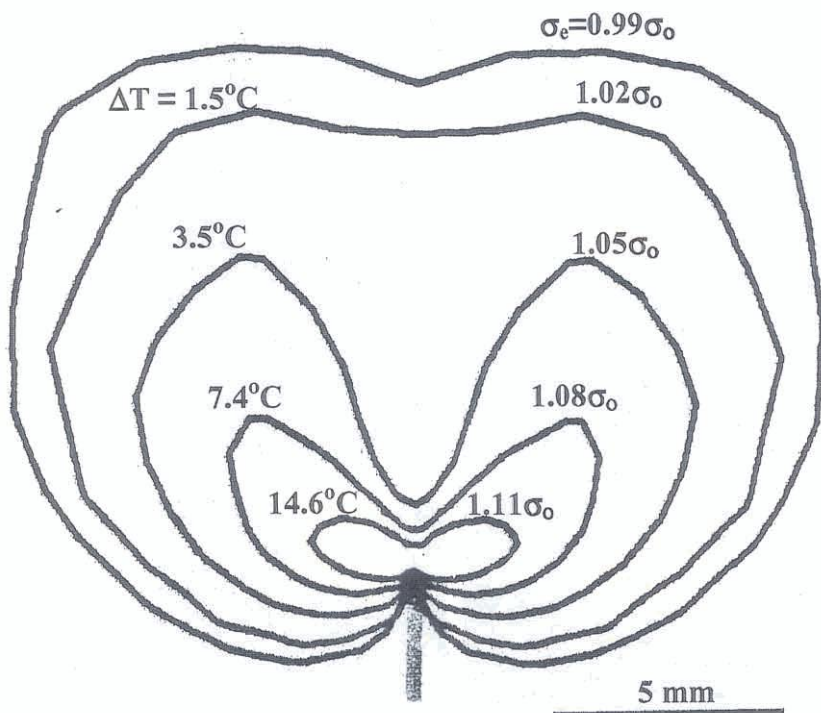


Figure 13

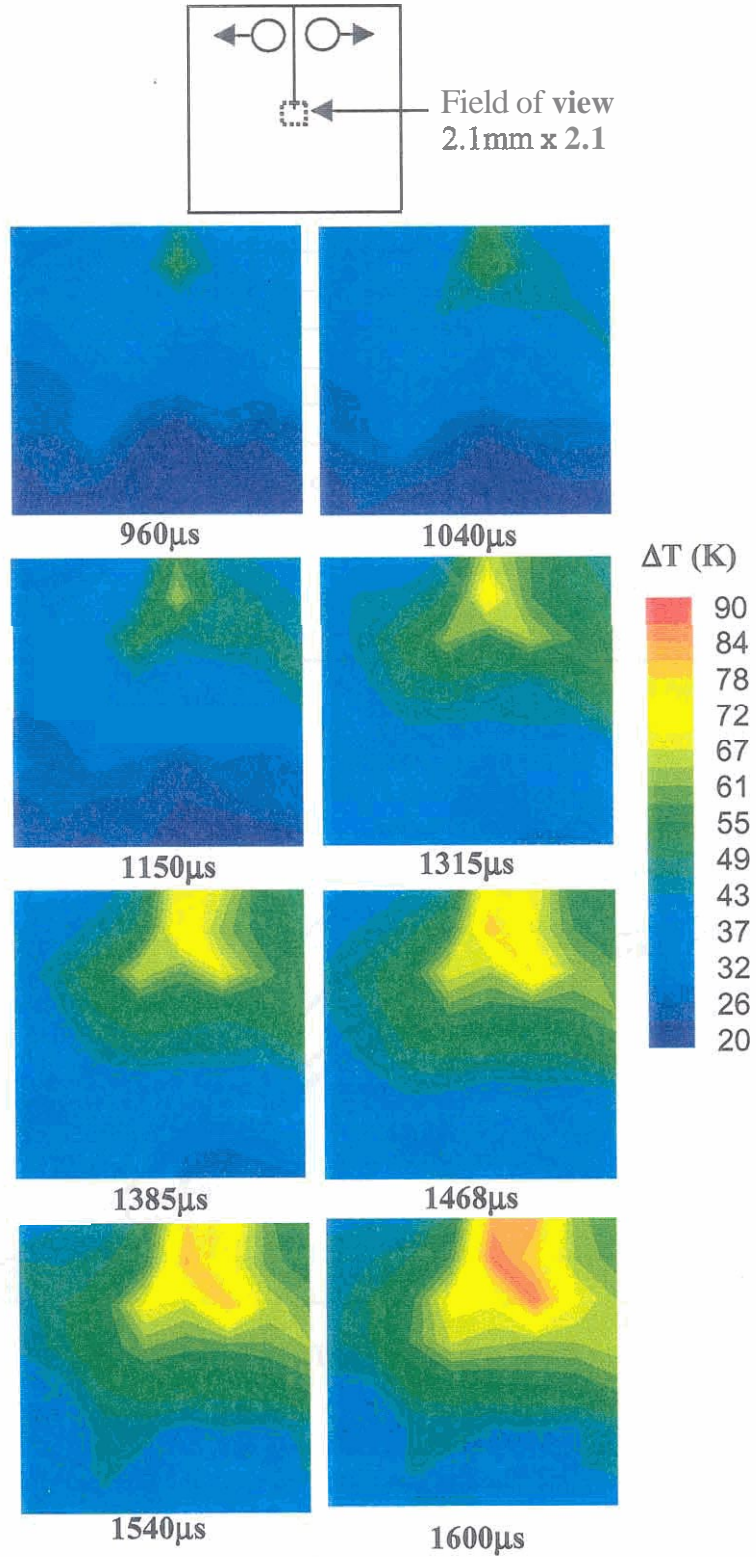
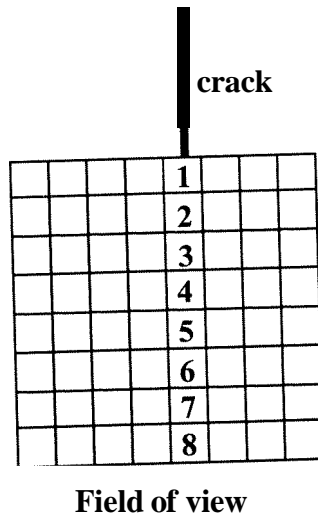
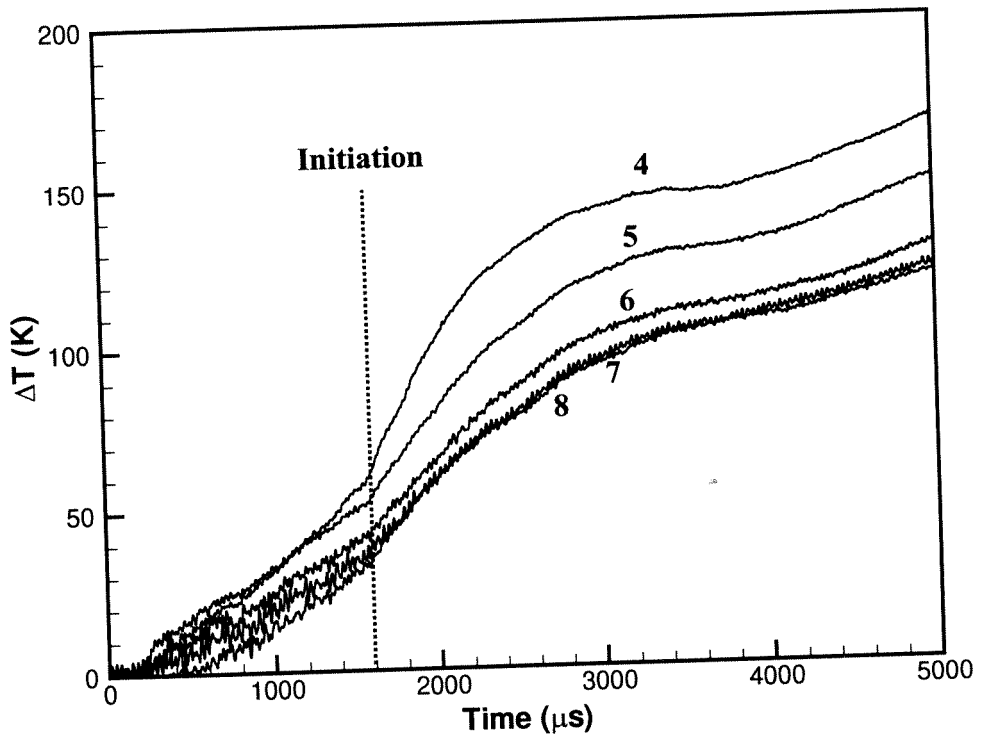


Figure 14



(a)



(b)

Figure 15

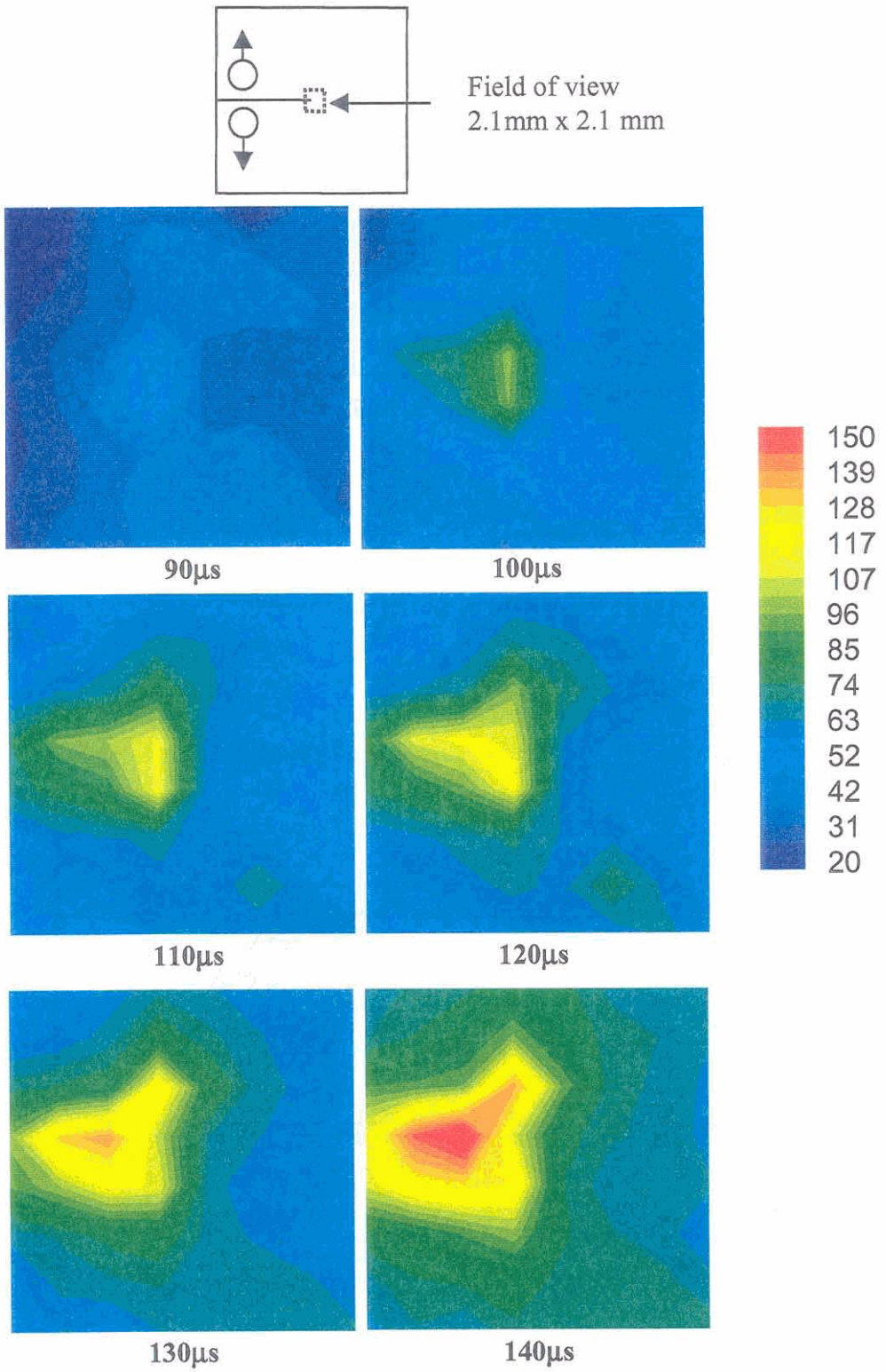
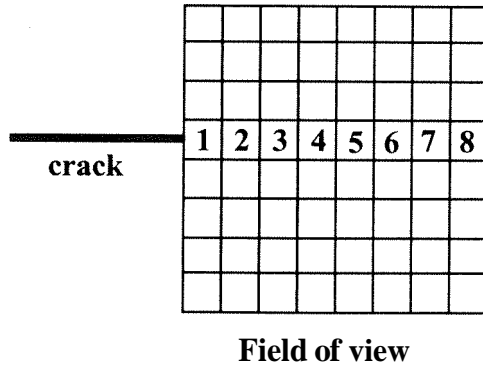


Figure 16



(a)

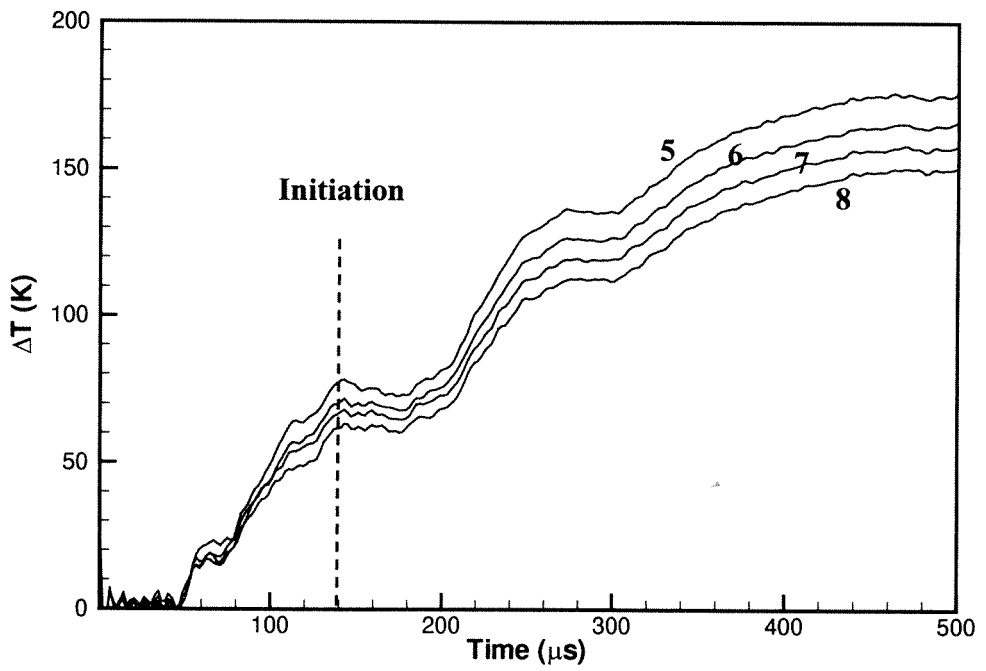
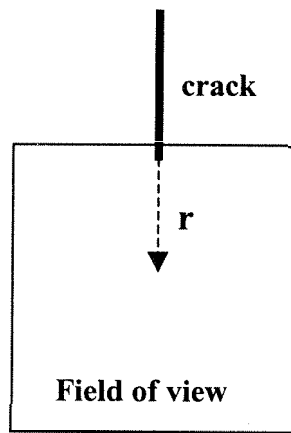
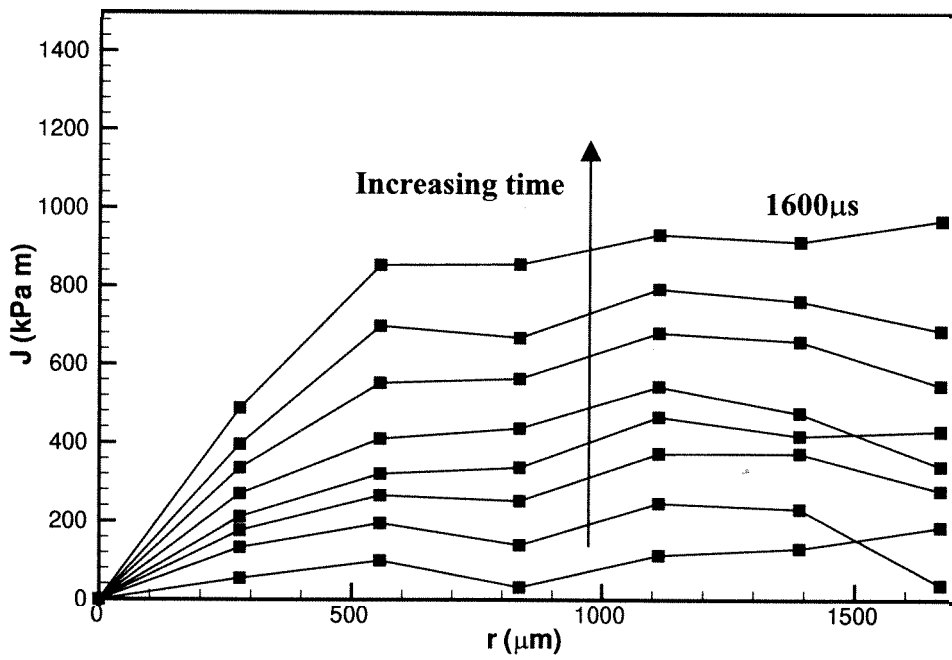


Figure 17

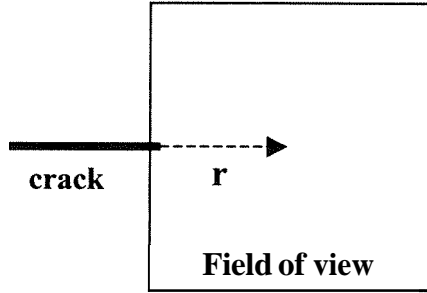


(a)

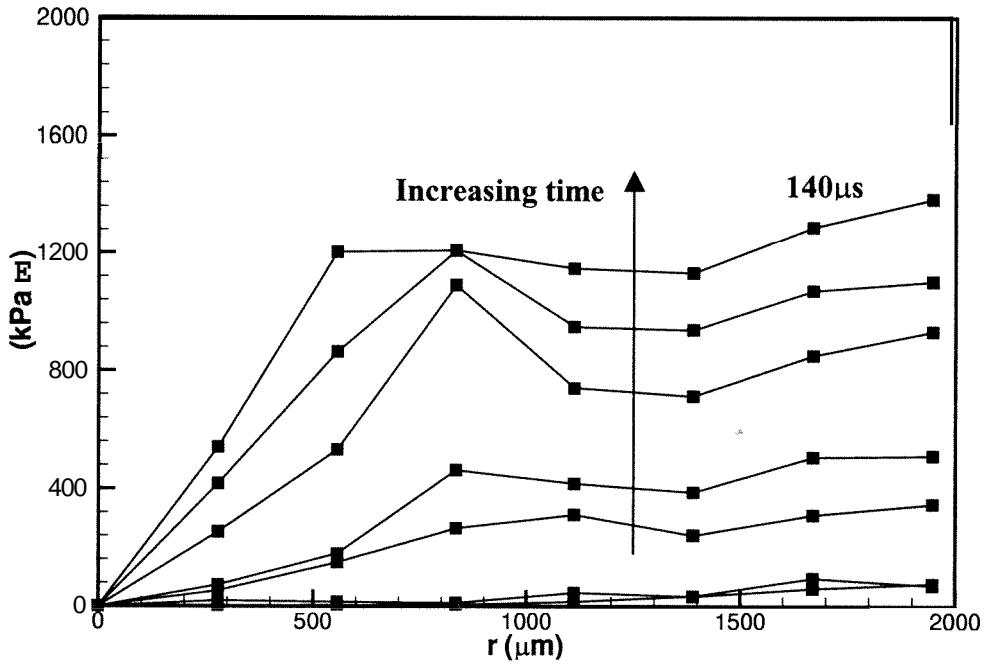


(b)

Figure 18



(a)



(b)

Figure 19

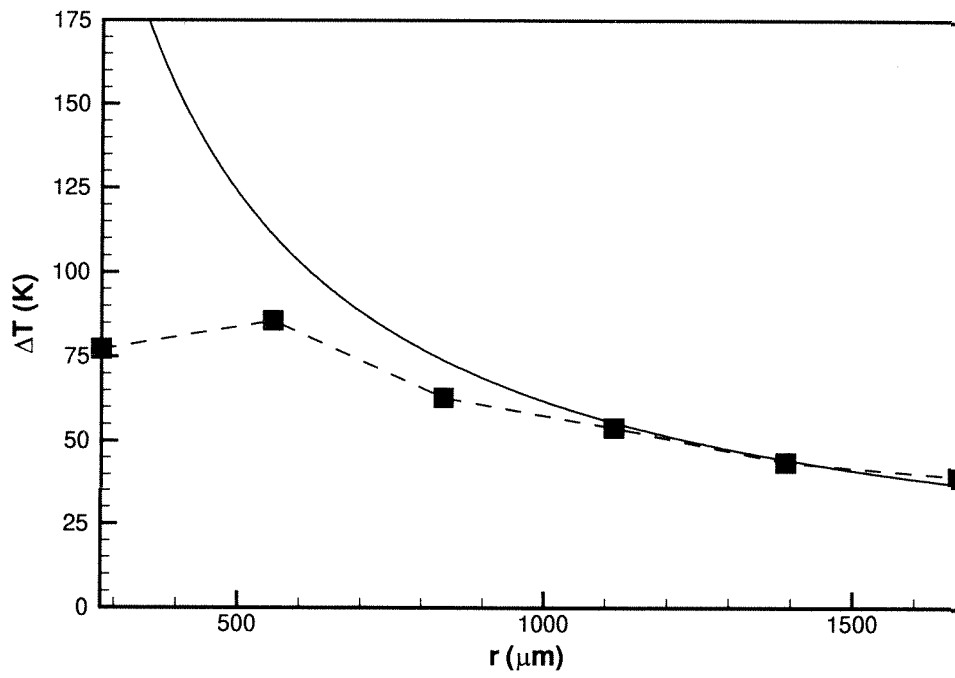


Figure 20

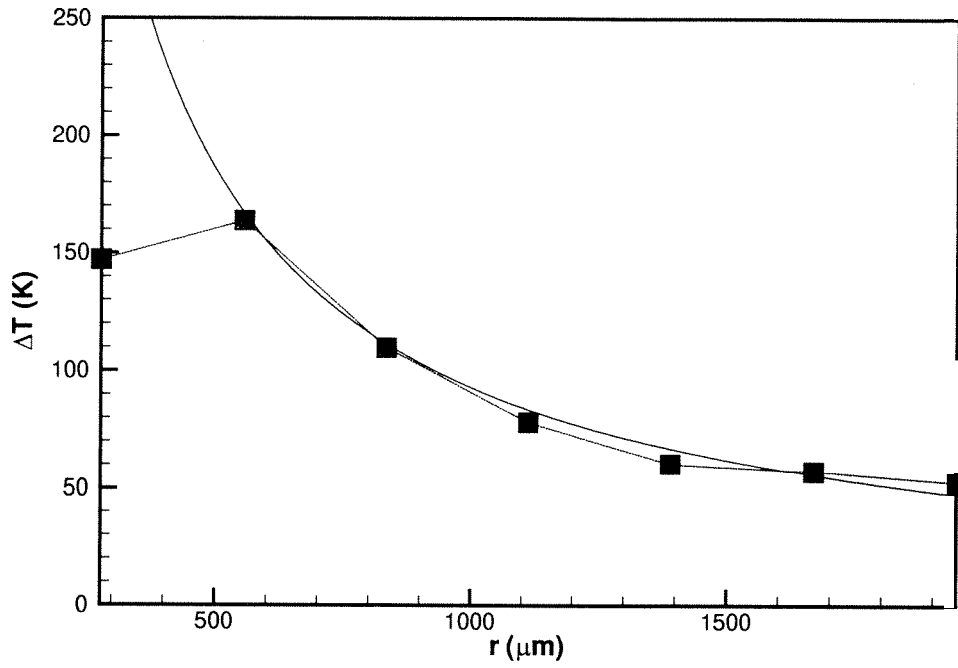


Figure 21

## Chapter 3

# Dynamic Shear Bands: An Investigation Using High Speed Optical and Infrared Diagnostics

### Abstract

This paper presents an experimental investigation of the initiation and propagation characteristics of dynamic shear bands in C300 maraging steel. Pre-fatigued single edge notched specimens were impacted on the edge under the notch to produce shear dominated mixed mode stress fields. The optical technique of coherent gradient sensing (CGS) was employed to study the evolution of the mixed mode stress intensity factors. Simultaneously, a newly developed 2-D high speed infrared (IR) camera was employed to obtain the temperature field evolution during the initiation and propagation of the shear bands. The possible criteria for observed failure mode selection are discussed. The IR images, for the first time, revealed the transition of crack tip plastic zone in to a shear band and also captured the structure of the tip of a propagating shear band. These thermographs support the notion of a diffuse shear band tip and reveal "hot spots" distributed along the length of a well developed shear band.

### 3.1 Introduction

Ever since Zener and Hollomon (1944) explained the physics of the formation of dynamic shear bands in solids, considerable research effort has been devoted to predict their initiation and to model their structure after they are formed. The generally accepted explanation for their formation is as follows. When solids experience dynamic plastic deformation, most of the external work done is dissipated as heat, which raises the local temperature of the material. When a slightly inhomogeneous plastic deformation occurs in **an** otherwise uniformly deforming material due to the presence of a geometric discontinuity or a material inhomogeneity, and if the deformation is rapid enough to supersede heat conduction effects, local temperature is elevated at those locations of inhomogeneities. This increase in temperature softens the material locally and reduces its resistance to further plastic deformation, i.e., local yield stress is lowered. As a result, plastic deformation becomes more inhomogeneous, leading to a self sustaining cycle of instability: inhomogeneous shear plastic flow - nonuniform temperature distribution - local thermal softening - further inhomogeneous shear plastic flow. The result is the formation of a highly localized shear band, starting from a small nonuniformity of deformation. Thus, the existing inhomogeneities in a structure play a crucial role in precipitating shear bands under dynamic shear loading. Kalthoff and Winkler (1988), in their pioneering experiments, demonstrated that a preexisting notch or a crack can act as **an** ideal geometric discontinuity in a material to initiate a shear band, when subjected to dynamic shear dominated loading. These experiments are significant because they

introduced a new failure mode and a failure mode transition into the framework of dynamic fracture mechanics. In addition, stress and strain fields at a crack tip are analytically well characterized quantities within the framework of fracture mechanics and the shear band initiation conditions could potentially be described in terms of the well known fracture mechanics parameters. These experiments initiated numerous efforts to understand the failure behavior of cracks subjected to shear dominated loading and introduced the notion of failure mode transition.

In their experiments, Kalthoff and Winkler (1988) impacted double edge notched specimens of maraging steel with a steel projectile between the two notches, thus generating a shear dominated mixed mode condition at the crack tip. When the impact speed was below a critical value, they observed that cracks initiated in opening mode at an angle of  $70^\circ$  to the crack line. Such a failure mode conforms to the predictions of the well known mixed mode crack initiation criteria such as the maximum energy release rate criterion and the maximum tensile hoop stress criterion. As the impact speed was increased, a failure mode transition was observed. At high impact speeds, a shear band initiated and propagated from the crack tip. Further, as the crack tip radius was decreased, the critical impact speed required for this transition was also lowered. When the radius was almost zero, i.e., the notch became a fatigue crack tip, within the impact speed range of 20 to 53 m/s, no opening mode cracks were reported; only shear bands of various lengths were observed. Although they reported a novel failure mode transition for the first time, certain important experimental details, which could help in understanding the mechanics of the failure transition process, were not reported in their work. They include

the times of failure initiation in each experiment, and the history of stress intensity factors  $K_I$  and  $K_{II}$  as a function of time up to initiation (except for two impact speeds, 13m/s and 33m/s). Also, in the experiments reported, the angle at which the opening cracks initiated varied from  $50^\circ$  to  $70^\circ$ . Knowledge of the evolution of mode mixity up to crack initiation would provide useful insights into the dynamic mixed mode initiation mechanics. These issues necessitate a detailed experimental investigation in which the stress field at the crack tip is measured continuously up to crack initiation in order to quantify the parameters that govern the competition between the two failure modes, i.e., opening crack and shear band.

Motivated by these experiments, Lee and Freund (1990) carried out theoretical and numerical investigation of the evolution of the mixed mode stress field in a single edge notched specimen, impacted under the notch. Reasonable agreement was found between the predictions of the theoretical analysis and the experimental results reported by Kalthoff and Winkler (1988). The theoretical analysis of Lee and Freund (1990) is valid only until the time when waves reach the crack tip carrying information about the existence of free boundaries and the finite diameter of the projectile. They also performed a numerical analysis of a specimen with a finite geometry. Mason *et al.* (1992) made an accurate measurement of mixed mode stress intensity factors, evolving as a function of time, in edge notched PMMA specimens, using the optical technique of coherent gradient sensing in transmission and high speed photography. They made a detailed comparison between their results and the theoretical and numerical results of Lee and Freund (1990). Good agreement between the three was found at short times. At longer times, the

numerical results which accounted for the finite geometry were found to be in better agreement with the experiments than the theoretical results. However, the issue of failure mode transition was not addressed in their investigation.

A detailed study, using a similar specimen geometry and loading arrangement, was conducted by Ravi-Chandar (1995), who tested specimens made of polycarbonate. Dynamic photoelasticity in conjunction with high speed photography was employed to monitor the evolving stress field around the crack tip. A number of revealing observations were made, which also clarified the findings of Kalthoff and Winkler (1988). It was observed that, when the impact speed was less than 28 m/s, no crack initiated. When the impact speed was between 28 and 32 m/s, an opening crack initiated at an angle of 22° to the crack line after several wave reflections within the specimen. As the impact speed was increased beyond 32 m/s and up to 55 m/s, an opening mode I crack initiated at 68° to the crack line before any reflected waves from the boundaries arrived at the crack tip. This matches very well with the predicted angle of 63° from the analysis of Lee and Freund (1990). Beyond 55 m/s, a shear band initiated and propagated from the crack tip, demonstrating the failure mode transition observed by Kalthoff and Winkler (1988). In addition, Ravi-Chandar *et al.* (2000) numerically investigated the development of the stress field at the crack tip in order to understand the effect of the impact speed on the mechanics of the failure mode transition. They found that at high impact speeds, formation of a plastic zone in front of the crack tip suppresses the development of high tensile hoop stress at the crack tip which is necessary for a mode I crack to initiate. Thus the impact geometry and the plasticity of the specimen conspire to delay the opening

crack failure mode and provide an opportunity for the plastic zone to develop into a shear band. However, the investigations of Ravi-Chandar (1995) and Ravi-Chandar *et al.* (2000) could not provide the detailed evolution of stress intensity factors because the photoelasticity fringes failed to show any K-dominance. Similar observations of failure mode transition in polymers were also reported by Rittel and Levin (1998). The failure mode transition phenomenon has also been numerically analyzed by Needleman and Tvergaard (1995), who modeled the Kalthoff specimen made of a material, whose response was characterized by an elastic-viscoplastic constitutive relation of a porous plastic solid (Gurson model), with adiabatic heating due to plastic dissipation and the resulting thermal softening accounted for. Similar to the findings of Ravi-Chandar (2000), they too noticed that at higher impact speeds, a softening region developing ahead of the crack tip shields the lateral regions from developing high tensile stresses, suppressing the formation of opening cracks.

The above numerical investigations attempted to provide a "mechanism" based explanation for the failure mode transition. They do not provide a criterion to predict failure mode selection. There have been attempts in that direction by formulating criteria in terms of the well known fracture mechanics parameters such as a critical combination of mode I and mode II stress intensity factors. Zhou *et al.* (1996b) proposed that a shear band initiates when the  $J$  integral reaches a critical value. Chen and Batra (1998a-c) proposed that, under adiabatic conditions, a shear band would initiate at a notch or a crack tip when the effective plastic strain at a prescribed distance from the crack tip reaches a critical value. This would translate into a shear band initiation locus on the  $K_I -$

$K_{II}$  plane for a given mixed mode situation, when the loading is rapid enough to render heat conduction effects negligible. Very limited experimental data is available to test such a hypothesis. The issue is complicated further by another locus on the  $K_I$ - $K_{II}$  plane which represents failure by opening mode in the form of a kinked crack. Roessig and Mason (1998) examined the shear band initiation behavior of a variety of steels by impacting single edge notched specimens supported against steel dies. They measured shear band initiation times from the experiments. Then, by numerically simulating the experiment, they estimated the critical stress intensity factors at initiation. They found that critical  $K_{II}$  can potentially be used to predict the onset of shear bands, though some dependence on impact speed and thus rate was observed.

All of the contributions discussed above are concerned with the behavior of a notch or a crack tip when subjected to a predominantly mode II loading in the single/double edge notched geometry subjected to asymmetric projectile impact and the competition between the competing failure mechanisms. However, it should be noted that though the study of the critical conditions for the initiation of a shear band from the tip of a crack subjected to a dynamic mixed mode loading is of special interest within the framework of dynamic fracture mechanics, it is only a particular aspect of the general problem of initiation of adiabatic shear localization at inhomogeneities or asperities in materials. The question of critical conditions for initiating shear localization in a homogeneously deforming material has received a great deal of attention and there are many excellent references devoted to this topic (Recht, 1964; Rogers, 1979; Clifton, 1980; Bai, 1982; Clifton et al., 1984; Molinari and Clifton, 1987; Shawki and Clifton, 1989; Bai and Dodd, 1992). The study

of propagating shear bands is a fascinating subject that has attracted wide attention in the past. From an experimental point of view, the relevant measurable quantities of interest for an advancing shear band are the speed of propagation, its width and the temperature rise along and across the band. Very few detailed investigations have been conducted in the past due to many intractable experimental difficulties associated with such measurements. These difficulties include extremely short duration of the event; typically shear bands initiate and propagate across the region of interest in just a few microseconds, requiring highly repeatable experimental geometries, a measurement device with sub-microsecond response time and very high speed data acquisition systems. Further, shear bands are typically very narrow, often less than 100  $\mu\text{m}$  in width, necessitating measuring devices with extremely high spatial resolution capabilities. In addition, making accurate high speed temperature measurements limits the choice of techniques to infrared (IR) thermography. One of the first attempts to measure the temperature in a shear band using an infrared thermographic technique was made by Costin *et al.* (1979). They subjected thin walled cylindrical specimens to dynamic twisting in a Kolsky torsional bar. Using a single element IR detector, they measured the average temperature over a spot 1mm in size, that contained a propagating shear band in a low carbon steel and estimated the temperature rise to be about 100°C. Since the spot size was much larger than the width of the shear band, their estimate was a lower bound for the actual temperature rise within the shear band. A more refined investigation, using a linear array of ten Indium Antimonide (InSb) IR detectors, was conducted by Hartley *et al.* (1987), for measuring the temperature rise in a shear band in two low carbon steels. The specimens and loading device were the same as those used by Costin *et al.* (1979).

The detectors measured temperature at 10 discrete points along a line across the projected path of the shear band, as it passed by. They observed that the shear bands in these materials were typically 150-250  $\mu\text{m}$  wide and the maximum temperature rise they measured, using a spot size of 20  $\mu\text{m}$ , was about 450°C. Subsequently, Marchand and Duffy (1988) used a linear array of twelve InSb detectors to measure temperature rise in shear bands in thin walled cylindrical specimens made of HY100 steel. The width of the shear bands in HY100 was typically 10-20  $\mu\text{m}$ . A spot size of 35  $\mu\text{m}$  was used and a maximum temperature rise of about 600°C was reported. Since the spot size was almost twice as wide as the shear band, the measurements were essentially lower bound estimates for the maximum temperature within the band. One disadvantage of using InSb detectors, especially along with small spot sizes, is their low signal to noise ratio. In the above investigations, for example, the temperature resolution was rather low, with the smallest detectable temperature rise being 80°C. Though these experiments were the first comprehensive investigations of the characteristics of adiabatic shear bands, they were limited by the linear arrays of detectors employed. A shear band is essentially a two-dimensional entity with a moving tip and an evolving structure behind it and a linear array of detectors can yield only partial information. Using high speed photography, Marchand and Duffy (1988) estimated the speed of the shear band propagation to be around 250-500m/s. The measurement of the shear band speed was handicapped by the fact that the shear bands initiated at several locations around the circumference of the specimen and propagated independently to meet each other. A systematic study to investigate the speed of shear bands and the associated temperature rise was undertaken by Zhou *et al.* (1996a,b) on the single edge notched geometry, with specimens made of a

maraging steel, C300. Since they studied shear bands initiating at a notch tip, using a high speed camera, they could clearly image a single propagating shear band and reported propagation speeds up to 1000 m/s. In addition, they also employed a linear array of 16 InSb IR detectors to measure the temperature rise across the shear band. This was the first investigation to measure the shear band speeds accurately and relate them to the impact speeds and to report very high temperatures, close to the melting temperature of the material. These measurements were made over a spot size of 100 $\mu$ m and thus were limited in spatial resolution. They also observed, for the first time, that for certain impact speeds, a shear band initiates, propagates, arrests within the specimen and a mode I crack initiates from the tip of the arrested shear band at an angle of about 35° to the shear band direction. Finally they conducted a detailed numerical investigation to simulate the shear band speeds and the failure mode transition. However, the temperatures observed in the experiments were much higher than the computed values.

Analytically, propagating shear bands were investigated, among others, by Wu and Freund (1984), Freund *et al.*, (1985) Wright (1987, 1995), Wright and Ockendon (1992), Wright and Ravichandran (1997) and Grady (1992, 1994). Wu and Freund (1984) sought to investigate the mechanism of shear band formation through the concept of "wave trapping." They considered the problem of a half space whose boundary was subjected to constant shearing velocity. They then analyzed the process by which the information about the boundary conditions is transmitted into the half space and demonstrated how very large strains are accumulated in a thin layer close to the boundary, leading to the formation of a shear band. In order to study the propagation behavior of a shear band,

Freund *et al.* considered a block of material with a defect and numerically subjected it to anti-plane shear deformation. A shear band initiated at the defect and propagated at a speed of  $0.57C_S$ , where  $C_S$  is the shear wave speed of the material. This estimate is higher than the experimentally observed shear band speeds and further experiments are necessary to investigate if shear bands can be driven at higher speeds. Wright and his coworkers, in a series of pioneering articles (Wright, 1987, 1995; Wright and Ockendon, 1992; Wright and Ravichandran, 1997), attempted to model the canonical structure of a well developed shear band. They developed a theory to describe the structure of temperature, shear strain and strain rate across the shear band. Lack of experimental data regarding temperature and strain rate at such fine length scales has prevented direct experimental verification of these models. Wright and Ravichandran (1997) showed that the theory captures the essential features of the strain distribution across the shear band by comparing it with the experimental results of Moss (1981). Grady (1992, 1994) viewed a shear band as a propagating feature with a well defined front, containing a process zone where most of the adiabatic heating and stress relaxation occurs. He developed models to predict the length and the width of such a process zone and was able to estimate the rate of energy dissipation within this zone. Once again, lack of experimental data to date at such length scales has prevented direct comparisons. Taking an entirely different point of view, in the single edge notched geometry, Gioia and Ortiz (1996) developed a theory by modeling the shear band as a consequence of the evolving boundary layer between the top and the bottom halves of the specimen. They proposed that within the boundary layer, the unstable shear band is the region where the plastic work exceeds a critical value and as a consequence the tip of a shear band is diffuse in

nature, with no singularity associated with it. Their predictions of shear band speeds were in close agreement with those measured by Zhou *et al.* (1996a).

In the light of the existing body of knowledge, an experimental investigation has been undertaken to address some of the issues discussed above. Detailed measurements of the mixed mode stress intensity factor histories are made and some questions regarding the failure mode transition are addressed. Using the recently developed IR high speed camera, the two dimensional structure of a shear band tip is imaged and the temperature distribution along the shear band is presented. Optical microscopy of certain interesting geometric features of shear bands is also discussed.

## **3.2 Experimental Techniques**

### **3.2.1 Material and Specimen Geometry**

In order to study the initiation of a shear band from the tip of a preexisting crack and its subsequent propagation, a single edge notched specimen geometry, similar to that introduced by Zhou *et al.* (1996a), was chosen. This geometry was a modification of the double edge notched geometry used by Kalthoff and Winkler (1988). The specimen geometry and the loading arrangement are schematically illustrated in Fig. 1. The specimen is made of C300 maraging steel, the composition of which is shown in Table 1. The specimens were age hardened by holding them at 482°C for 5 hours, followed by air

cooling. An EDM notch (260  $\mu\text{m}$  wide) was made on the edge as shown in Fig. 1, which was further extended by 2 mm by fatigue loading. One of the specimen faces was lapped and polished to make it specularly reflective, in order to use it for the optical interference technique of coherent gradient sensing (CGS). The specimen is impacted on the edge under the notch, with a 127 mm long cylindrical projectile, 50mm in diameter, to produce a mixed mode stress field at the crack tip. The projectile is accelerated using a gas gun. The specimen is supported at three points as shown in the Fig. 1. No supports are actually required for the specimen to fail, as demonstrated in the previous experimental investigations. The reason for introducing the supports is to hold the specimen at a more or less fixed location during the loading process, the purpose of which will be discussed in more detail in a later section.

In the current investigation, two diagnostic techniques were used to observe the crack tip and the propagating shear band. On one side of the specimen, the optical technique of CGS in reflection was used to monitor the evolution of the stress intensity factors as a function of time. On the other side of the specimen, a newly developed full-field, high-speed infrared imaging system was employed to measure the evolving, two dimensional temperature field. These techniques are briefly described below.

### **3.2.2 Coherent Gradient Sensing (CGS)**

The optical technique of CGS is a shearing interferometric technique that is sensitive, in reflection mode, to the in plane gradients of the out of plane displacements. Detailed

description of the technique, the equations governing the optical mapping and fringe formation, can be found in the original papers by Tippur *et al.* (1990, 1991) and in the review article by Rosakis (1993). A schematic illustration of the experimental setup along with the optical technique is shown in Fig. 2. The coordinate system used is shown in Fig. 1. For opaque materials, this technique involves reflecting a collimated laser beam from the surface of the deforming specimen and optically shearing it by sending it through two high density gratings separated by a distance  $A$ . This gives rise to multiple diffraction spots of orders  $0, \pm 1, +2, \dots$  and the interference fringe pattern given by the  $+1$  or the  $-1$  order spot is recorded by the imaging system. In the current experiments, the beam has been sheared in a direction perpendicular to the crack. The governing equation for interpreting the interference fringes is:

$$u_{3,2} = \frac{\partial u_3}{\partial x_2} = \frac{np}{2\Delta} \quad (1)$$

where  $u_3$  is the out of plane displacement of the specimen surface,  $x_2$  is the direction of shearing of the beam,  $n$  is the fringe order and  $p$  is the pitch of the gratings, which is  $25.4 \mu\text{m}$  in the current investigation. Thus, each fringe represents the locus of constant  $u_{3,2}$  on the specimen surface. Since the fringes are sensitive to the gradients of displacements, they are insensitive to rigid motions of the specimen during deformation, which is one of the distinct advantages of CGS, not shared by other full field optical techniques. In the present set of experiments, the shearing direction was chosen to be  $x_2$ , considering the flexural waves that are generated in the specimen upon projectile impact. These waves are cylindrical in nature, flexing the specimen along the  $x_1$  direction. Hence, if the laser beam were sheared in the  $x_1$  direction, the fringes obtained would be the result of not only the out of plane deformation due to crack tip singular field, but also the out of plane

displacements due to the flexural waves. Shearing the beam in the  $x_2$  direction filters out the out of plane displacements due to the flexural waves, because of their cylindrical nature, and the resulting fringes are due to the crack tip deformation field only. This is illustrated in Fig. 3 for the case of a mode I loading. Two maraging steel specimens, 12 mm thick, were impacted by a cylindrical steel projectile at 35 m/s to produce mode I loading at the crack tip as illustrated in the schematics on the left-hand side of Fig 3. In Fig. 3a, the beam was sheared along the crack direction, as shown by the arrow, and in Fig. 3b, the beam was sheared perpendicular to the crack direction. The synthetic, ideal fringes for full  $K_I$  dominance in each case are shown next to the schematics for comparison. A sequence of two CGS images resulting from crack tip loading in each case is also shown next to the synthetic fringes. The fringe patterns clearly show the effect of the flexural waves. In Fig. 3a, the fringes due to the waves are superposed on the fringes due to the crack tip displacement field and a very complicated combined fringe pattern emerges. Whereas, in Fig. 3b, the fringes due to the waves are filtered out and only the fringes due to the out of plane displacements are captured. By comparing with the synthetic fringes, it can be concluded that the experimental fringes in Fig. 3(b) correspond to a mode I, opening,  $K_I$  dominated crack tip loading whereas the fringes in Fig. 3a do not correspond to any purely  $K$  dominated field. This exercise clearly demonstrates that care should be taken in interpreting the fringe patterns as it is entirely possible to conclude from Fig. 3a that there is no purely  $K$  dominant field around the crack tip, whereas in reality, there exists a  $K_I$  dominant field, which is merely coupled with the flexural wave field. Guided by this, in all subsequent experiments involving high

velocity projectile impact, the laser beam was sheared in  $x_2$  direction for measuring the stress intensity factors.

A gas gun accelerates a cylindrical projectile which impacts the specimen edge under the notch as shown. Upon impact, a strain gage attached to the specimen edge triggers an Argon ion laser (Coherent, Sabre Fred) to emit a series of 80 discrete coherent light pulses, (514.5 nm wavelength, 20 ns pulse width) with an inter-pulse time of 2  $\mu$ s. These pulses are then collimated to a diameter of 50 mm. These pulses pick up information about the out of plane displacement while reflecting on the specimen surface, pass through the CGS setup, and the resulting interference fringe patterns are recorded using a rotating mirror type high speed camera (Cordin 330A), capable of framing rates up to 2 million frames per second. The images are recorded on TMAX 3200 high sensitivity film. The field of view of the images was approximately a circle of 27 mm in diameter.

### 3.2.3 High Speed Infrared Thermography

#### 3.2.3.1 Two-dimensional *infrared* imaging system

Infrared thermography has been used for measuring temperature rise in dynamic deformation and failure experiments by many investigators in the past (Moss and Pond, 1975; Costin et al. 1979; Hartley et al. 1987; Marchand and Duffy, 1988; Zehnder and Rosakis, 1991, 1992; Mason and Rosakis, 1993; ; Zehnder et al., 1993; Kallivayalil and Zehnder, 1994; Zhou et al., 1996a; Guduru et al., 1998; Li and Lambros, 2000;

Hodowany *et al.*, 2000). All the investigations conducted so far have utilized either a single element detector or a linear array of detectors. Using a linear array of detectors, it is possible to measure temperature at a series of discrete points along a line on the specimen surface. Such detectors have been successfully used by Zehnder and Rosakis (1991) and Mason and Rosakis (1993) to measure the temperature rise across a propagating opening crack in a high strength steel. Costin *et al.* (1979), Hartley *et al.* (1987), Marchand and Duffy (1988) and Zhou *et al.* (1996a) used them to measure the temperature rise across a propagating shear band in steels. However, the linear arrays of detectors are ideal to measure temperature distribution across features that are essentially one-dimensional and steady. Although a great deal of information can be obtained with the linear arrays of high speed IR detectors, given the highly transient two-dimensional nature of the shear band tip and the significance of its structure in understanding the mechanics of shear bands, it would be desirable to have an instrument that can measure dynamically varying temperature field in an area instead of at points along a line. Since several events involving dynamic deformation in solids occur at time scales of tens of microseconds, such measurements can be accomplished using a two-dimensional square array of IR detectors acquiring images at rates of around 1MHz.

Although there have been great advances in 2-D infrared (IR) imaging systems in recent years, there are no commercial systems capable of imaging at such high speeds. IR imaging systems typically run at television rates, 30 Hz, although higher speed systems do exist, with rates of up to 34kHz. To achieve the required framing rates of up to 1MHz requires very fast and temporally frozen data acquisition in conjunction with a high-speed

2-D IR detector array. The bottleneck in performing such measurements has been data acquisition. However, utilizing the fast, relatively inexpensive digitizers which are now available, a 2-D IR imaging system has recently been designed and built at Caltech. This instrument, for the first time, enabled the measurement of thermal fields at rates of up to 1 million frames per second. The complete imaging system, consisting of the focusing optics, IR focal plane array, multiplexing circuits, and data acquisition boards is shown in the block diagram of Fig. 4. At the heart of the system is an 8x8 focal plane array of HgCdTe IR detector elements. Each detector element is  $100\mu\text{m} \times 100\mu\text{m}$ , with center to center spacing of  $130\mu\text{m}$ . Each of the 64 elements has its own preamplifier, the outputs of which are fed into a bank of eight 8:1 multiplexers. The multiplexed signals are then digitized using 4 two-channel, Gage 1012 A/D boards, running at speeds up to 10MHz. Radiation emitted from the object as it deforms and heats up is focused onto the IR focal plane array using a reflective lens, built up out of two Schwarzschild objectives, each operating at infinite conjugation ratio. The ray diagram for the focussing optics is shown Fig. 5. A photograph of the camera is shown in Fig. 6. The magnification of each lens is fixed, thus to achieve different magnifications, different lenses are used. In the current investigation, a magnification of 0.9 was used. At this magnification, each detector would be measuring the average temperature over an area of  $110\mu\text{m} \times 110\mu\text{m}$ . In this system, there is no integration of the signal between frames as in commercial IR cameras; thermal resolution is sacrificed in favor of speed. The system rise time is approximately 750ns. The details of each of the components of the system and the results of some preliminary applications of the system are given in Zehnder *et al.* (2000). It was experimentally found that the system cross talk is about 12%, and as a result, if the image of a thin ( $\sim 75\mu\text{m}$

diameter) hot wire is focussed on a row of detectors, the neighbouring row of detectors also responds, even though no signal is expected out of it. The signals from the neighbouring row are about 12% of the signals from row on which the image is focussed. Two of the important sources of cross talk are electronic and optical in nature. The former is due to the electronic coupling between the neighbouring detectors on the array. Optical cross talk arises because of imperfect optical focussing, owing to various aberrations in the focussing system as well as the errors in assembling the system. No attempt has been made here to correct for the cross talk. As a consequence, the thermal images obtained would be somewhat blurred images of the actual temperature distribution on the specimen. In order to convert the voltage signals from the detectors to corresponding temperatures, an output signal vs. temperature rise calibration curve is obtained for the detectors.

### 3.2.3.2 *IR system calibration*

Calibration of the system is performed in a direct manner. A sample of the same material and surface finish as will be tested is heated in an oven by several hundred degrees. The heated sample, instrumented with a thermocouple to record its surface temperature, is placed in the object position. As the sample cools, the voltage output from each of the IR elements is recorded by the data acquisition system along with the sample temperature. This procedure provides a voltage vs. temperature curve for each element. Since the IR system is AC coupled, the input radiation to the detectors must contain an AC

component. This is achieved by placing a chopping wheel in front of the heated calibration specimen.

Great care should be taken during the calibration procedure since any errors made at this stage are directly reflected in the final measurements. Further, oxidation of the sample surface when heated to high temperatures during calibration changes its emissivity substantially, rendering the calibration curve inapplicable. The ideal way to overcome the oxidation problem is to perform the calibration in vacuum or in an inert gas atmosphere, both of which are experimentally cumbersome procedures. As an alternative, the following procedure has been adopted. First, the sample was heated up to a temperature at which no oxidation takes place on its surface, about 225°C in this case, and a calibration is performed while it cools down to room temperature. In order to verify that indeed no oxidation has taken place, the same sample, without modifying the surface condition in anyway, is heated repeatedly to 225°C and the calibration curves are obtained. The curves obtained in four such repetitions, for one of the 64 detectors, are shown in Fig. 7. The proximity of all of them to each other confirms that there was no oxidation up to 225°C. Next, the specimen was heated to a higher temperature, about 525°C and a calibration was performed while the specimen cooled down. This curve, along with the curve obtained by heating the specimen up to 225°C, is shown in Fig. 8. The ratio of these curves to each other represents the ratio of the emissivities of the two surfaces. This ratio is plotted as a function of temperature rise in Fig. 9. It can be seen that this ratio, after some initial non-linearity, settles down to a constant value 1.55, which is essentially the ratio of the emissivity of the oxidized surface to that of the non-

oxidized surface. The calibration curve corresponding to the non-oxidized surface is then extended to higher temperatures by simply dividing the calibration curve of oxidized surface by the factor 1.55. It should be noted that during a dynamic experiment, the temperature elevations of interest happen at such short time intervals that no oxidation has the time to build up during the observation window.

### 3.2.3.3 *Specimen support and triggering*

Another important issue where great care should be taken while making temperature measurement is in properly supporting the specimen. Traditionally, the edge impacted specimens for studying shear bands are not supported since failure initiates within the first few reflections of the stress waves emanating from the impact site. However, the initial stress waves impart a translation velocity to the specimen in the direction of impact. Usually, the time window of temperature measurement in a specific area on the specimen surface, such as at the crack tip, following the impact is of the order of 100 $\mu$ s. If the projectile impacts the specimen at a speed of 35m/s, and assuming that the characteristic translation speed of the specimen has a similar magnitude, the specimen travels a distance of 3.5mm during the time of measurement. Hence, each detector would measure temperature not at a particular targeted point on the specimen, but at a series of points along a line as they travel across the field of view of the IR camera. In order to ensure that each detector measured temperature at the same location, the specimen was supported at three points as shown in Fig. 1, preventing translations and rotations. These supports would certainly affect the evolution of the stress intensity factors at long times

but would not have any effect during the first 30-40 $\mu$ s, before the reflected waves from the supports reach the crack tip.

During the experiment, the same strain gage on the specimen, which upon impact triggers the laser pulses, also triggers the data acquisition system for the IR camera, initiating thermal image acquisition. The specimen was impacted at speeds ranging from 10m/s to 38m/s. The primary objectives of infrared imaging in the current investigation were to image the development of the plastic zone at the preexisting crack tip and its transition to a shear band, to image the temperature structure of the tip of a propagating shear band and to investigate the temperature distribution along such a band. In order to observe the plastic zone, the IR camera was focussed at an area around the fatigue crack tip and in order to investigate the structure of the propagating band, the area of observation was located 3.5mm in front of the crack tip, along the expected path of the shear band.

### **3.3 Experimental Results**

#### **3.3.1 Failure Modes**

The experiments conducted can be divided into four groups. (i) Those in which the impact speed ( $v$ ) was less than 13m/s. A crack tip plastic zone was observed and there was no crack initiation. (ii) 13m/s  $< v <$  26m/s. In this speed range, the crack initiated in opening mode, at an angle to the crack line, after several wave reflections. (iii) 26m/s  $< v <$  32m/s. In these experiments, a shear band initiated, propagated and arrested within the

specimen. This was followed by a failure mode switching to an opening crack from the tip of the arrested shear band at an angle to the shear band direction. (iv)  $v > 32\text{m/s}$ . At these high impact speeds, the shear bands propagated through the entire width of the specimen. Some illustrative cases will be examined in detail next.

### 3.3.2 Stress Intensity Factor History when $v < 26\text{m/s}$

When the impact speed was below  $13\text{m/s}$ , no failure mode (neither crack nor shear band) initiation was observed. However, beyond  $13\text{m/s}$ , a crack initiated in locally opening mode at an angle to the initial crack line. A sequence of CGS images illustrating the history of mixed mode stress field from impact until crack initiation is shown in Fig. 10, from the experiment with an impact speed of  $15.5\text{m/s}$ . The pictures have a black rectangular patch on them, which is a scale marker stuck on the specimen surface. The images show a mixed mode field, consisting of compressive mode I and shear mode II components, building in magnitude up to  $76\mu\text{s}$ , as demonstrated by the increasing size of the fringes. Also, the fringes are seen to rotate, indicating a shift towards a higher mode I stress intensity factor. Beyond  $76\mu\text{s}$ , the stress intensity factors are seen to decrease and become almost zero around  $132\mu\text{s}$ . This is followed by a build up of a mixed mode field, comprised of a tensile opening stress field and a shear stress field. At  $164\mu\text{s}$ , critical conditions for crack initiation under mixed mode conditions are reached and the initiated crack, along with the waves released in the initiation process, can be discerned in the last image of Fig. 10. When the impact speed is less than  $13\text{m/s}$ , the stress intensity factors do not build up enough to cause crack initiation. Before attempting to devise an appropriate

way to extract the stress intensity factors from the fringes, it is essential to understand the actual stress state at the crack tip in the presence of a fatigue crack tip.

According to the analysis of Lee and Freund (1990), when a single edge notched specimen is impacted under the notch, like in the current experiment, the resulting stress field at the crack tip would be mixed mode in nature, though shear dominated. The mode I stress intensity factor  $K_I$  would be negative. If the crack faces are separated initially, as in the case of a notch, the compressive part of the stress field brings the two crack faces closer to each other. Similarly, two points, one on each face of the crack, both initially located at equal distance from the notch tip, would also slide with respect to each other along the crack direction, due the shear component of the notch tip stress field ( $K_{II}$ ). This is illustrated in Fig. 11a. The point O is the notch tip and it is the origin for the singular stress fields. Now let us examine the case of a mathematically sharp crack, all along its length, subjected to the same impact loading. This is illustrated in Fig. 11b. Since the crack faces are already in contact, they can not be brought any closer and thus, no negative mode I stress intensity factor  $K_I$  can develop, rendering  $K_I$  to be identically zero. Thus, there can be only sliding of one face relative to the other, which means that there can only be a mode II stress intensity factor  $K_{II}$ . This  $K_{II}$  is clearly a combined result of the applied boundary load and the frictional traction distributed along the crack faces. And this is also the stress intensity factor that is experienced by the material in front of the crack tip and governs the failure processes therein. Any optical technique that is based on measuring the field quantities such as the out of plane displacement or its gradient, such as the CGS, measures the value of this net  $K_{II}$ . As an extreme example, if

the frictional locking is severe enough to prevent any relative sliding, then the frictional traction developed along the crack faces would be such that it would produce a  $K_{II}$  which is exactly equal in magnitude but opposite in sign to that produced by the boundary loading, to render the net stress intensity factor at the crack tip to be identically zero.

Now let us turn to the events at the notch tip with a fatigue precrack. Along the fatigue crack, the crack faces are already in contact. This is illustrated in Fig. 12. O is the notch tip, and O' is the fatigue crack tip. After the waves from the impact site arrive, the crack tip area is deformed as illustrated in Fig. 12b. Points A and A' come closer to each other as well as slide with respect to each other. Points B and B' can only slide with respect to each other. This situation can be described as the combination of the two loading scenarios illustrated in Fig. 12c and d. Since the crack faces can come close to each other only to the left of point O, there would be a compressive mode I singular stress field with O as its origin and there will be a mode II singular field with O' as the origin. The net stress intensity factor  $K_{II}$  acting on the material at O' is the combination of the boundary loads and the distributed frictional traction on the fatigue crack faces. Thus, stress at a point P in Fig. 12e can be described as

$$\sigma_{ij}(r_1, r_2, \theta_1, \theta_2) = \frac{K_I}{\sqrt{2\pi r_1}} f_{ij}^I(\theta_1) + \frac{K_{II}}{\sqrt{2\pi r_2}} f_{ij}^{II}(\theta_2) \quad (2)$$

when  $K_I$  is negative.  $r_1, r_2, \theta_1, \theta_2$  are defined in Fig. 12e.  $\sigma_{ij}$  are the components of stress, and  $f_{ij}^I$  and  $f_{ij}^{II}$  are the known angular functions.  $K_I$  is the stress intensity factor for the

mode I compressive singular field which acts with O as its origin and  $K_{II}$  is the stress intensity factor for the mode II singular field which acts with O' as its origin. However, when the mode I component of the stress field is positive, i.e., opening, naturally, O' is the origin for both components of the singular field and the stress at the point P can be described as

$$\sigma_{ij}(r_2, \theta_2) = \frac{K_I}{\sqrt{2\pi r_2}} f_{ij}^I(\theta_2) + \frac{K_{II}}{\sqrt{2\pi r_2}} f_{ij}^{II}(\theta_2) \quad (3)$$

Using, equation (2), the governing equation (1) for analyzing the CGS fringes reduces to

$$\frac{np}{2\Delta} = \frac{vh}{2E\sqrt{2\pi}} \left[ K_I r_1^{\frac{3}{2}} \sin \frac{3\theta_1}{2} + K_{II} r_2^{\frac{3}{2}} \cos \frac{3\theta_2}{2} \right] \quad (4)$$

where  $n$  is the fringe order,  $p$  is the pitch of the gratings,  $\Delta$  is the distance between the gratings,  $\nu$  is the Poisson's ratio,  $h$  is the specimen thickness and  $E$  is the specimen Young's modulus. The fringes are digitized and the above equation along with the least squares procedure, described by Mason *et al.* (1992), is used to extract  $K_I$  and  $K_{II}$ . In order to verify the accuracy of the calculation procedure, the extracted  $K_I$  and  $K_{II}$  are used to generate synthetic CGS fringes, which are compared with the experimental fringes, as illustrated in Fig. 13. The good agreement between the two testifies to the accuracy of the procedure. It should be noted that the artificial fringes are able to reproduce the structure of the fringes close to the crack tip, which is a consequence of using two origins O and O' for the mode I and mode II singular fields respectively. However, since the length of the

fatigue crack is only 2 mm, if the digitized fringes are sufficiently far away from the crack tip, calculation of  $K_I$  and  $K_{II}$  as described above would not be very different from a calculation based on just one origin, such as  $O''$  in Fig. 12e, for both singular fields. The stress intensity factors have been computed employing both methods for a few cases and the difference between the stress intensity factors obtained was within the estimated errors in their calculation, though the latter approach was not be able to reproduce the fringe patterns very near the crack tip as good as the former.

Fig. 14 presents the evolution of the normalized  $K_I$  for four different experiments as a function of normalized time. The normalizing parameter  $K'$  is the same as that used by Mason *et al.* (1992),

$$K' = \sqrt{\frac{l}{\pi}} \frac{E\nu}{2c_d^{pI-\sigma}}$$

where  $l$  is the initial crack length,  $\nu$  is the impact speed and  $c_d^{pI-\sigma}$  is the plane stress dilatational wave speed. Time is normalized with  $l/c_d^{pI-\sigma}$ . Fig. 15 shows the evolution of  $K_{II}$  for the same four experiments. The normalizing factors used are the same as those used for  $K_I$ . A closer examination of the data at early times allows comparison with the analytical and numerical results of Lee and Freund (1990) and the previous experimental results of Mason *et al.* (1992). These comparisons for  $K_I$  and  $K_{II}$  are shown in Figs. 16 and 17 respectively. The agreement is very good for  $K_{II}$  and is reasonably good for  $K_I$ . The differences could probably be attributed to the presence of the fatigue crack. The

value of  $K_{II}$  peaks around a normalized time of 10 and reaches a minimum around 20. These values are most likely related to the length of the projectile which is approximately 5 times the length of the crack,  $l$ , and hence the length of the loading pulse is  $10l$ . The magnitude and the time period of the oscillation in  $K_{II}$  and  $K_I$  are in good agreement with the numerical simulations of Rittel and Levin (1998) and Roessig and Mason (1998) despite the difference in the boundary conditions.

### 3.3.3 Incipient Shear Banding when $v < 26$ m/s

When the projectile speed was less than 26m/s, though the crack initiated in an opening mode at an angle to the crack line, a microscopic examination of the crack tip area reveals a small and thin arrested shear band at the tip of the initial crack. This was observed in all experiments with impact speeds ranging from 10 to 26m/s. An optical micrograph of the sample from the crack tip area, polished and etched, is shown in Fig. 18. The arrested shear band can be seen as a thin white band. The length of the band varied from one experiment to another and the longest observed was about 0.5mm. Examining the history of  $K_{II}$ , it can probably be concluded that this band initiated around or before a normalized time of 10, when the magnitude of  $K_{II}$  reached a peak value. Assuming that an increasing  $K_{II}$  provides the driving force for the shear band to propagate, it would have arrested when  $K_{II}$  started to decrease. Subsequent wave reflections would result in a mixed mode field with a strong opening mode I component, leading to crack initiation in opening mode. Based on this observation, it appears that the

failure mode transition has a significantly different connotation in this material from the traditional view and will be discussed in a subsequent section.

### 3.3.4 Stress Intensity Factors when $v > 26\text{m/s}$

When the impact speed is greater than  $26\text{m/s}$ , a shear band initiates and propagates from the tip of the crack. A sequence of CGS images leading up to the initiation of shear band is shown in Fig. 19, for the case where the impact speed was  $38\text{m/s}$ . The shear band initiation can be identified by the elongated dark region at the crack tip, which continues to propagate in the subsequent images. The fringe patterns up to initiation are analyzed in the same way as described above. The stress intensity factors increase rapidly and the critical values of  $K_I$  and  $K_{II}$  at the time of initiation for six different experiments are shown in Figs. 20 and 21 respectively. From Fig. 21, it appears that there is a critical range of  $K_{II}$ , within which the shear band initiates from a pre-fatigued initial notch. Chen and Batra (1998a-c) proposed that since the stress intensity factors determine the stress and strain fields near the crack tip, they could potentially be used to formulate a criterion for shear band initiation under adiabatic conditions. Data presented in Fig. 21 seems to support such a proposal. From Fig. 20, it appears that the value of  $K_I$  at initiation may not have a significant role in determining the critical conditions, possibly because it represents a compressive singular field about the notch tip  $O$  and not the fatigue crack tip  $O'$ . The critical  $K_{II}$  criterion gains further support if the results of Fig. 21 are combined with the peak  $K_{II}$  values of the experiments with  $v < 26\text{ m/s}$ , as shown in Fig. 22. As discussed in the previous section, if it is assumed that the arrested incipient shear bands

which always appear in those experiments, initiated close to the peak value of  $K_{II}$ , then irrespective of the subsequent propagation history, a shear band appears to have initiated within a narrow range of  $K_{II}$  values. However, this result should be qualified by stating that shear bands are extremely sensitive to the geometry of the inhomogeneities at which they are initiated, in this case, a fatigue crack tip. Thus, a substantial change in critical  $K_{II}$  could be expected if a notch tip was used instead of a sharp fatigue crack tip.

### 3.3.5 Shear Band Propagation Speed

Fig. 23 shows a sequence of CGS images illustrating the propagation of the shear band following its initiation. Figs. 24 and 25 show the advance of the shear band and its velocity in five different experiments. In order to obtain the velocity plot, every set of three consecutive points in Fig. 24 is fitted with a second order polynomial and the slope of this polynomial at its mid point is taken to be the velocity at that point. The velocities computed have an uncertainty of  $\pm 80$  m/s. The shear band velocity can be seen to be highly transient and a function of the impact speed. In all but one experiment, the band arrests momentarily at about  $30\mu\text{s}$ , before accelerating to high speeds. Such transient behavior, not observed in the previous similar investigations (Zhou *et al.* 1996a), could be because of the different boundary conditions used here. The maximum shear band speed observed here is about 1100 m/s. Freund *et al.* (1985) estimated the speed of a shear band in certain steels to be  $0.57C_s$ , which is about 1700 m/s. Though the positive slope of the curves in Fig. 25 suggests increasing speeds, further investigations are necessary to determine the limiting speed for a shear band.

### 3.3.6 Crack Initiation Under Mixed Mode Loading

In the experiments, where the impact speed was less than 26m/s, the crack initiated at an angle to the crack direction, after several wave reflections. This angle is determined by the mode mixity at the time of crack initiation. Similarly, when the impact speed was only slightly above 26m/s, a shear band initiated at the crack tip, propagated a few millimeters and arrested within the optical field of view. In such cases, the CGS images capture the subsequent development of mixed mode field at the arrested shear band tip, leading to an opening crack initiating at an angle to the initial crack direction. Thus, the current experiments provide an opportunity to investigate the dynamic crack initiation behavior under mixed mode conditions. Fig. 26 shows results taken from five experiments. The mode mixity is plotted as the abscissa, represented by the mixity parameter  $\tan^{-1}(K_{II}/K_I)$  and the crack initiation angle is plotted as the ordinate. The discrete points are the experimental results. The solid line represents the He and Hutchinson (1989) maximum energy release rate criterion and dashed line represents the local pure mode I criterion. Though the models predict a consistently higher value for the crack initiation angle than what was observed in the experiments, the agreement can be described as reasonable, given the errors in measuring the stress intensity factors.

### 3.3.7 Micrographs of Shear Bands

Fractured specimens were examined using an optical microscope to study the features of the shear bands such as its width, trajectory, etc. Specimens for microscopy were prepared by cutting small samples from the area of interest using electric discharge machining (EDM). Surface of interest was then polished down to  $0.25\mu\text{m}$ , followed by etching with 2% nital solution. Fig. 27 is a photograph of an arrested shear band in the specimen. The shear band is revealed as a white stripe. This white band represents the area where the temperature increase was high enough to cause a solid-solid phase transformation. The thickness of the band is about  $40\text{-}50\mu\text{m}$ . Fig. 28 shows a scanning electron microscope (SEM) image of the specimen surface that failed by shear band propagation. The image shows elongated voids, with sheared edges that are characteristic of such a failure mode.

Meyers (1994) has made an interesting observation about the possibility of shear band branching, by presenting a micrograph of a shear band that showed **bifurcation**. Here we report some of our observations that support such a possibility. Fig. 29 shows three micrographs that show possible shear band bifurcation. In the first two, the left edges are the failure paths, caused by a propagating shear band. The third image is taken from an arrested shear band. The possible branching behavior is clearly seen. To our knowledge, there is no theoretical framework to explain such a phenomenon, and we feel that this interesting observation requires further investigation to understand the possible conditions under which such bifurcation can take place.

### **3.3.8 Temperature Measurement**

### 3.3.8.1 *Temperature field at the crack tip*

One of the objectives of imaging the temperature field was to visualize the development of the mode II plastic zone at the tip of the initial crack and to observe its evolution through further localization into a shear band. The IR camera was focussed at the tip of the fatigue crack as illustrated on the left-hand side of Fig. 30. The impact speed was about 35 m/s. The figure also shows a sequence of thermal images showing the development of the temperature field as a function of time. It should be remembered that the actual data is collected at 64 discrete points. The images shown here are the projections of contour lines drawn on a surface fitted through the 64 points in the  $x_1$ ,  $x_2$  and temperature rise,  $\Delta T$ , space. The black lines on these images were artificially superimposed to represent the supposed approximate location of the initial crack tip. The position of the crack was inferred from the temperature patterns. Plasticity gradually builds up, with the characteristic shape of a mode II dominated plastic zone. Starting at about 21  $\mu\text{s}$ , the central hot region extends to the right, signifying the process of shear localization. The measured highest temperature rise within the plastic zone when this happened was at least 80K. Since each detector averages temperature rise over an area of  $110\mu\text{m} \times 110\mu\text{m}$ , spatial features smaller than this can not be resolved in these measurements. This is the first time that such two dimensional thermal images were obtained that clearly capture the transition of the initial crack tip plastic zone into a shear band.

A specific feature of interest here is the shape of the plastic zone prior to shear localization. In the numerical analyses of Needleman and Tvergaard (1995) and Ravi-Chandar (1995), it was observed that the plastic zone is elongated straight ahead of the crack and it also possesses a short, tail like extension on the side of impact, at about  $-135^\circ$  to the crack line. The current IR measurement was able to resolve such features, as illustrated in Fig. 31. This figure shows a qualitative comparison between the simulations of Needleman and Tvergaard (1995) and our current experimental results of the temperature rise within the plastic zone. The two pictures are shown at same scale. The comparison is for nominally the same impact speed and at almost the same time after impact. The difference lies in the material properties. The steel used in the current investigation is about 40% stronger than the one used in their simulations. In spite of the differences, the agreement between the size and shape of the plastic zones is indeed remarkable.

### 3.3.8.2 *Structure of the tip of a propagating shear band*

Next we turn our attention to the temperature field associated with the tip of a propagating shear band. There have been numerous speculations about its existence and the nature of an autonomous stress-strain fields associated with it. In order to image the structure of such a propagating shear band tip, the IR camera was focussed at a distance of 3.5mm ahead of the initial crack tip, in the expected path of the shear band. Fig. 32 shows a sequence of thermal images that capture the thermal profile of the tip of the shear band as it propagates across the field of view. 15 $\mu$ s after impact, a very diffuse

temperature front can be seen entering the field of view. The front moves rapidly across the field of view and the temperature increases gradually. The temperature rises by at least 40K in  $4\mu\text{s}$  and the gradient of temperature increase is about  $5 \times 10^4 \text{ K/m}$  along the direction of propagation of the shear band. As noted above, since the spot size is  $110\mu\text{m}$ , and the width of the shear band is at most  $50\mu\text{m}$ , the temperature rise measured here is only a lower bound for the actual value. The tip of the first detectable temperature rise was seen to propagate across the field of view at a speed of about 500m/s. The very gradual nature of temperature rise at the front end of the shear band tends to support the notion of a very diffuse shear band tip, as opposed to a crack tip which carries a strong singularity in the field quantities. The idea of a diffuse tip was first proposed by Gioia and Ortiz (1996). From a boundary layer theory, they introduced the idea of a shear band tip that carries no discontinuities and is characterized by the accumulation of a critical amount of plastic work to render the material behind it unstable by virtue of the change in the nature of its stress strain behavior. The experimental results appear to support this idea.

### 3.3.8.3 *Temperature structure along a propagating shear band*

As the shear band propagates, the material within the band progressively accumulates large plastic shear strains within short times and the temperatures can quickly reach very high values. Of special interest in this investigation has been the temperature distribution along a well defined shear band. It has been consistently observed, in all experiments where a propagating shear band was imaged, that the temperature distribution along the

band is highly non-uniform, with discrete regions of high temperature, that look like “hot spots.” These hot spots are also seen to translate along the length of the band. Fig. 33 shows one such image where the hot spots can be identified easily. In this image the hot spots are spaced at about  $250\mu\text{m}$  and in general the spacing varied from  $250\mu\text{m}$  to  $1\text{mm}$ . This observation raises questions about the spatial and temporal nature of shear deformation inside a shear band, which until now has been assumed to be essentially laminar in all available theoretical models. The high speed images obtained here show the shearing process to be far from laminar and the hot spots observed indicate a possible instability operating at the band width length scale, similar to certain hydrodynamic instabilities observed in fluids. Since in a shear band, a very thin layer of high temperature material is subjected to very high shear strain rates, the situation may resemble that of a viscous fluid confined between two rigid plates moving parallel to each other, known as the plane Couette flow in the fluid dynamics parlance. Since the plane Couette flow could become unstable and turbulent under certain conditions, it was conjectured that the hot spots observed in the current experiments probably indicate certain instabilities of the deformation process. This led us to examine the stability characteristics of the plane Couette flow.

It is well known in fluid mechanics that plane Couette flow of inviscid as well as viscous fluids is linearly stable. However, the situation is different if the viscosity of the fluid is a function of temperature since viscous dissipation increases local temperature. The linear stability of plane Couette flow with viscous heating was numerically studied by Sukanek *et al.* (1973) and later with improved numerical accuracy by Yueh & Weng (1996). It was

found that perturbations of finite wave numbers along the flow direction grow unboundedly beyond a critical Reynolds number, leading to eventual turbulence. This lends credence to our notion of the analogy with a flow related instability in a shear band since the temperature rise in a shear band decreases local viscosity of the material. Yet, there are major differences between a shear band and the Couette flow with viscous heating. The shear band temperatures are approximately one-half of the melting temperature of steel, indicating that the local shear band behavior can not be necessarily approximated by that of a viscous fluid. Indeed, a more appropriate description of the material behavior would be one of a thermo-viscoplastic material.

Motivated by observations at an entirely different length scale, namely, the existence of ductile shear zones with spatial periodicity in the earth's lower crust, where the material is constantly sheared, Molinari and Leroy (1991) conducted a two-dimensional quasi-static perturbation analysis of a layer of thermo-viscoplastic material subjected to shearing at the boundaries, as shown in Fig. 34. The viscosity of the material they modeled was an exponentially decreasing function of temperature. They investigated the possibility of the existence of any perturbations with a finite wave number in the direction along the band that could become unstable and grow as the deformation proceeds. They found that for certain material properties, such perturbations do exist and they lead to periodic hot spots along the length of the shear band as also illustrated in Fig. 34. These results, although quasi-static, can be used to understand the present case of a shear band since the material used in the current investigation has properties that are close to those of the material used in their analysis. The results of Molinari and Leroy

(1991) show that the non-dimensional wave numbers of unstable perturbations range from 0.02-0.1, which, using a shear band width of 40  $\mu\text{m}$  (Fig. 27), would mean wavelengths of about 1.2 mm to 5.0 mm. In the current experiments, the distance between the hot spots was seen to be between 250  $\mu\text{m}$  and 1.0mm (Fig. 33), which is lower than the range predicted by their analysis, but well within the order of magnitude, supporting our hypothesis that the observed nonuniform features are related to an instability of laminar flow of the material within the shear band. This finding calls for models that account for such microstructures in order to accurately estimate the energy dissipation in shear bands and to describe the dynamics of shear band formation, growth and arrest. Motivated by the current experimental observations, detailed numerical simulations are currently underway in order to investigate the microstructure of the shear bands using mesh-less numerical schemes (Li *et al.*, 2000a,b).

### **3.4 Concluding Remarks**

Impact experiments have been conducted on single edge notched specimens made of C300 maraging steel to study impact induced failure mode transition by simultaneously employing the optical technique of CGS and the high speed 2-D thermal imaging. Macroscopically, a failure mode transition from an opening crack to a shear band was observed at a critical impact speed of 26m/s. However, a closer examination of the initial crack tip area reveals a small arrested shear band even in the experiments with sub-critical impact speed. When the impact speed is below 26m/s, the band arrests immediately and the crack initiates from the tip of the pre-fatigued crack in opening

mode after multiple wave reflections. The two dimensional thermal images of the shear band initiation and propagation processes present several new observations. The shear band tip is seen to possess a very diffuse structure, with a gradual increase in temperature. A rather surprising finding from this investigation has been the non-uniform temperature distribution along a shear band. This observation has been possible due to the high speed IR camera developed for such applications. All analytical and numerical models of propagating shear bands so far have assumed a laminar deformation for the material within the shear band. New models are required to account for the non-uniform temperature distribution, which directly affects the energy dissipation in a shear band.

One of the limitations of the current temperature measurements is that each detector averages over an area of  $110\mu\text{m} \times 110\mu\text{m}$ , which is too large for making accurate temperature measurements of the shear bands which are only  $40\mu\text{m}$  in width. The experiments presented here are the first two dimensional temperature images of shear bands that were obtained using the new high speed IR camera. More refined experiments with smaller spot size to resolve temperatures across the width of the band are currently underway.

## References

- Bai, Y.L. (1982) Thermo-plastic instability in simple shear. *Journal of the Mechanics and Physics of Solids* **30**, 195-207.
- Bai, Y.L. and Dodd, B. (1992) Adiabatic shear localization: Occurrence, theories and applications. Pergamon Press, Oxford.
- Chen, L. and Batra, R.C. (1998a) Shear instability direction at a crack-tip in a thermoviscoplastic body. *Theoretical and Applied Fracture Mechanics* **29**, 33-40.
- Chen, L. and Batra, R.C. (1998b) Analysis of material instability at an impact loaded crack tip. *Theoretical and Applied Fracture Mechanics* **29**, 213-217.
- Chen, L. and Batra, R.C. (1998c) Material instability criterion near a notch-tip under locally adiabatic deformations of thermoviscoplastic materials. *Theoretical and Applied Fracture Mechanics* **30**, 153-158.
- Clifton, R.J. (1980) Material Response to Ultra High Loading Rates, NRC Report No. 356, U.S. National Material Advisory Board.
- Clifton, R.J., Duffy, J., Hartley, K.A. and Shawki, T.G. (1984) On critical conditions for shear band formation at high strain rates. *Scripta Metallurgica* **18**, 443-448.

Costin, L.S., Crisman, E.E., Hawley, R.H. and Duffy, J. (1979) On the localization of plastic flow in mild steel tubes under torsional loading. 2<sup>nd</sup> Conference on the Mechanical Properties of Materials at High Rates of Strain (Ed. Harding, J.) The Institute of Physics, London, 90-100.

Fruend, L.B., Wu, F.H. and Toullos, M. (1985) Initiation and propagation of shear band in antiplane shear deformation. Proceedings of the Considere Memorial Symposium, 125-143, Presse de l'Ecole Nationale des Ponts et Chaussees.

Gioia, G. and Ortiz, M. (1996) The two-dimensional structure of dynamic boundary layers and shear bands in thermoviscoplastic solids. *Journal of the Mechanics and Physics of Solids* **44**, 251-292.

Grady, D.E. (1992) Properties of an adiabatic shear band process zone. *Journal of the Mechanics and Physics of Solids* **40**, 1197-1215.

Grady, D.E. (1994) Dissipation in adiabatic shear bands, *Mechanics of Materials* **17**, 289-293.

Guduru, P.R., Singh, R.P., Ravichandran, G. and Rosakis, A.J. (1998) Dynamic crack initiation in ductile steels. *Journal of the Mechanics and Physics of Solids* **46**, 1997-2016.

Hartley, K.A., Duffy, J. and Hawley, R.H. (1987) Measurement of the temperature profile during shear band formation in steels deforming at high strain rates. *Journal of the Mechanics and Physics of Solids* **35**, 283-301.

He, M.-Y. and Hutchinson, J.W. (1989) Kinking of crack out of an interface. *Journal of Applied Mechanics* **56**, 270-278.

Hodowany, J., Ravichandran, G., Rosakis, A.J. and Rosakis, P. (2000) Partition of plastic work into heat and stored energy in metals. *Experimental Mechanics* **40**, 113-123.

Kallivayalil, J.A. and Zehnder, A.T. (1994) Measurement of the temperature field induced by dynamic crack growth in beta-C titanium. *International Journal of Fracture* **66**, 99-120.

Kalthoff, J.K. and Winkler, S. (1988) Failure mode transition at high rates of loading, *Proceedings of the international conference on impact loading and dynamic behaviour of materials* (Ed. C.Y. Chiem, H.D. Kunze and L.W. Meyer) 43-56, Deutsche Gesellschaft für Metallkunde.

Lee, Y.J. and Freund, L.B. (1990) Fracture initiation due to asymmetric impact loading of an edge cracked plate, *Journal of the Mechanics and Physics of Solids* **57**, 104-111.

Li, S., Liu, W-K., Hao, W. and Rosakis, A.J. (2000) Simulations of dynamic shear band propagation. Part I: Brittle to ductile transition. In preparation.

Li, S., Liu, W-K., Rosakis, A.J. and Guduru, P.R. (2000) Simulations of dynamic shear band propagation. Part II: Micro-structure of adiabatic shear band. In preparation.

Li, Z. and Lambros, J. (2000) Dynamic thermomechanical behavior of fiber reinforced composites. *Composites, Part A – Applied Science and Manufacturing* **31**, 537-547.

Marchand, A. and Duffy, J. (1988) An experimental study of the formation process of adiabatic shear bands in a structural steel. *Journal of the Mechanics and Physics of Solids* **36**, 251-283.

Mason, J.J., Lambros, J. and Rosakis, A.J. (1992) The use of a coherent gradient sensor in dynamic mixed mode fracture mechanics experiments. *Journal of the Mechanics and Physics of Solids* **40**, 641-661.

Mason, J.J. and Rosakis, A.J. (1993) On the dependence of the dynamic crack-tip temperature fields in metals upon crack-tip velocity and material parameters. *Mechanics of Materials* **16**, 337-350.

Meyers, M.A. (1994) *Dynamic behavior of Materials*. John Wiley & Sons, Mew York.

Molinari, A. and Clifton, R.J. (1987) Analytical characterization of shear localization in thermoviscoplastic materials. *Journal of Applied Mechanics* 54, 806-812.

Molinari, A. and Leroy, Y.M. (1991) Structures in shear zones due to thermal effects. *C.R. Acad. Sci. Paris., Serie II* 313, 7-13.

Moss, G.L. (1981) Shear strains, strain rates and temperature changes in adiabatic shear bands. In *Shock Waves and High-strain-rate Phenomena in Metals*, (Ed. M.A. Meyers and L.E. Murr), 299-312, Plenum, New York.

Moss, G. and Pond Sr., R.B. (1975) Inhomogeneous thermal changes in copper during plastic elongation. *Metallurgical Transactions* **6A**, 1223-1235.

Needleman, A. and Tvergaard, V. (1995) Analysis of a brittle-ductile transition under dynamic shear loading. *International Journal of Solids and Structures* 32,2571-2590.

Ravi-Chandar, K. (1995) On the failure mode transition in polycarbonate under dynamic mixed mode loading. *International Journal of Solids and Structures* **32**, 925-938.

Ravi-Chandar, K., Lu, J., Yang, B. and Zhu, Z. (2000) Failure mode transitions in polymers under high strain rate loading. *International Journal of Fracture* **101**, 33-72.

Recht, R.F. (1964) Catastrophic thermoplastic shear. *Journal of Applied Mechanics* 31, 189-193.

Rittel, D. and Levin, R. (1998) Mode-mixity and dynamic failure mode transitions in polycarbonate. *Mechanics of Materials* 30, 197-216.

Roessig, K.M. and Mason, J.J. (1998) Adiabatic shear localization in the impact of edge-notched specimens. *Experimental Mechanics* 38, 196-203.

Rogers, H.C. (1979) Adiabatic plastic deformation. *Ann. Rev. Mater. Sci* 9, 283-311.

Rosakis, A.J. (1993) Two optical techniques sensitive to gradients of optical path difference: the method of caustics and the coherent gradient sensor (CGS). In *Experimental Techniques in Fracture* (Ed. Epstein, J.), VCH, New York, 327-425.

Shawki, T.G. and Clifton, R.J. (1989) Shear band formation in thermal viscoplastic materials. *Mechanics of Materials* 8, 13-43.

Sukanek, P.C., Goldstein, C.A. and Laurence, R.L. (1973) The stability of plane Couette flow with viscous heating. *Journal of Fluid Mechanics* 57, 651-670.

Tippur, H.V., Krishnaswamy, S. and Rosakis, **A.J.** (1990) Coherent gradient sensor for crack tip deformation measurements: analysis and experimental results. *International Journal of Fracture* 48, 193-204.

Tippur, H.V., Krishnaswamy, S. and Rosakis, **A.J.** (1991) Optical mapping of crack tip deformations using the method of transmission and reflection coherent gradient sensing: a study of crack tip k-dominance. *International Journal of Fracture* **52**, 91-117.

Wright, T.W. (1987) Steady shearing in a viscoplastic solid. *Journal of the Mechanics and Physics of Solids* 35,269-282.

Wright, T.W. (1995) Scaling laws for adiabatic shear bands. *International Journal of Solids and Structures* 32,2745-2750.

Wright, T.W. and Ockendon, H. (1992) A model for fully formed shear bands. *Journal of the Mechanics and Physics of Solids* 40, 1217-1226.

Wright, T.W. and Ravichandran, G. (1997) Canonical aspects of adiabatic shear bands. *International Journal of Plasticity* **13**, 309-325.

Wu, F.H. and Freund, L.B. (1984) Deformation trapping due to thermoplastic instability in one-dimensional wave-propagation. *Journal of the Mechanics and Physics of Solids* 32, 119-132.

Yueh, C-S. and Weng, C-I. (1996) Linear stability analysis of plane Couette flow with viscous heating. *Physics of Fluids* **8**, 1802-1813.

Zehnder, A.T., Guduru, P.R., Rosakis, A.J. and Ravichandran, G. (2000) Million frames per second infrared imaging system. *Review of Scientific Instruments*, In press.

Zehnder, A.T., Ramamurthy, A.C., Bless, S.J. and Brar, N.S. (1993) Stone impact damage to automotive paint finishes – Measurement of temperature rise due to impact. *International Journal of Impact Engineering* **13**, 133-143.

Zehnder, A.T. and Rosakis, A.J. (1991) On the temperature distribution at the vicinity of dynamically propagating cracks in 4340 steel. *Journal of the Mechanics and Physics of Solids* **39**, 385-415.

Zehnder, A.T. and Rosakis, A.J. (1992) A note on the use of high speed infrared detectors for the measurement of temperature fields at the vicinity of dynamically growing cracks in 4340 steel. *Journal of Applied Mechanics* **59**, 450-452.

Zener, C. and Hollomon, J.H. (1944) Effect of Strain Rate Upon Plastic Flow of Steel. *Journal of Applied Physics* **15**, 22-32.

Zhou, M., Ravichandran, G. and Rosakis, A.J. (1996a) Dynamically propagating shear bands in impact-loaded prenotched plates – I. Experimental investigations of temperature signatures and propagation speed. *Journal of the Mechanics and Physics of Solids* 44, 981-1006.

Zhou, M., Ravichandran, G. and Rosakis, A.J. (1996b) Dynamically propagating shear bands in impact-loaded prenotched plates – II. Numerical simulations. *Journal of the Mechanics and Physics of Solids* 44, 1007-1032.

## List of Tables

Table 1. Chemical composition of C-300 maraging steel

## List of Figures

- Figure 1 Specimen geometry and impact arrangement. The projectile is 127mm long. All dimensions shown are in millimeters.
- Figure 2 Schematic illustration of the experimental setup. The CGS setup measures the out of plane displacement gradients on the rear side of the specimen. Simultaneous thermal imaging is accomplished using the IR camera on the facing side of the specimen.
- Figure 3 Effect of shearing direction on CGS fringes. (a) Shearing in  $x_1$  direction. (b) Shearing in  $x_2$  direction.
- Figure 4 Block diagram for IR camera operation.
- Figure 5 Ray diagram for double Schwarzschild optical focussing lens.
- Figure 6 A photograph of the IR camera.
- Figure 7 Calibration curves obtained by repeatedly heating the sample to 225°C.
- Figure 8 Calibration curves obtained by heating the sample to 525°C and 225°C.
- Figure 9 Ratio of the two calibration curves shown in Fig. 8.  $\Delta V_{HT}$  is the output from the 525°C test and  $\Delta V_{LT}$  is the output from the 225°C test.

- Figure 10 A sequence of CGS images obtained from the experiment with an impact speed of 15.5 m/s.
- Figure 11 Schematic illustration of (a) notch tip loading and (b) sharp crack tip loading.
- Figure 12 Schematic illustration of loading of a notch top with an extended fatigue crack.
- Figure 13 Comparison between synthetic and experimental fringes.
- Figure 14 Evolution of  $K_I$  prior to crack initiation in opening mode.
- Figure 15 Evolution of  $K_{II}$  prior to crack initiation in opening mode.
- Figure 16 Comparison of  $K_I$  evolution with analytical and numerical solutions of Lee and Freund (1990) for short times.
- Figure 17 Comparison of  $K_{II}$  evolution with analytical and numerical solutions of Lee and Freund (1990) for short times.
- Figure 18 An optical micrograph of an incipient shear band at the crack tip.
- Figure 19 A sequence of CGS images up to shear band initiation.
- Figure 20  $K_I$  at the time of shear band initiation as a function of impact speed.
- Figure 21  $K_{II}$  at the time of shear band initiation as a function of impact speed.
- Figure 22 Critical  $K_{II}$  for shear band initiation.
- Figure 23 A sequence of CGS images showing shear band propagation.

- Figure 24 Shear band advance as a function of time.
- Figure 25 Shear band velocity as a function of time.
- Figure 26 Mixed mode crack initiation criterion: a comparison with analytical models.
- Figure 27 **An** optical micrograph of an arrested shear band.
- Figure 28 **An** SEM image of the fracture surface that failed by shear banding.
- Figure 29 Optical micrographs of possible shear band bifurcation.
- Figure 30 A sequence of thermal images showing the transition of crack tip plastic zone in to a shear band.
- Figure 31 A comparison of the size and shape of the crack tip plastic zone with numerical solution of Needleman and Tvergaard (1995).
- Figure 32 A sequence of thermal images revealing the structure of the tip of a propagating shear band.
- Figure 33 A thermal image of a shear band showing non-uniform temperature distribution along the length of the band.
- Figure 34 Linear stability analysis of the deformation of a layer of material subjected to a shear stress.

Ni	Co	Mo	Ti	Si	Al
18.1	9.1	4.95	0.65	0.08	0.05

Table 1

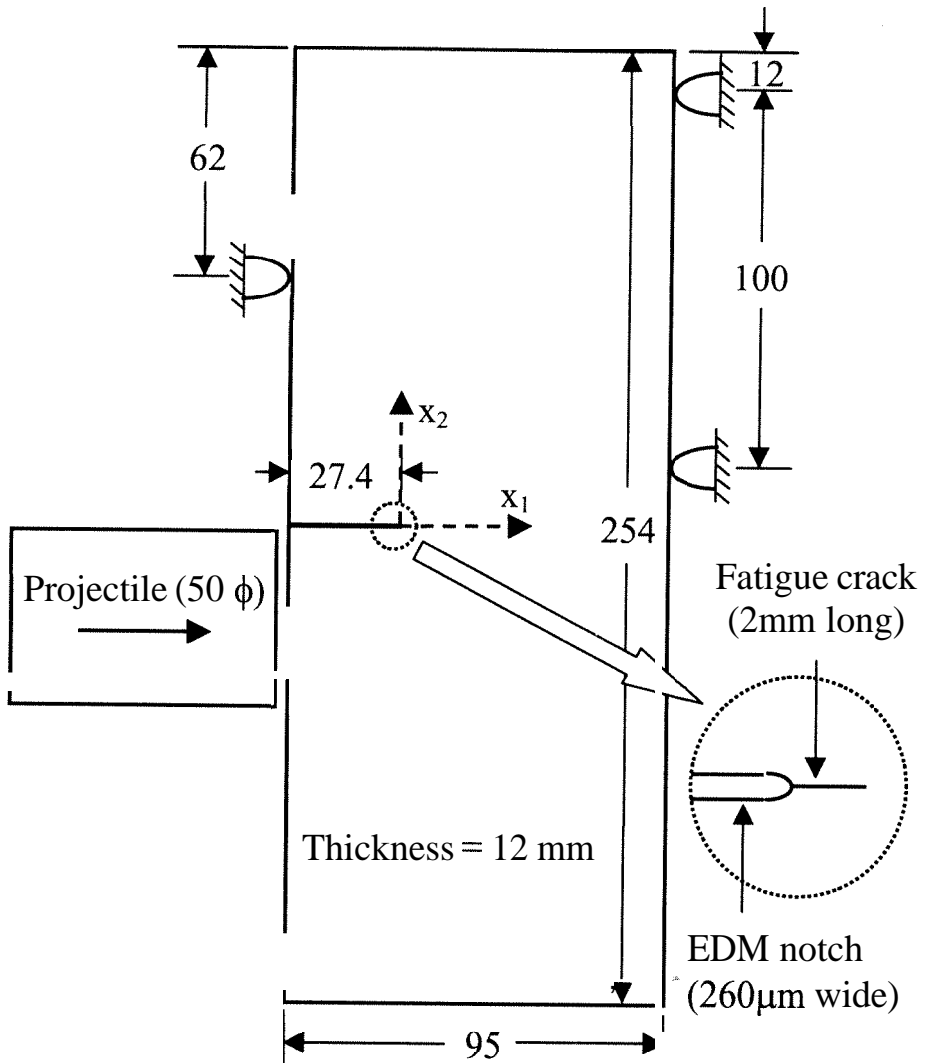


Figure 1

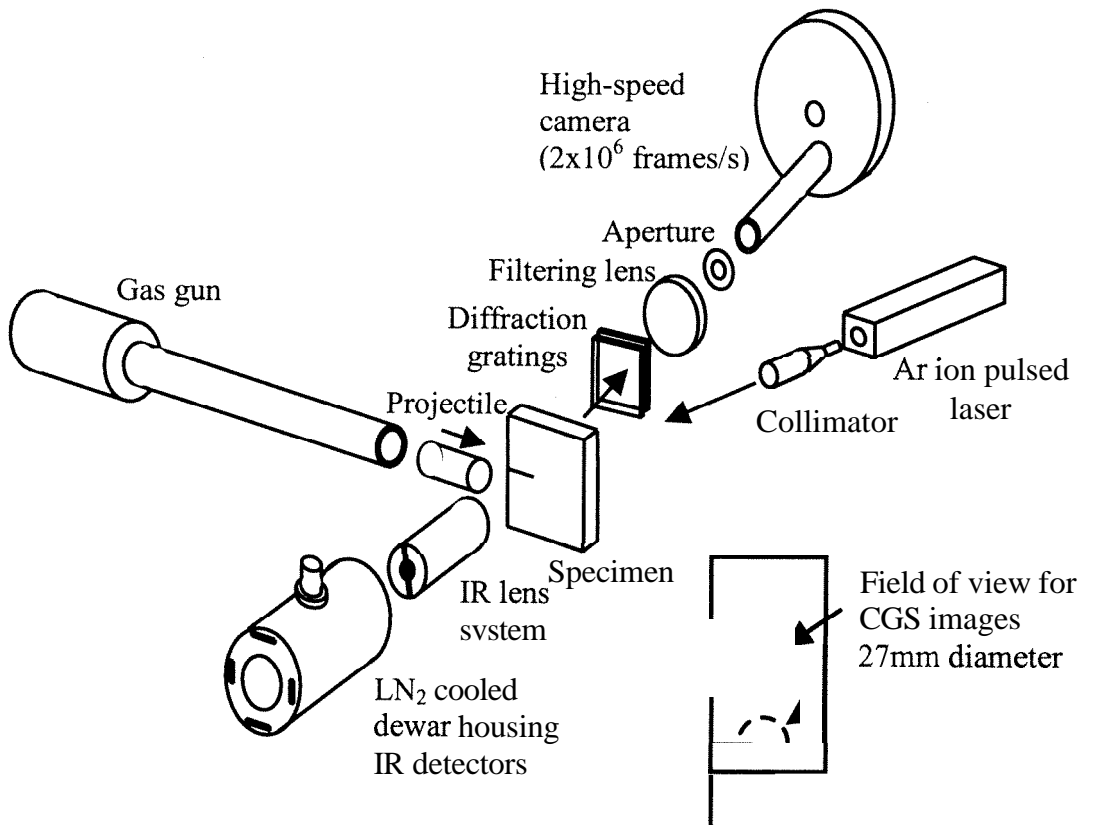


Figure 2

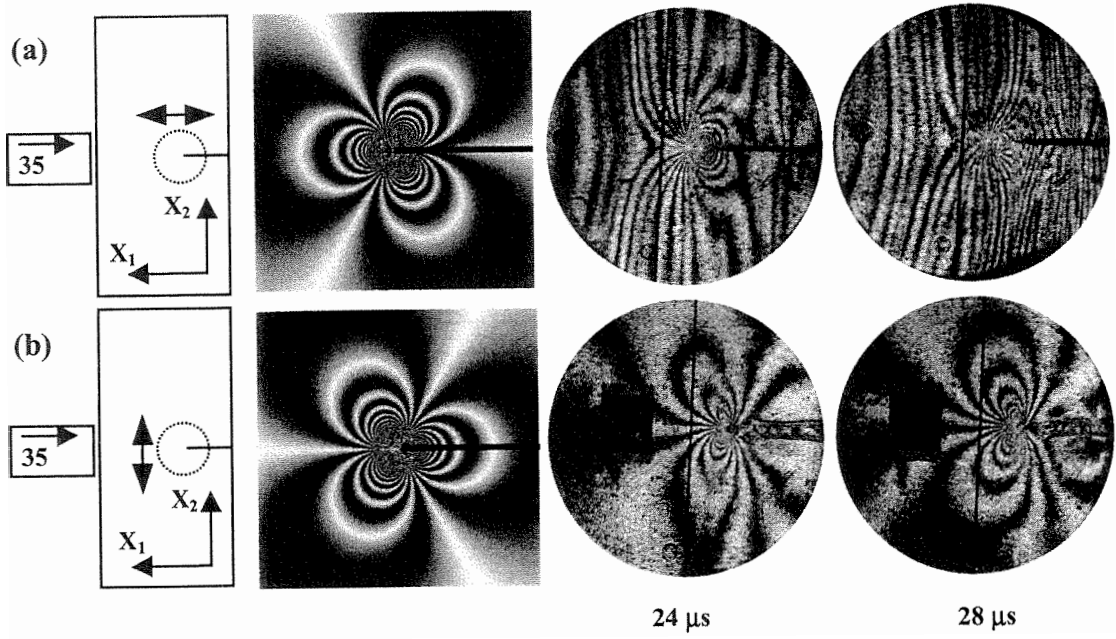


Figure 3

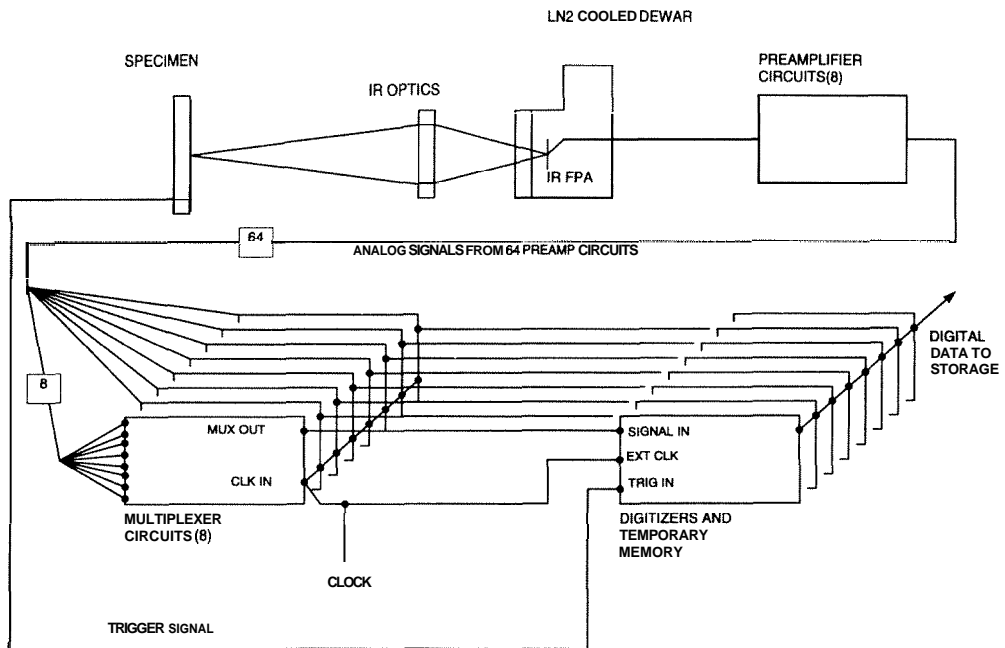


Figure 4

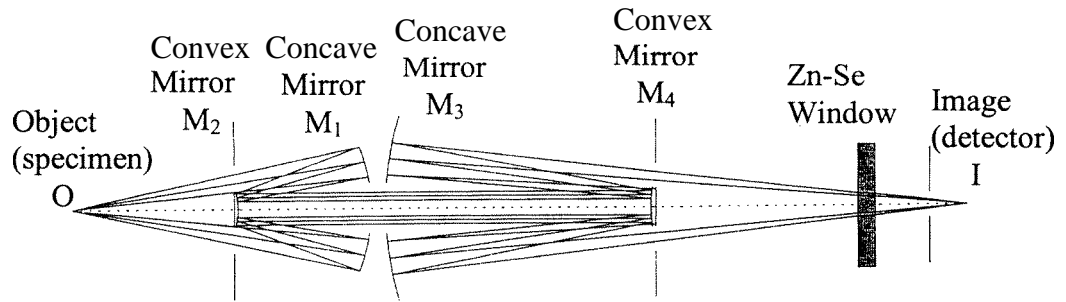


Figure 5

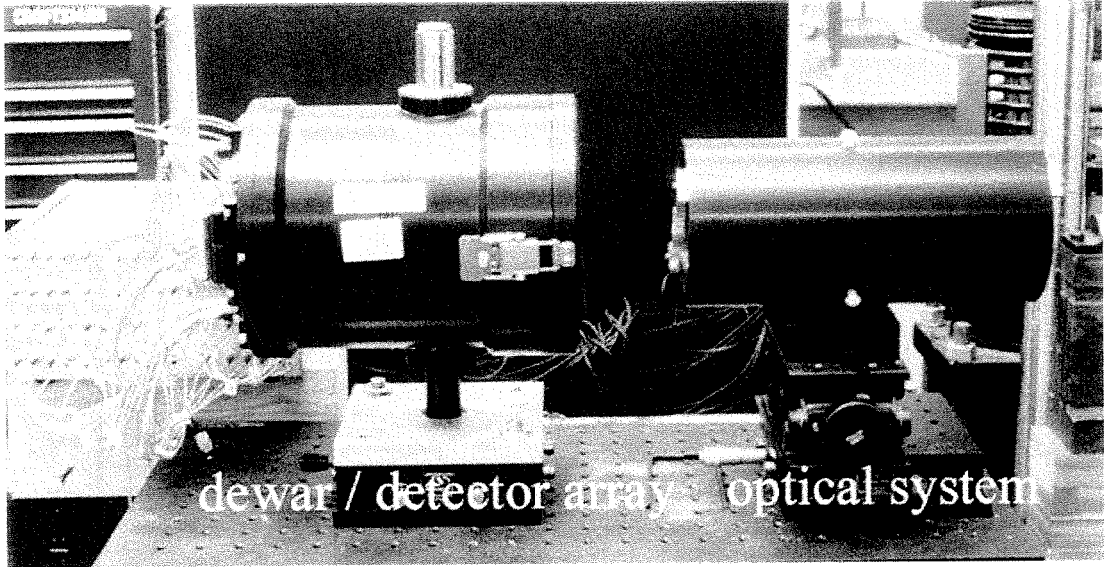


Figure 6

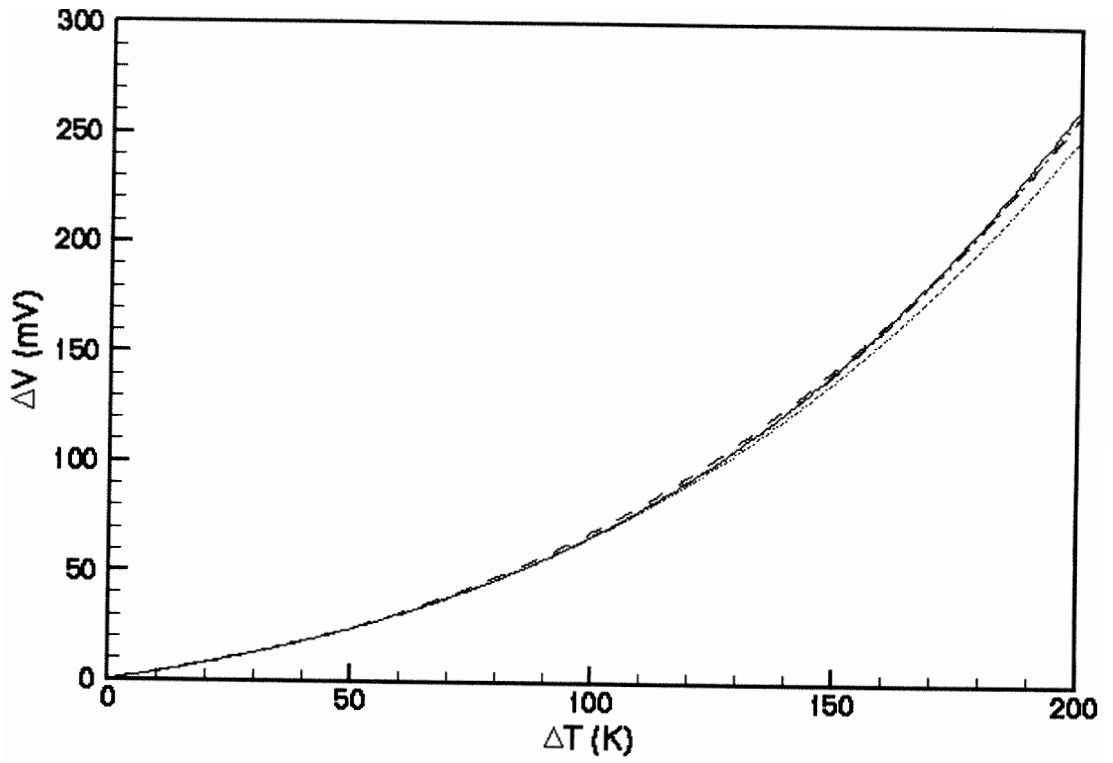


Figure 7

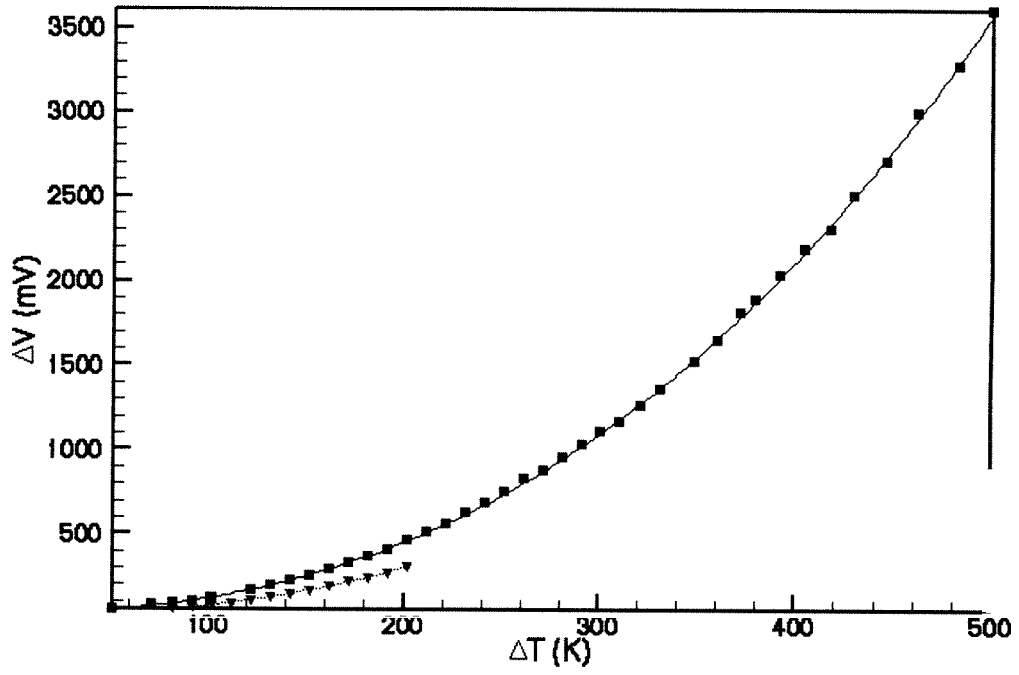


Figure 8

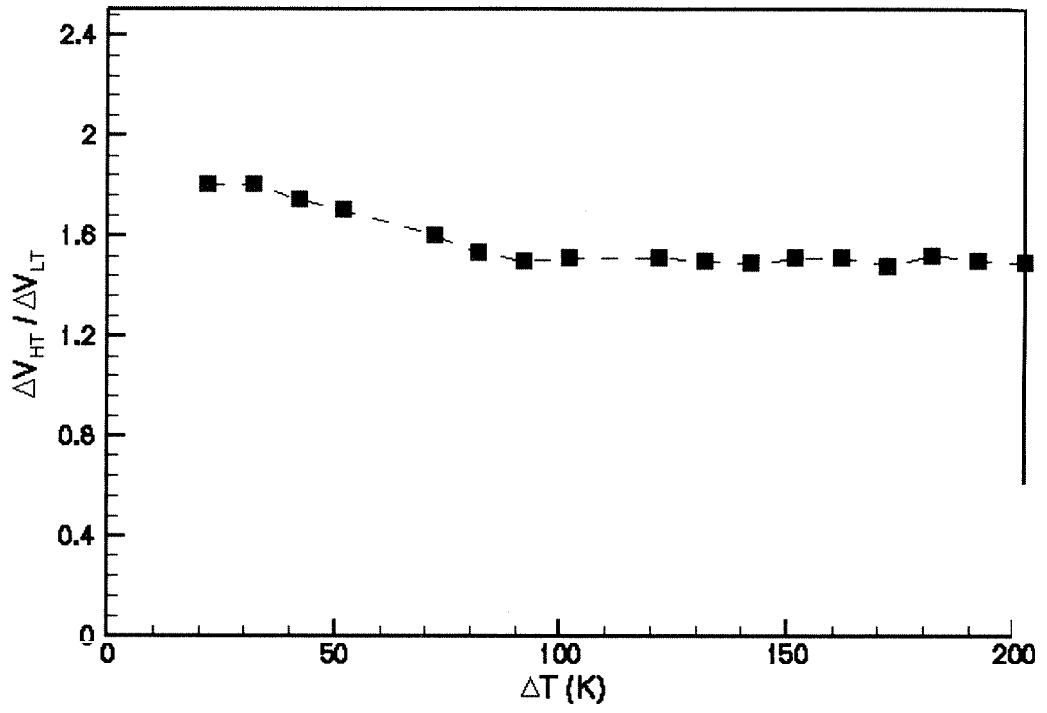


Figure 9

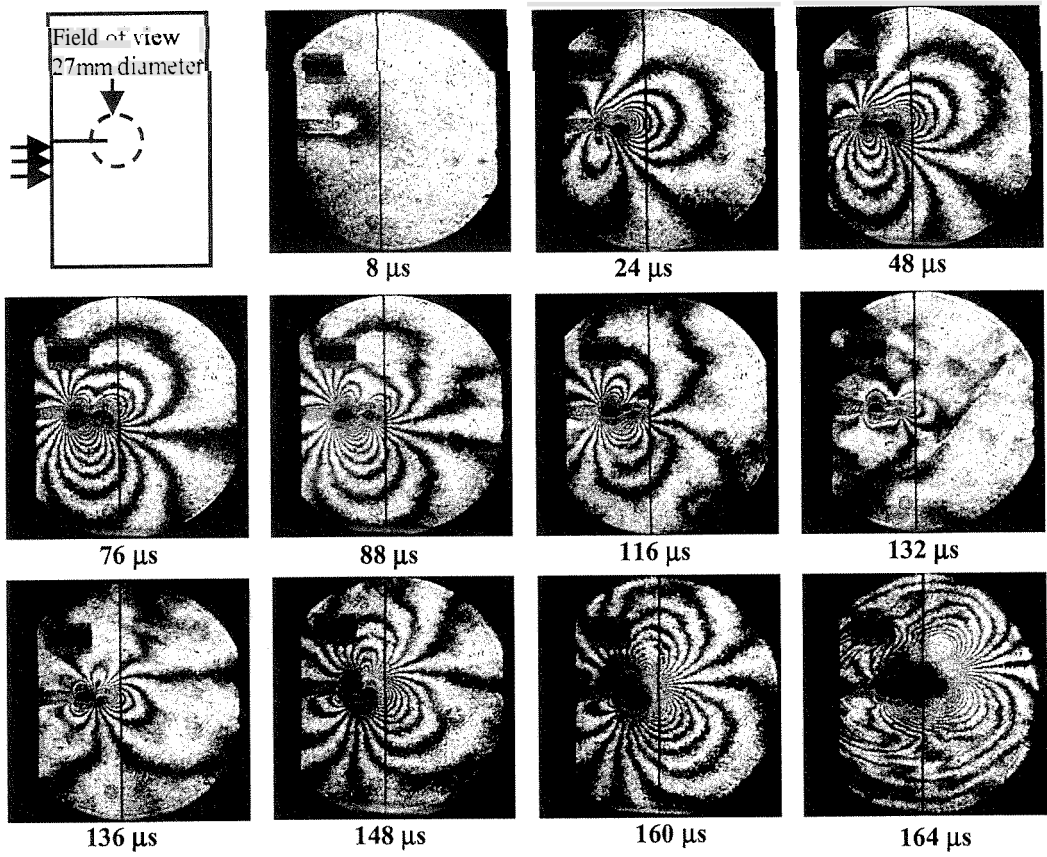


Figure 10

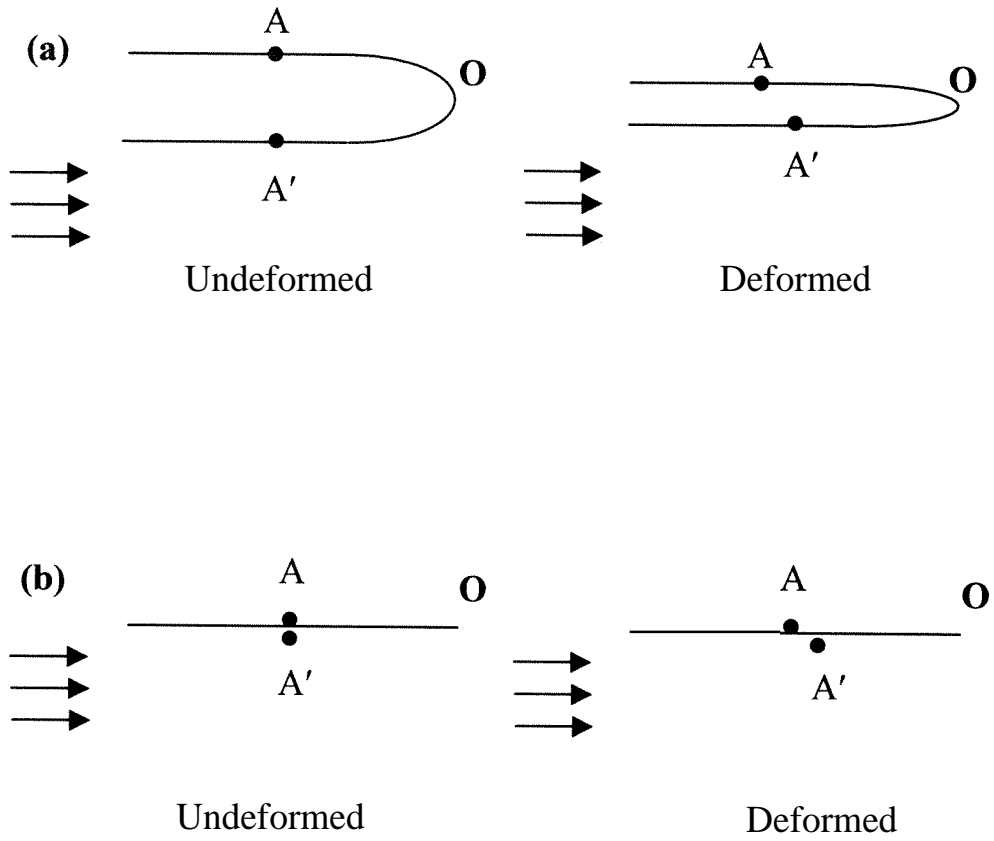


Figure 11

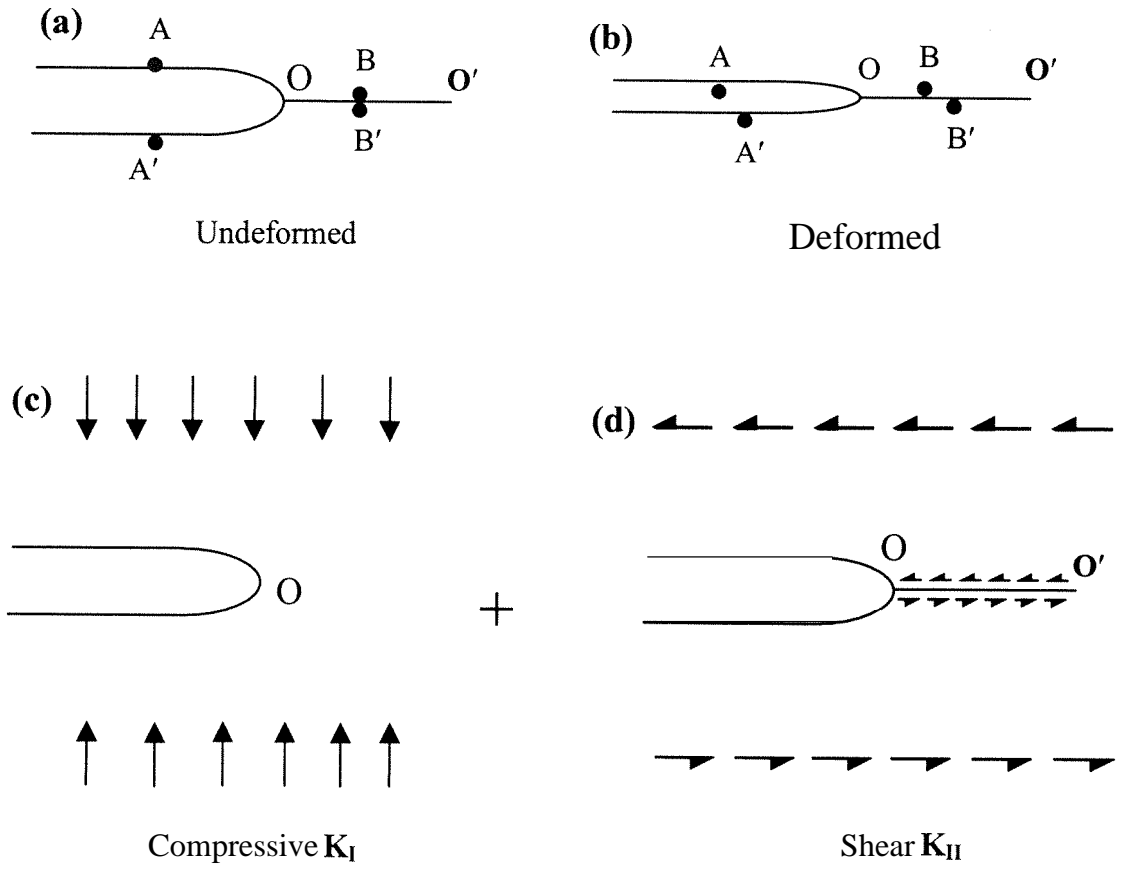


Figure 12

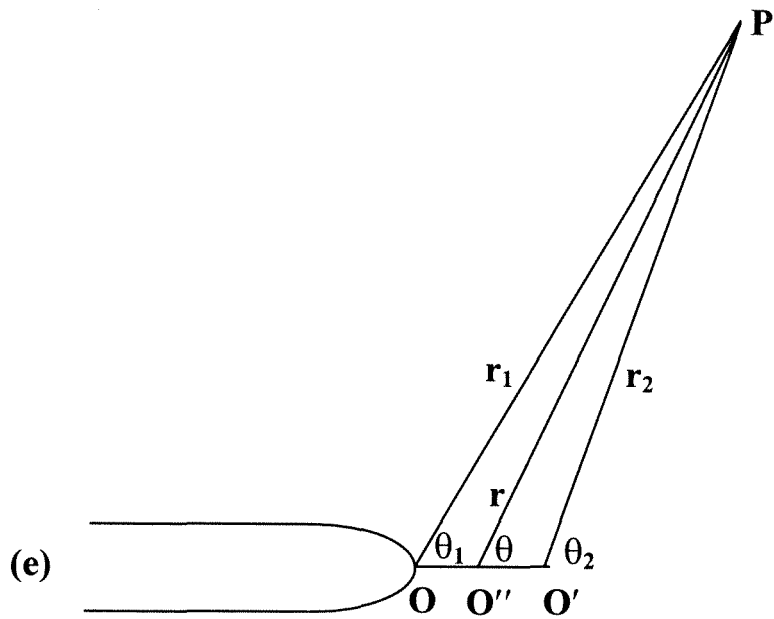


Figure 12 (continued)

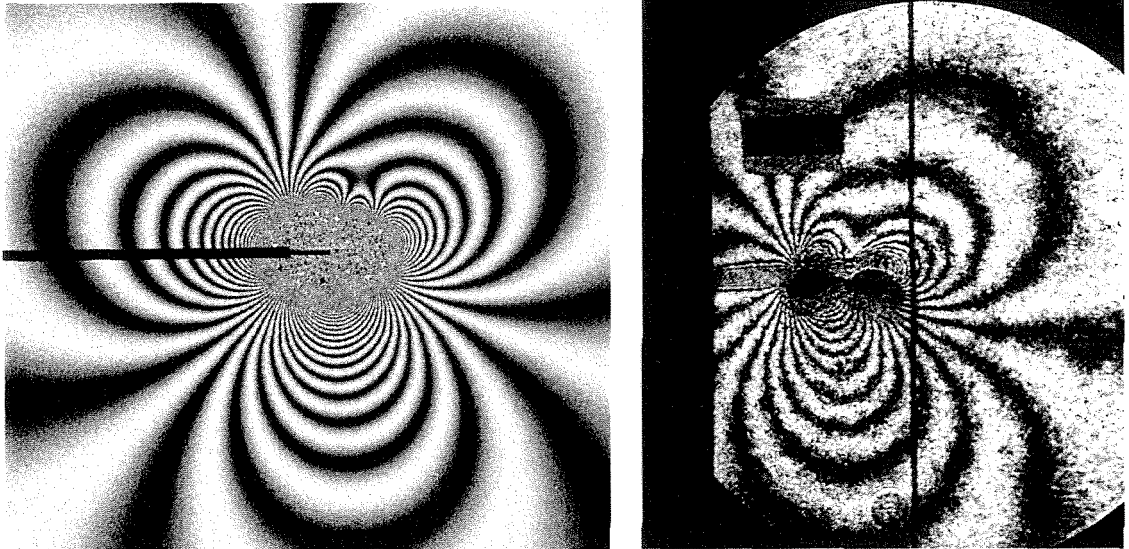


Figure 13

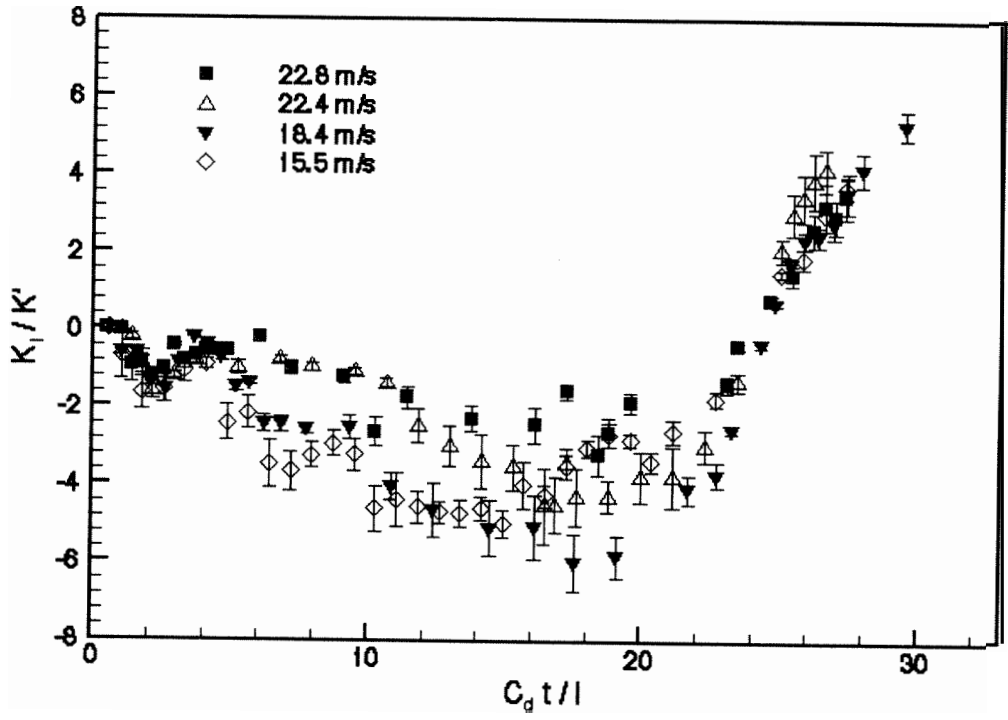


Figure 14

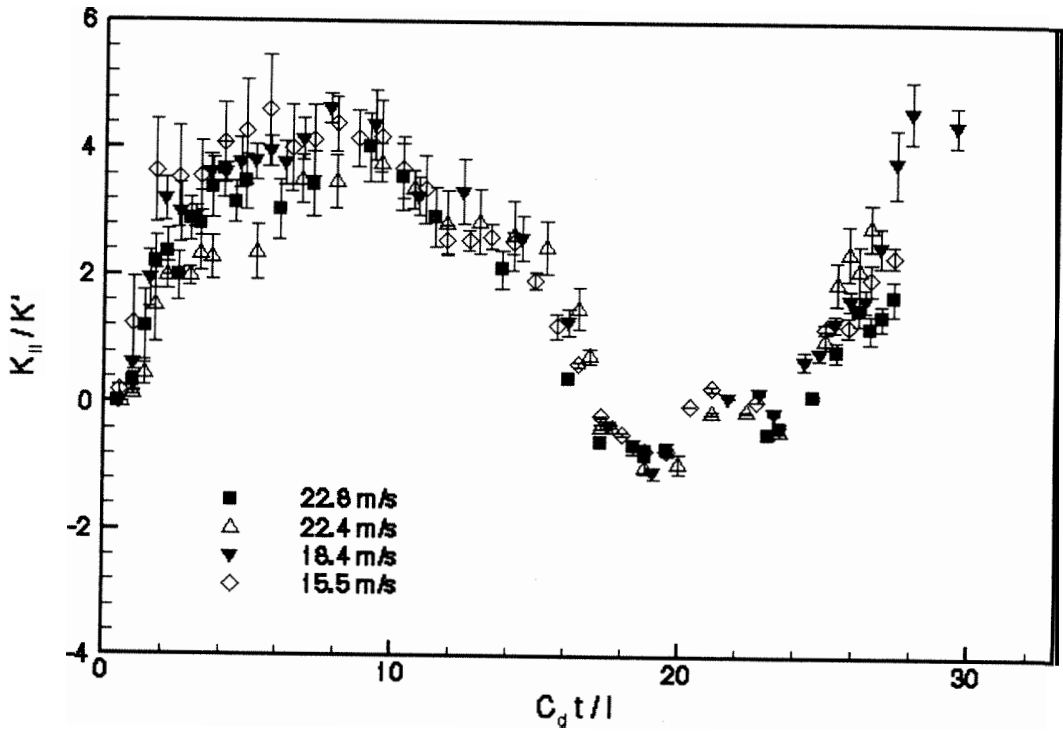


Figure 15

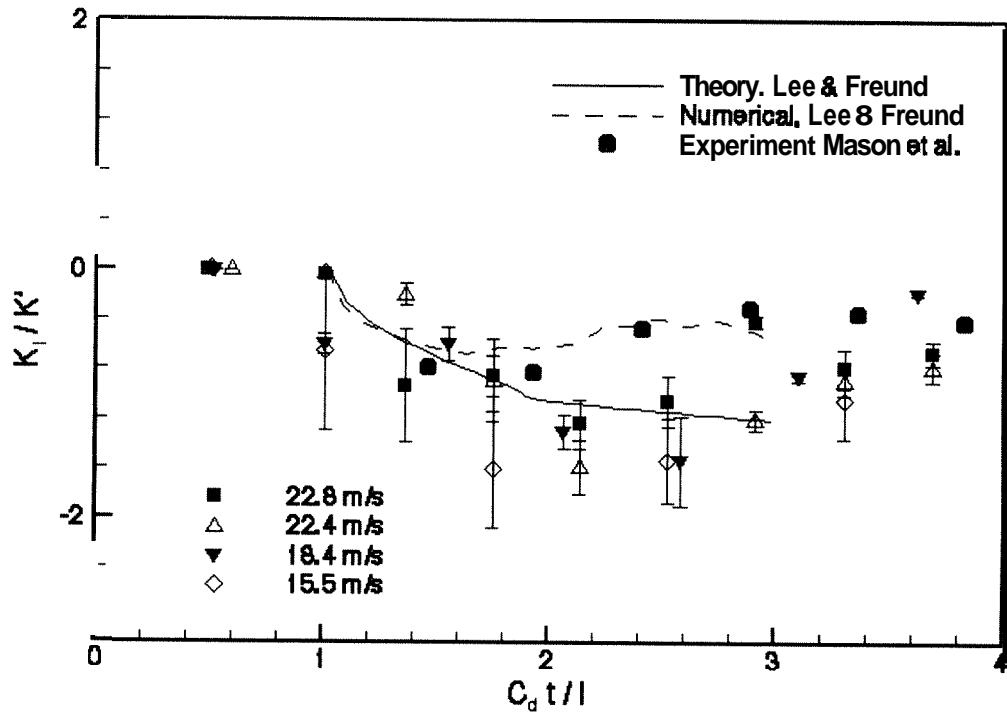


Figure 16

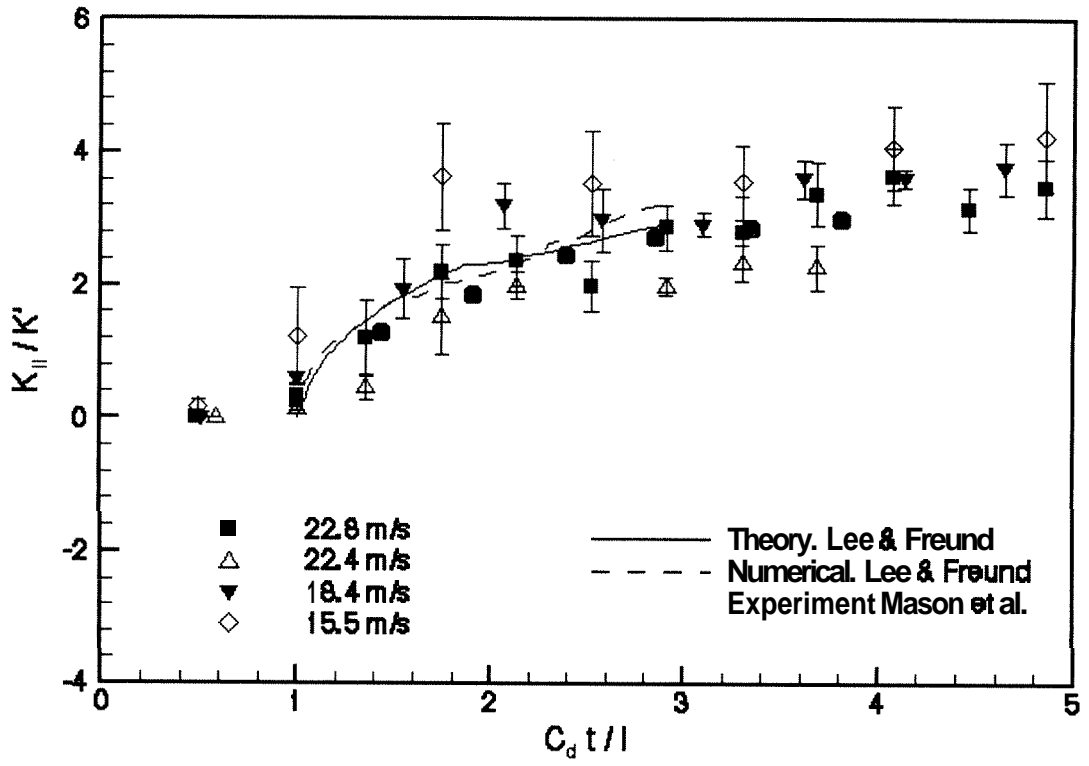


Figure 17

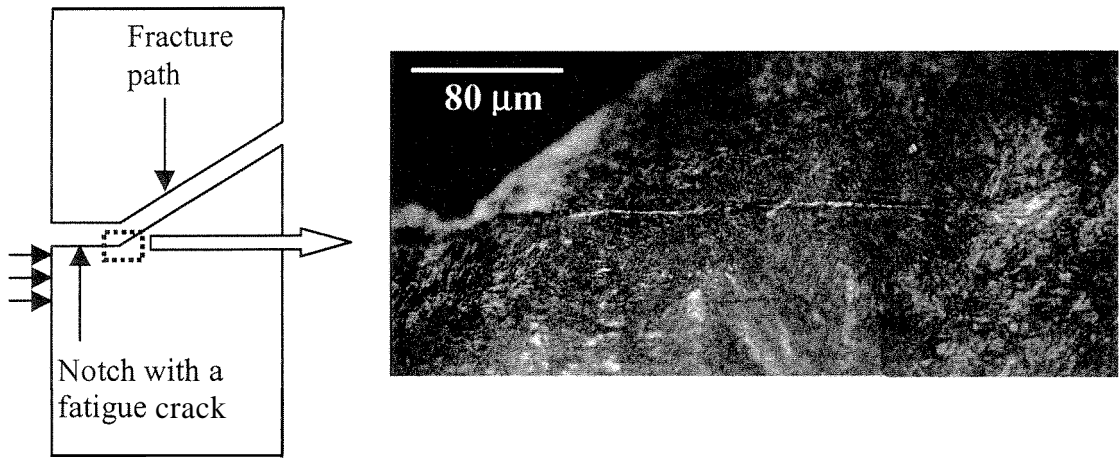


Figure 18



6  $\mu$ s



8  $\mu$ s



10  $\mu$ s



12  $\mu$ s

Figure 19

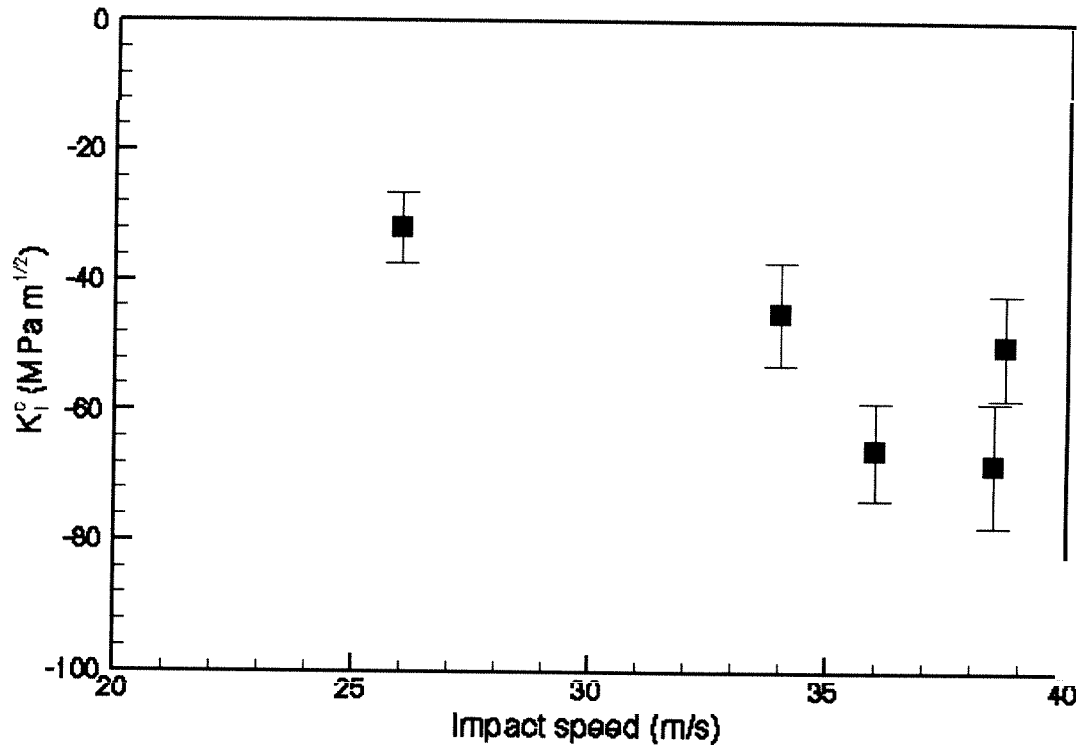


Figure 20

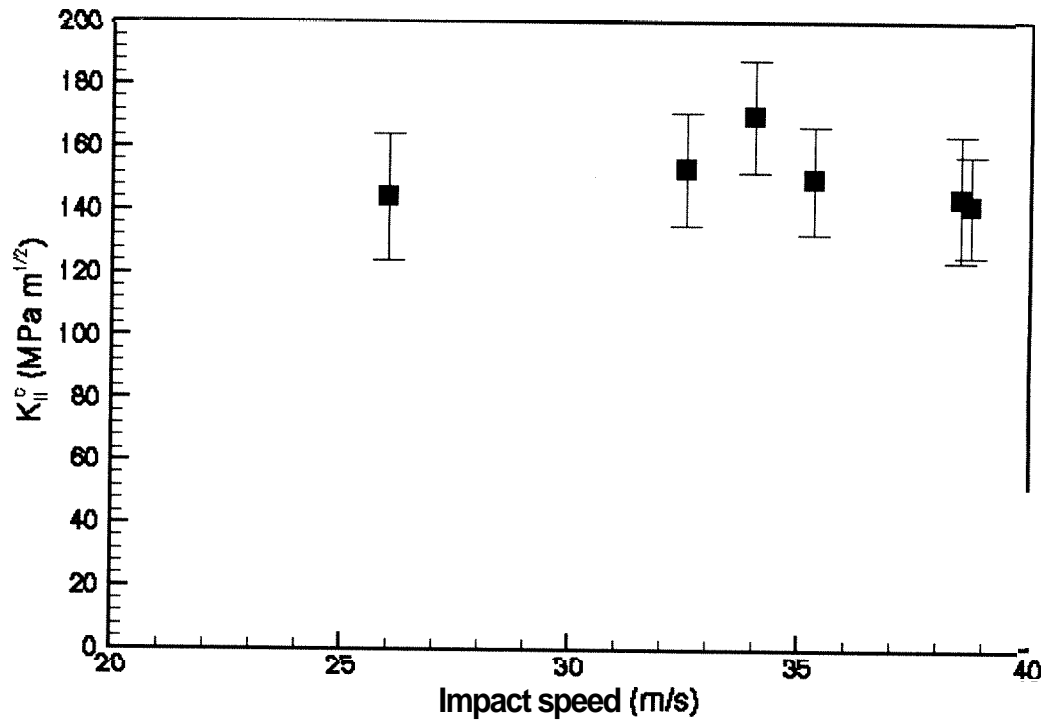


Figure 21

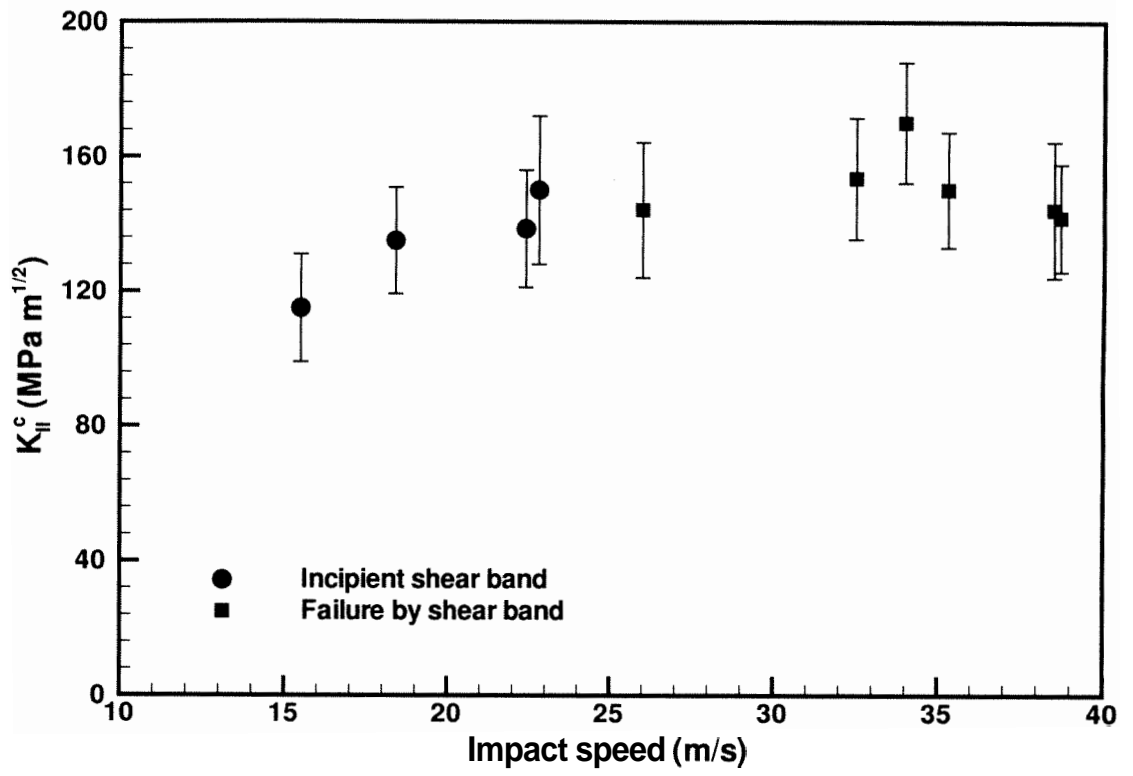


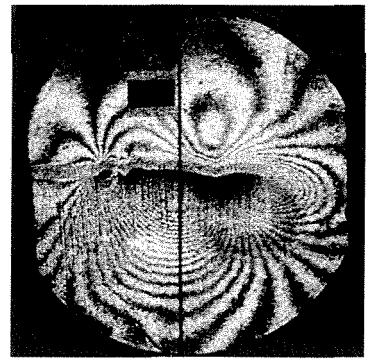
Figure 22



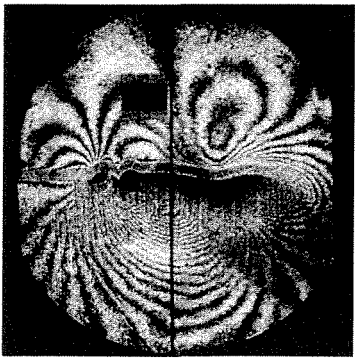
24  $\mu$ s



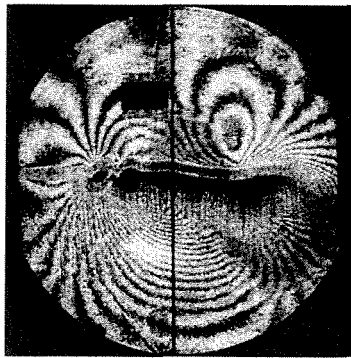
28  $\mu$ s



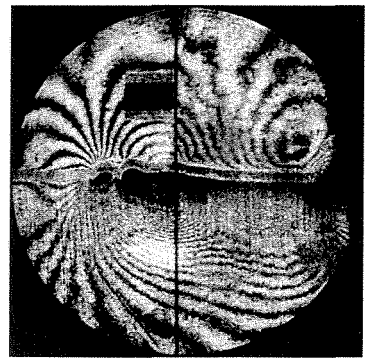
32  $\mu$ s



36  $\mu$ s



40  $\mu$ s



44  $\mu$ s

Figure 23

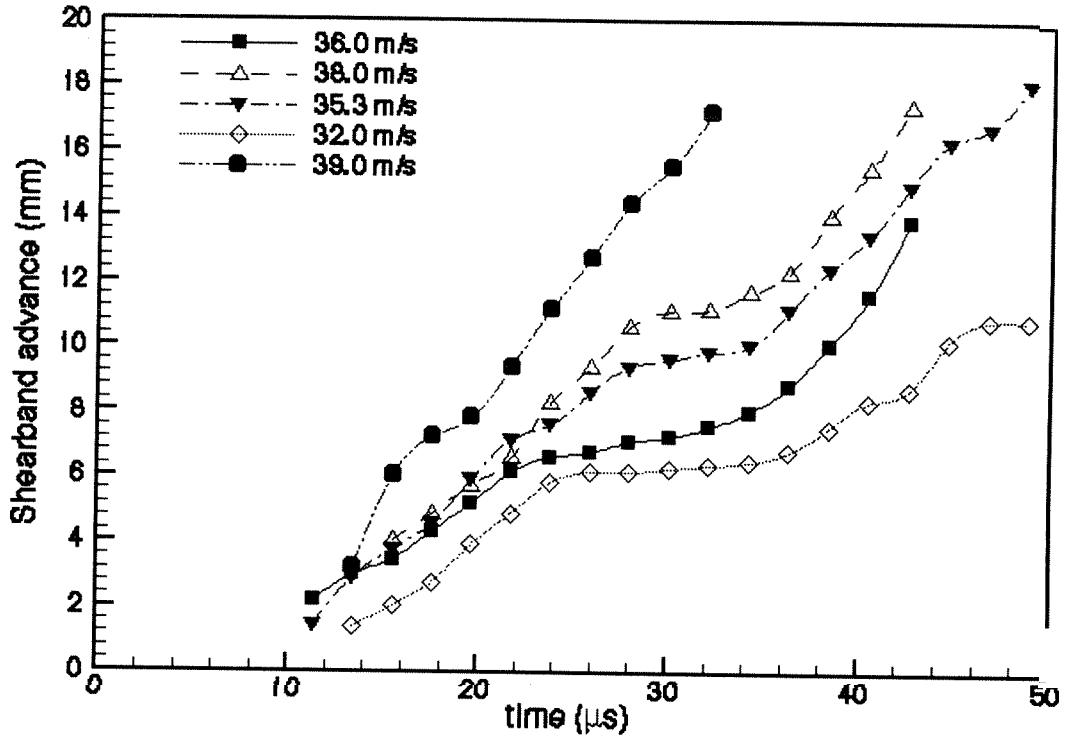


Figure 24

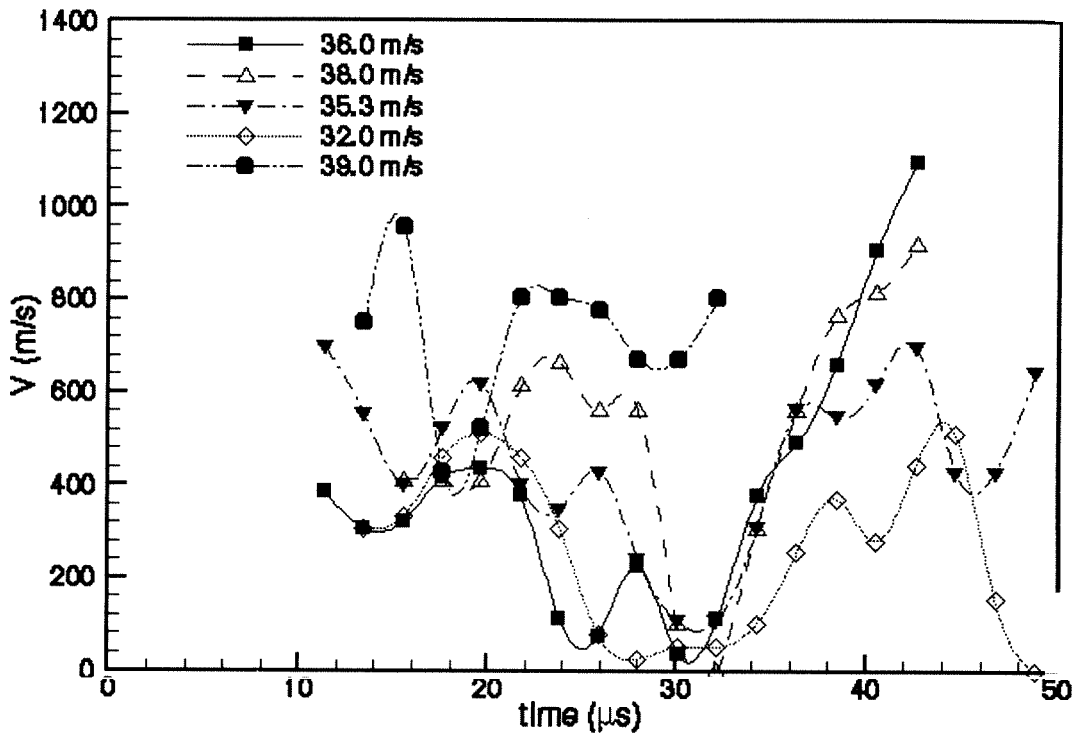


Figure 25

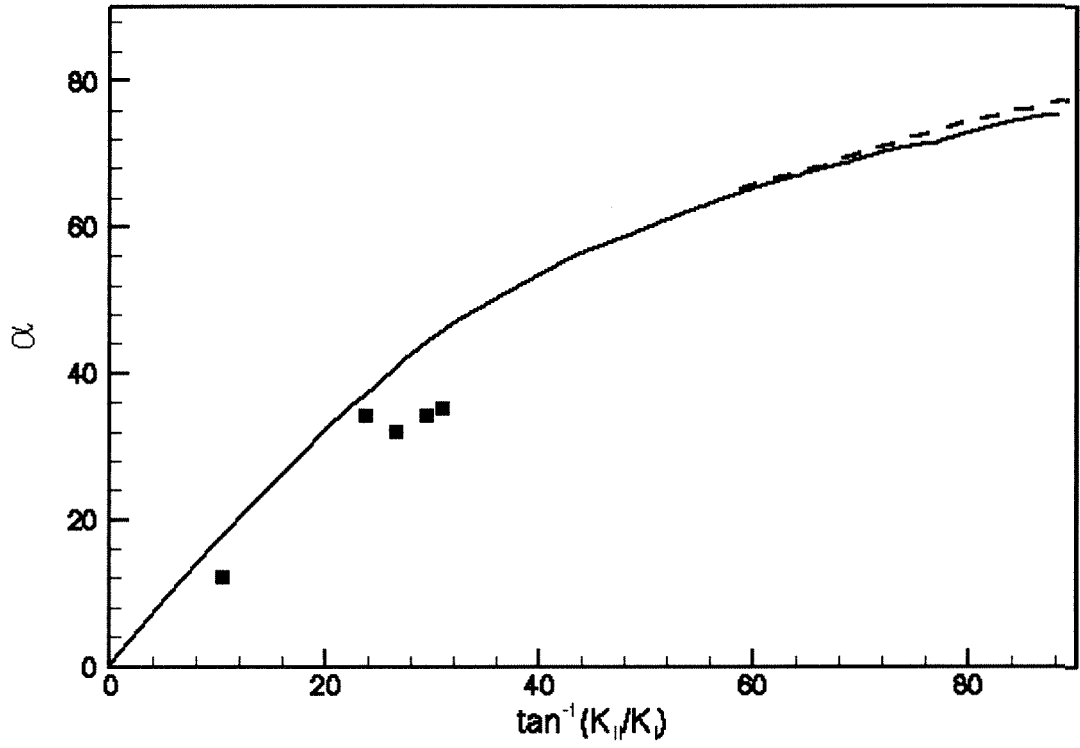


Figure 26

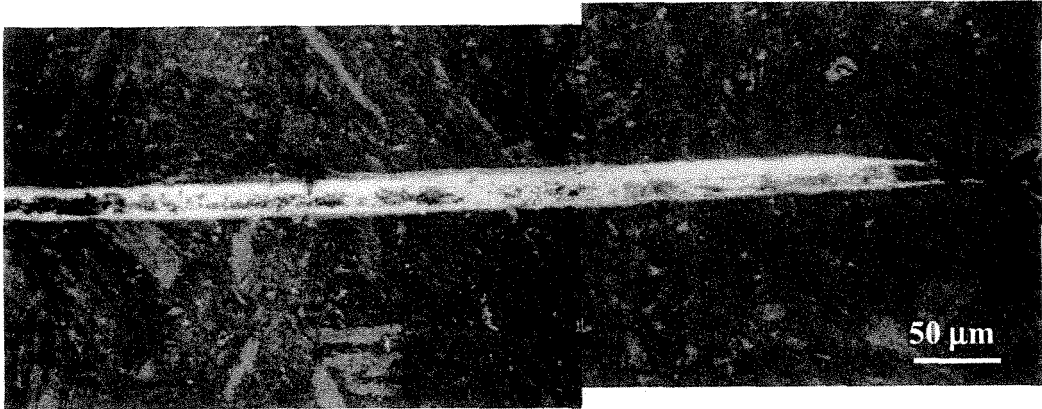
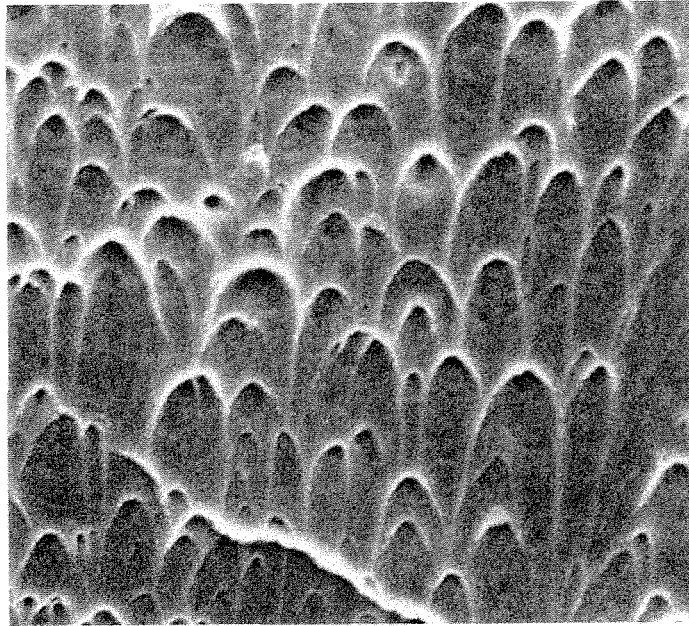


Figure 27



5  $\mu\text{m}$

Figure 28

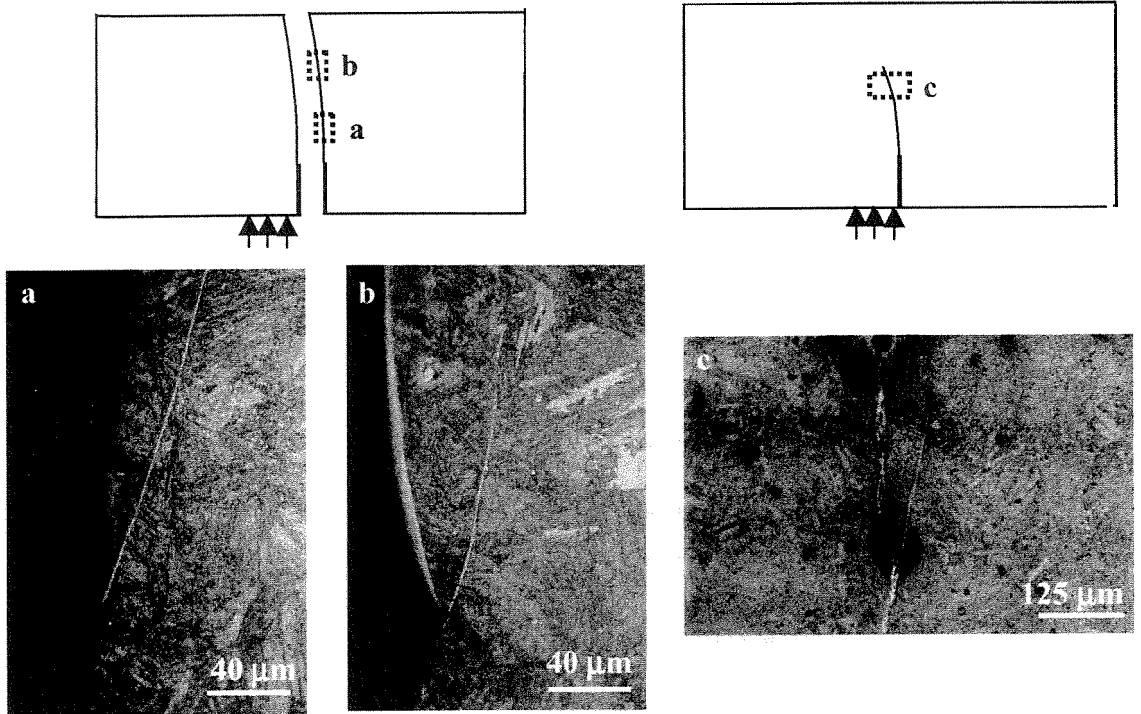


Figure 29

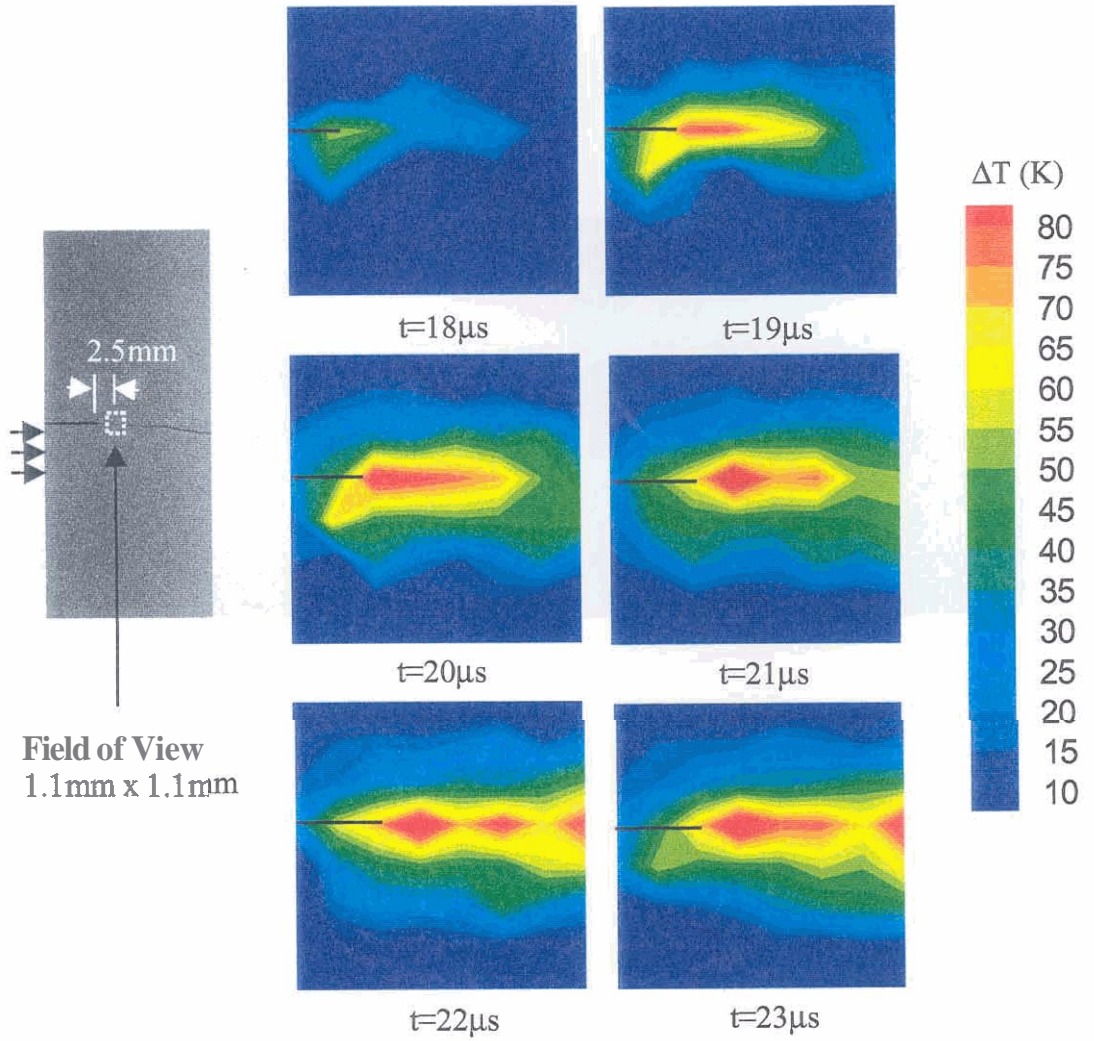


Figure 31

Figure 30

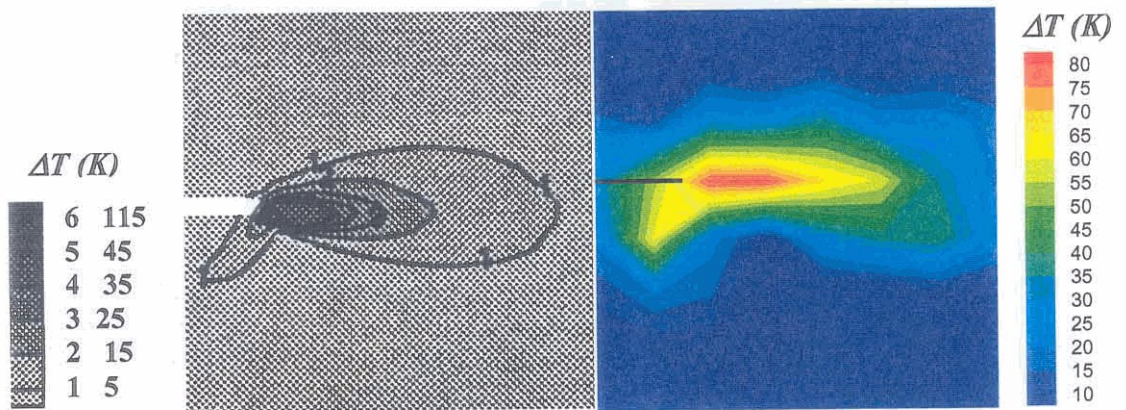


Figure 31

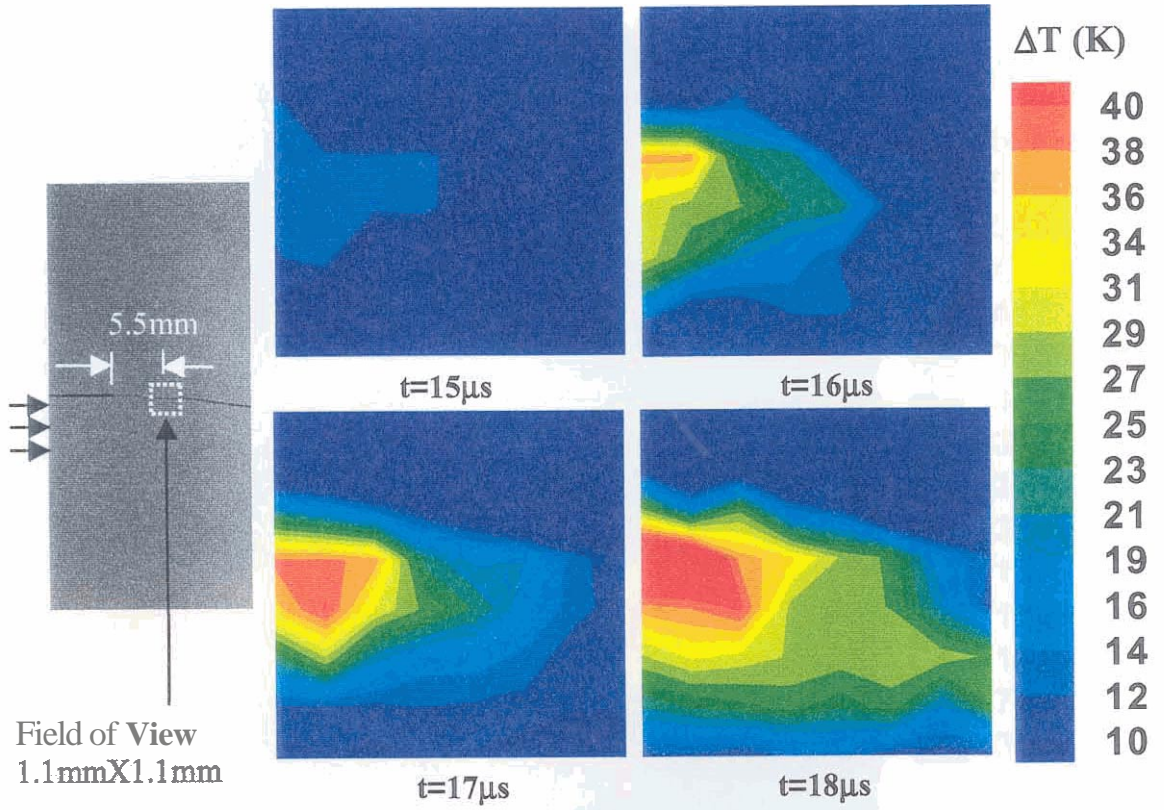


Figure 32

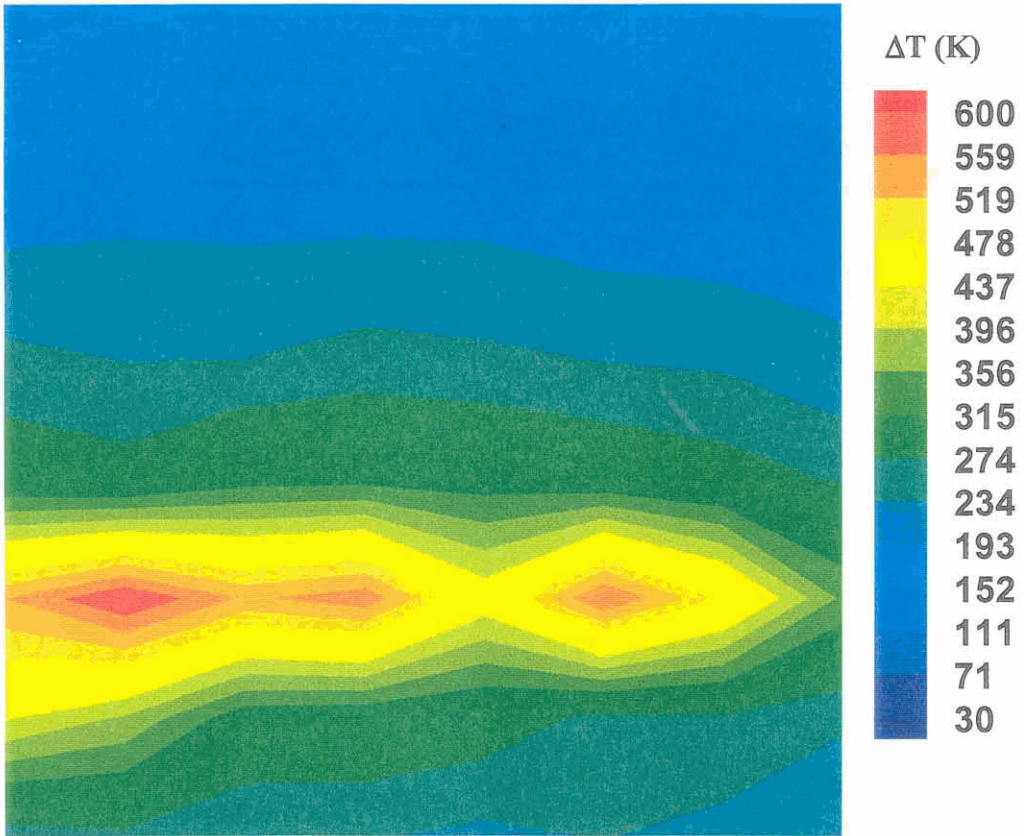


Figure 33

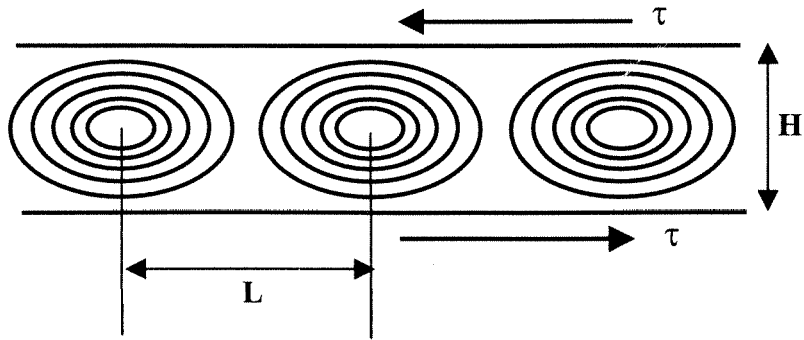


Figure 34